MEASURING MASS: NON-CIRCULAR MOTIONS OF GAS IN DISK GALAXIES AND RADIAL VELOCITIES OF STARS IN A GLOBULAR CLUSTER

BY RICARDO ZÁNMAR SÁNCHEZ

A dissertation submitted to the

Graduate School—New Brunswick

Rutgers, The State University of New Jersey

in partial fulfillment of the requirements

for the degree of

Doctor of Philosophy

Graduate Program in Physics and Astronomy

Written under the direction of

J.A. Sellwood

and approved by

_____

_____

_____

_____

_____

New Brunswick, New Jersey

October, 2009

ABSTRACT OF THE DISSERTATION

Measuring Mass: Non-circular Motions of Gas in Disk Galaxies and Radial Velocities of Stars in a Globular Cluster

by Ricardo Zánmar Sánchez

Dissertation Director: J.A. Sellwood

This thesis is concerned with the motions of gas in disk galaxies and with the motions of stars in a globular cluster to learn about their mass content.

First we study non-circular streaming motions of HI gas in five representative disk galaxies with a bisymmetric model. We show that this physically motivated method can represent a wide range of bar-like distortions and that its model parameters can be related to useful physical parameters of galaxies like the amplitude of the forced non-circular speed, the bar angle, and halo ellipticity.

We also model the non-circular gas flow in the strongly barred galaxy NGC 1365. The gravitational potential is based on new observations that include photometric imaging, Fabry-Perot emission line imaging spectroscopy and a detailed re-analysis of archival HI data from the VLA. We use our 2-dimensional velocity map to constrain the strength and positions of the shocks in hydrodynamical simulations and find that better agreement is found with a massive, but not fully maximal disk ($M/L \simeq 2.0 \pm 1.0$) and a fast bar (corotation at $1.2R_{bar}$). The analysis was complicated by the discovery of an asymmetric distribution of dust and kinematics in the bar region despite the remarkably bisymmetric

distribution of the I-band light.

We have measured 543 radial velocities of stars in the direction of the Galactic globular cluster M80 with Fabry-Perot absorption-line imaging spectroscopy. The data is used to derive the total mean velocity of 7.39 ± 0.54 km s^{-1}, the total velocity dispersion of 10.1 ± 0.4 km s^{-1}, a declining dispersion profile, and the rotation of the cluster. M80 is rotating with an amplitude of 2.42 ± 0.81 km s^{-1} along an axis with a position angle of $246.1^{\circ} \pm 17.1$ (measured from North through East), which is perpendicular to the major axis of the cluster flattening. We have fitted single- and multi-mass Michie-King models to our velocity data and to surface-brightness profiles taken from the literature. Only when we increase the expected present-day number of white dwarfs are we able to match the expected M/L_V of the stellar population with the dynamically-derived value of 3.0 ± 0.3. We tentatively interpret this as evidence of tidal stripping given that M80 is on an orbit that keeps it in the inner regions of the Galaxy and therefore has probably experienced significant tidal mass loss.

Acknowledgements

This work would not have been writable (nor readable!) without the ideas, support and corrections of Jerry and Tad. I'm very grateful to them both. Jerry was instrumental in my research and in the completion of my dissertation. He was also responsible for sending me on quests for knowledge to Socorro (the VLA), Las Vegas, and Switzerland. I also had the opportunity to learn quite a few programming tricks from the master himself and have also adopted his FORTRAN formatting style that I find very useful(though sometimes I find $ myself overdoing it). I'm very lucky to have met Tad because he is the most patient-knowledgeable person I know. Chapter four was entirely written under his supervision. He is also living proof that there are actually astronomers who know their way around the sky and are always aware of the time when the sun sets throughout the year.

I would like to express my gratitude to other influential faculty members: Ted Williams, our Fabry-Perot guru. I always appreciated his sense of humor and was impressed by how quick he runs calculations in his head. Ted always took the time to cheer me up when times were tough, despite his hectic schedule. I also thank Eric Gawiser for giving me insight into the minds of professors during the job-hunting season, Andrew Baker for being overwhelmingly helpful (I once asked him for a bibliographic reference; he suggested ten and a meeting with one of the authors!), and Jack Hughes for the support to attend a conference in South Africa. Jack also carefully read the whole dissertation and kindly provided detailed suggestions.

I'm indebted to Ben Weiner who, despite the distance, was a constant ghostly presence in my early years. His apparitions took the form of emails, personal notes, bash scripts, and FORTRAN code that he kindly shared with me and from which I learned a lot. I'm also

grateful to Kristine Spekkens for her help with all radio-related questions and for cheering me up during the rough job-season.

I wish to thank my personal assistant and public image adviser, Naseem Rangwala, whose help in all things related to functioning in real life was indispensable throughout the years. Examples of her services are: reminders to pay taxes on time, to register for classes every semester so I could maintain my legal status as an international student and avoid deportation, reminders to renew my driver license, etcetera. Naseem is also responsible for my addiction to Indian cuisine.

Thanks to my officemates: Ross Fadely, who was kind enough to put up with my mysterious and secretive ways, my South African friend Menzi Mchunu[1] for the pool games and those hard early years in Lukyanov's class marked by his constant "in principle you should know this", Xifan Wu, my ping pong nemesis, Eric Barnes who helped me get started with IRAF, Bonita de Swardt, for showing me the nice hidden corners of Cape Town, Neelima Sehgal, the fearless defender of women's rights and the only pilot I've ever personally met, Monica Haşegan with whom I had many interesting conversations and who entrusted me the delicate task of printing and handing in her dissertation. Other nice people I had the pleasure of meeting are Juntai Shen, Gabe Alba (commander-in-chief of the geek soccer club where I felt quite at home), Chelsea Sharon, Felipe Menanteau (thank you for the chocolate), Amruta Deshpande, Saquib Ahmed, Chrystal Delilah Battle, and the entire Italian department.

Last but not least, to Monica who I met the first day I set foot on College Ave. (my second day on American soil) and has shared with me ever since, the graduate-student experience and more.

[1] I could never really pronounce his last name. Mch is pronounced with a clicking sound that requires a careful interplay between the tongue and the roof of the mouth.

Dedication

A mis padres Nelva y Ricardo.

Table of Contents

List of Tables

List of Figures

Chapter 1

Introduction

Spiral galaxies are intriguing yet beautiful objects formed of stars and gas that rotate about a common center. Confined primarily to a single plane, these systems often have spiral arms, a spherical bulge and a bar in the center. In the nineteenth century, photographic plates allowed astronomers to clearly resolve the spiral arms that suggest their rotating nature. Years later, the first spectroscopic confirmation of rotation was made by Slipher (1914).

A number of kinematic tracers have been used to derive the rotation of disk galaxies: at optical wavelengths; the Hα, [NII] and [SII] transitions in the interstellar gas; in the radio, the spin-flip transition of neutral hydrogen gas (HI) and rotational transitions of carbon monoxide (CO). It was using HI that Bosma (1978) firmly established the rather surprising result that most rotation curves –the circular orbital speed as a function of radius– are flat to the last measured point, far beyond the observed distribution of stars. If Newton's laws hold true on those scales, this suggested that galaxies are embedded in mysterious non-luminous matter. Nowadays, the idea of mildly aspherical dark matter halos surrounding galaxies fits nicely with the current lambda[1] Cold Dark Matter (ΛCDM) paradigm in which the universe today is believed to comprise 20% dark matter, 4% baryonic matter, and 76% dark energy (Tegmark et al. 2006). According to this model, dark matter halos grow out of small density fluctuations by hierarchical clustering and merging. At the centers of some halos, gas sinks and settles into rotational balance as it loses energy through dissipative processes such as radiation and will eventually form stars and galaxies (Springel et al.

[1]Lambda (Λ) is the cosmological constant that models the observed accelerated expansion of the universe.

2006).

Since dark matter can not be directly observed, one has to rely on the gravitational effects it has on photons or on baryonic matter. For example, the theory of general relativity predicts that light rays are deflected by matter (*i.e.*, gravitational lensing) and therefore, distorted images of background galaxies have been used to probe the dark matter halos of galaxies (*e.g.* Fischer et al. 2000) and cluster of galaxies (*e.g.* Clowe et al. 2000). Also, non circular motions in the stars and gas are expected to be induced by the predicted aspherical dark matter halos. However, other non-axisymmetric features such as spiral arms and bars can also induce departures from circular motion. Characterizing such motions in 2-dimensional velocity maps is therefore desirable for an in-depth understanding of halo shapes and mass distribution. In Chapter 2 we made use of a technique first proposed by Spekkens & Sellwood (2007) to model streaming motions that allowed us to constrain the halo ellipticity of two galaxies: NGC 2403 and NGC 3198. The physically-motivated bisymmetric model that we employ can also model the strong departures from circular motions that occur in bars and we demonstrate this for the galaxy NGC 2903.

When the first researchers tried to model the mass in disk galaxies with the simplest mass-follows-light assumption (parametrized by a constant mass-to-light ratio) they found that acceptable fits were possible to optical rotation curves without the need of dark matter (Kent 1986). On the other hand, when extended rotation curves from HI observations were considered, dark matter was necessary in the models, but its exact amounts were impossible to determine from the rotation curve alone (van Albada et al. 1985; Lake & Feinswog 1989). As Bahcall & Casertano (1985) wrote: "The most striking feature of rotation curves is that there are no striking features". This inability to disentangle the relative contributions of baryonic and dark matter to the rotation curve has been dubbed the disk-halo degeneracy problem.

An upper limit for the disk mass is provided by the maximum-disk hypothesis. Under this assumption, the maximum possible M/L is attributed to the disk (and spherical bulge,

when present) consistent with the inner parts of the rotation curve . This idea is supported by the good fits to optical rotation curves (Palunas 1996) but is in disagreement with results from ΛCDM numerical simulations that predict galaxies dominated by dark matter.

Several dynamical arguments have been proposed to break the disk-halo degeneracy. For example, Bottema (1997) and Verheijen et al. (2004) argue that the vertical velocity dispersion of stars in nearly face-on galaxies contains information about the disk mass; Athanassoula et al. (1987) restrict the allowed range of the disk contribution to the rotation curve of galaxies by invoking spiral structure theory in which the number and strength of spiral arms depends on the disk-to-halo mass ratio. Stellar population synthesis models (Bell & de Jong 2001) have also attempted to model the mass disk (parametrized by a mass-to-light ratio) from broad-band colors. But these constraints are insufficiently tight to favor either a maximum or half-maximum disk. Weiner et al. (2001) proposed a method to address this problem that uses galactic bars.

Bars are a common dynamical component of disk galaxies (Sheth et al. 2008). Their elongated shapes are thought to be the superposition of stars in very elliptical stable orbits which rotate together with a common bar pattern speed (Sellwood & Wilkinson 1993). Bars can have a significant impact on the morphology of the galaxy they inhabit. For example, bars can give rise to inner and outer rings, funnel gas to the center of the galaxy, drive spiral arm structure, and shock gas on the leading side of bars –sometimes seen as dust lanes (Kormendy & Kennicutt 2004). It is the distortions imprinted on gas flow that allowed Weiner et al. (2001) to constrain the mass of the disk in barred galaxies.

Although stars in bars can follow elongated orbits which sometimes cross, gas clouds collide and shock. These signatures depend on the mass of the bar and thus can be used to estimate the matter in the stars and halo. Out of the two main competing mass components, the assumed spherical halo and the non-axisymmetric bar potential, only the latter can create the observed signature in velocity maps (see Fig. 1.1). Therefore one can create hydrodynamical simulations in which the mass and pattern speed of the bar are varied

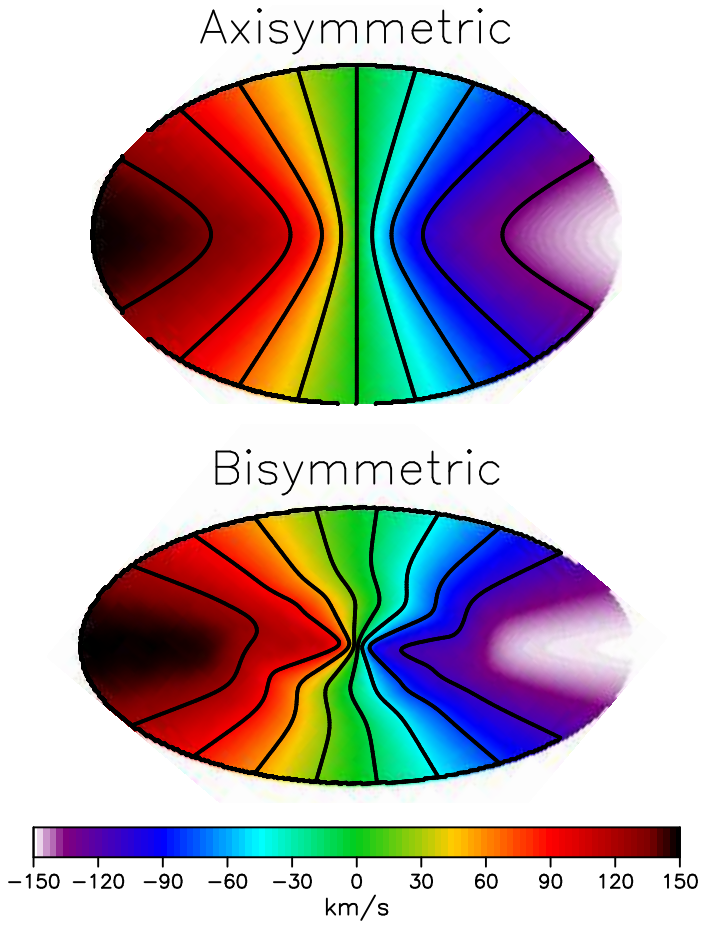

Figure 1.1 Velocity maps for two model galaxies projected in the sky. The solid lines are isovelocity contours. Top panel, an axisymmetric model with gas particles following perfectly circular motions. Bottom panel, a bisymmetric distortion —such as those produced by bars (see Chapter 2)— was introduced in the inner parts and it twists the isovelocity contours with characteristic "S" shaped distortions.

until values that reproduce the disturbed velocities are found. This is demonstrated for the barred galaxy NGC 1365 in Chapter 3 (see also Zánmar Sánchez et al. 2008).

Most galaxies host tens to hundreds of globular clusters which are nearly spherical systems with masses of $10^4 - 10^6$ $M_\odot$ and sizes of a few parsecs[2]. The majority of these relatively tiny objects are true relics of the early universe and therefore unique probes of galaxy formation. For example, it has been suggested (Peebles 1984) that globular clusters formed at the center of low-mass dark matter halos before the parent galaxy had been assembled. However, their halos are suspected to have been stripped away since

[2]Compare to galaxies which have $10^7 - 10^{13}$ $M_\odot$ and sizes of thousands of parsecs.

globular clusters seem to be devoid of substantial amounts of dark matter as suggested by their declining velocity dispersion profiles (Chapter 4), low mass-to-light ratios (Pryor et al. 1989) and the presence of faint tidal tails on some clusters (Moore 1996). And yet, somewhat "ironically", globular clusters themselves have been used to trace the structure of dark matter halos since they can probe the outer regions of their hosting galaxy (Côté et al. 2003; Richtler et al. 2004).

Globular clusters are also interesting objects in their own right. With our Galaxy hosting some 150 of these stellar systems, their proximity and apparent simplicity make them ideal testbeds for dynamical studies. Indeed, in contrast with most extragalactic studies, individual stars can be resolved and studied individually. This allows, for example, the measurement of velocities of stars that are necessary to constrain the mass and other dynamical aspects of these systems. Chapter 4 is devoted to a first survey of line-of-sight velocities for one of the 29 galactic clusters in Messier's catalog: M80. We use our new kinematic information to study its rotation, velocity dispersion, and mass-to-light ratio and to constrain its expected tidal mass stripping given its proximity to our Galaxy's center.

Bibliography

Athanassoula, E., Bosma, A., & Papaioannou, S. 1987, A&A, 179, 23

Bahcall, J. N., & Casertano, S. 1985, ApJ, 293, L7

Bell, E. F., & de Jong, R. S. 2001, ApJ, 550, 212

Bosma, A. 1978, PhD thesis, Groningen Univ.

Bottema, R. 1997, A&A, 328, 517

Clowe, D., Luppino, G. A., Kaiser, N., & Gioia, I. M. 2000, ApJ, 539, 540

Côté, P., McLaughlin, D. E., Cohen, J. G., & Blakeslee, J. P. 2003, ApJ, 591, 850

Fischer, P., McKay, T. A., Sheldon, E., Connolly, A., Stebbins, A., Frieman, J. A., Jain, B., Joffre, M., Johnston, D., Bernstein, G., Annis, J., Bahcall, N. A., Brinkmann, J., Carr, M. A., Csabai, I., Gunn, J. E., Hennessy, G. S., Hindsley, R. B., Hull, C., Ivezić, Ž., Knapp, G. R., Limmongkol, S., Lupton, R. H., Munn, J. A., Nash, T., Newberg, H. J., Owen, R., Pier, J. R., Rockosi, C. M., Schneider, D. P., Smith, J. A., Stoughton, C., Szalay, A. S., Szokoly, G. P., Thakar, A. R., Vogeley, M. S., Waddell, P., Weinberg, D. H., York, D. G., & The SDSS Collaboration. 2000, AJ, 120, 1198

Kent, S. M. 1986, AJ, 91, 1301

Kormendy, J., & Kennicutt, Jr., R. C. 2004, ARA&A, 42, 603

Lake, G., & Feinswog, L. 1989, AJ, 98, 166

Moore, B. 1996, ApJ, 461, L13

Palunas, P. 1996, PhD thesis, Rutgers The State University of New Jersey - New Brunswick

Peebles, P. J. E. 1984, ApJ, 277, 470

Pryor, C., McClure, R. D., Fletcher, J. M., & Hesser, J. E. 1989, AJ, 98, 596

Richtler, T., Dirsch, B., Gebhardt, K., Geisler, D., Hilker, M., Alonso, M. V., Forte, J. C., Grebel, E. K., Infante, L., Larsen, S., Minniti, D., & Rejkuba, M. 2004, AJ, 127, 2094

Sellwood, J. A., & Wilkinson, A. 1993, Reports on Progress in Physics, 56, 173

Sheth, K., Elmegreen, D. M., Elmegreen, B. G., Capak, P., Abraham, R. G., Athanassoula, E., Ellis, R. S., Mobasher, B., Salvato, M., Schinnerer, E., Scoville, N. Z., Spalsbury, L., Strubbe, L., Carollo, M., Rich, M., & West, A. A. 2008, ApJ, 675, 1141

Slipher, V. M. 1914, Lowell Observatory Bulletin, 2, 66

Spekkens, K., & Sellwood, J. A. 2007, ApJ, 664, 204

Springel, V., Frenk, C. S., & White, S. D. M. 2006, Nature, 440, 1137

Tegmark, M., Eisenstein, D. J., Strauss, M. A., Weinberg, D. H., Blanton, M. R., Frieman, J. A., Fukugita, M., Gunn, J. E., Hamilton, A. J. S., Knapp, G. R., Nichol, R. C., Ostriker, J. P., Padmanabhan, N., Percival, W. J., Schlegel, D. J., Schneider, D. P., Scoccimarro, R., Seljak, U., Seo, H.-J., Swanson, M., Szalay, A. S., Vogeley, M. S., Yoo, J., Zehavi, I., Abazajian, K., Anderson, S. F., Annis, J., Bahcall, N. A., Bassett, B., Berlind, A., Brinkmann, J., Budavari, T., Castander, F., Connolly, A., Csabai, I., Doi, M., Finkbeiner, D. P., Gillespie, B., Glazebrook, K., Hennessy, G. S., Hogg, D. W., Ivezić, Ž., Jain, B., Johnston, D., Kent, S., Lamb, D. Q., Lee, B. C., Lin, H., Loveday, J., Lupton, R. H., Munn, J. A., Pan, K., Park, C., Peoples, J., Pier, J. R., Pope, A., Richmond, M., Rockosi, C., Scranton, R., Sheth, R. K., Stebbins, A., Stoughton, C., Szapudi, I., Tucker, D. L., Berk, D. E. V., Yanny, B., & York, D. G. 2006, Phys. Rev. D, 74, 123507

van Albada, T. S., Bahcall, J. N., Begeman, K., & Sancisi, R. 1985, ApJ, 295, 305

Verheijen, M. A. W., Bershady, M. A., Andersen, D. R., Swaters, R. A., Westfall, K., Kelz, A., & Roth, M. M. 2004, Astronomische Nachrichten, 325, 151

Weiner, B. J., Sellwood, J. A., & Williams, T. B. 2001, ApJ, 546, 931

Zánmar Sánchez, R., Sellwood, J. A., Weiner, B. J., & Williams, T. B. 2008, ApJ, 674, 797

Chapter 2

Quantifying Non-circular Streaming Motions in Disk Galaxies

The centrifugal balance of gas on near circular orbits in a galaxy yields a direct estimate of the central attraction, which is the first step towards a model for the mass distribution. The estimation of galaxy rotation curves therefore has a long history (see Sofue & Rubin 2001, for a review).

Well-sampled 2D velocity maps provide sufficient information to identify the rotation center and to test whether the line-of-sight velocity field is, or is not, consistent with a circular flow patttern in an inclined plane about a common rotation center. The widely-used software utility *rotcur* (Begeman 1987) divides the velocity map into a number of elliptical elements that are assumed to be projected circles around which the gas moves on circular orbits. It yields an estimate of the circular speed in each annulus, and has options to fit for, or hold fixed, the rotation center, systemic velocity, position angle and inclination in each annulus. It is uniquely powerful in its ability to extract information when the gas layer is warped.

A number of possible systematic errors in the fitted velocity have been discussed. Beam smearing (van den Bosch & Swaters 2001) is obviously reduced by improved spatial resolution of the observations, *e.g.*, by using optical data when available. Various forms of turbulence – also described as pressure support or as an asymmetric drift (Valenzuela *et al.* 2007) – can be recognized and corrected for in high quality data (Oh *et al.* 2008). However, the most difficult systematic error to correct for is widely believed to be non-circular gas streaming in a non-axisymmetric potential.

Gas streaming on non-circular orbits is clearly not in simple centrifugal balance, and estimation of the azimuthally averaged mass profile is not straightforward. A number of authors have constructed detailed fluid dynamical models of bar (Weiner *et al.* 2001; Zánmar Sánchez *et al.* 2008) or spiral (Kranz *et al.* 2003) flows, which they have used to estimate the mass of the visible component. This powerful approach is too time-consuming for routine use, however.

Not only do non-circular motions arise from bars and other visible distortions, but they may also be caused by expected asphericities in dark matter halos (*e.g.* Jing & Suto 2002; Allgood *et al.* 2006; Hayashi *et al.* 2007), although their shapes are expected to be made rounder by disk formation (*e.g.* Dubinski 1994; Debattista *et al.* 2008). Indeed, Hayashi & Navarro (2006) argue that halo-driven non-axisymmetric streaming motions in the inner disc may mask a central cusp in the halo density. Furthermore, gas in the outer discs may flow in an elliptical streaming pattern in response to forcing by a non-axisymmetric halo.

It is therefore desirable to be able to identify non-circular streaming motions in high-quality 2D velocity maps and to correct for their influence in an estimate of the average central attraction. Here we show how the bisymmetric model proposed by (Spekkens & Sellwood 2007, hereafter SS07) can be used to place bounds on the streaming motions possibly induced by an aspherical dark matter halo, and to extract an improved estimate of the central attraction when the flow pattern is characterized by non-circular streaming about a fixed axis. We illustrate the advantages of the method, which was first applied to NGC 2976 (SS07), for a number of other galaxies from the THINGS (Walter *et al.* 2008) and BHαBar (Hernandez *et al.* 2005) galaxy samples.

2.1 Fitting Non-circular Motions

Non-circular flow patterns have long been recognized (*e.g.* Bosma 1978) as velocity "wiggles" or larger-scale distortions of the isovelocity contours in well-sampled 2D velocity maps. The velocity of a particle in the plane of the disk of a galaxy can be decomposed into radial,

V_r, and tangential, V_t, components which in turn can be expanded as follows:

$$V_t(r,\theta) = \bar{V}_t(r) + \sum_{m=1}^{\infty} V_{m,t}(r)\cos\left[m\theta + \theta_{m,t}(r)\right] \tag{2.1}$$

and

$$V_r(r,\theta) = \bar{V}_r(r) + \sum_{m=1}^{\infty} V_{m,r}(r)\cos\left[m\theta + \theta_{m,r}(r)\right], \tag{2.2}$$

here the coefficients $V_{m,t}$ and $V_{m,r}$, and the angular phases $\theta_{m,t}$ and $\theta_{m,r}$ are all functions of the distance r to the center of the galaxy. Galaxies are observed in projection and therefore the observed line-of-sight velocities are $V_{\rm obs} = V_{\rm sys} + \sin i(V_t\cos\theta + V_r\sin\theta)$, where $V_{\rm sys}$ is the systemic velocity of the galaxy, i is the inclination about the major axis of the galaxy and the angle θ is zero at the position angle ϕ_d'. Substituting the above Fourier expansions and simplifying yields:

$$\begin{aligned}\frac{V_{\rm obs} - V_{\rm sys}}{\sin i} &= \bar{V}_t\cos\theta + \sum_{m=1}^{\infty}\frac{V_{m,t}}{2}\left\{\cos\left[(m+1)\theta + \theta_{m,t}\right] + \cos\left[(m-1)\theta + \theta_{m,t}\right]\right\} + \\ &\quad \bar{V}_r\sin\theta + \sum_{m=1}^{\infty}\frac{V_{m,r}}{2}\left\{\sin\left[(m+1)\theta + \theta_{m,r}\right] - \sin\left[(m-1)\theta + \theta_{m,r}\right]\right\}\end{aligned} \tag{2.3}$$

Thus, projection complicates the determination of the Fourier coefficients by introducing degenerate azimuthal variations of orders $m' = m \pm 1$ for the intrinsic sectoral harmonic m, as is well known (*e.g.*, Canzian 1993; Schoenmakers *et al.* 1997). At least two different approaches have been proposed to simplify and interpret equation 2.3 and here we summarize and compare both methods and their respective software incarnations.

Schoenmakers *et al.* (1997) and Schoenmakers (1999) estimate the potential distortion from an harmonic analysis of the line-of-sight velocities. This approach is embodied in the tool *reswri*, an extension of *rotcur*, which was used by Trachternach *et al.* (2008, hereafter TBWBK) for the THINGS sample (Walter *et al.* 2008) and for a sample of dwarf galaxies by van Eymeren *et al.* (2009). Small values of the fitted non-axisymmetric coefficients can be related to the magnitude of the potential distortion.

It should be noted that non-circular motions are readily confused with the kinematic signature of a warp, since both cause variations in the ellipticity and position angle of the

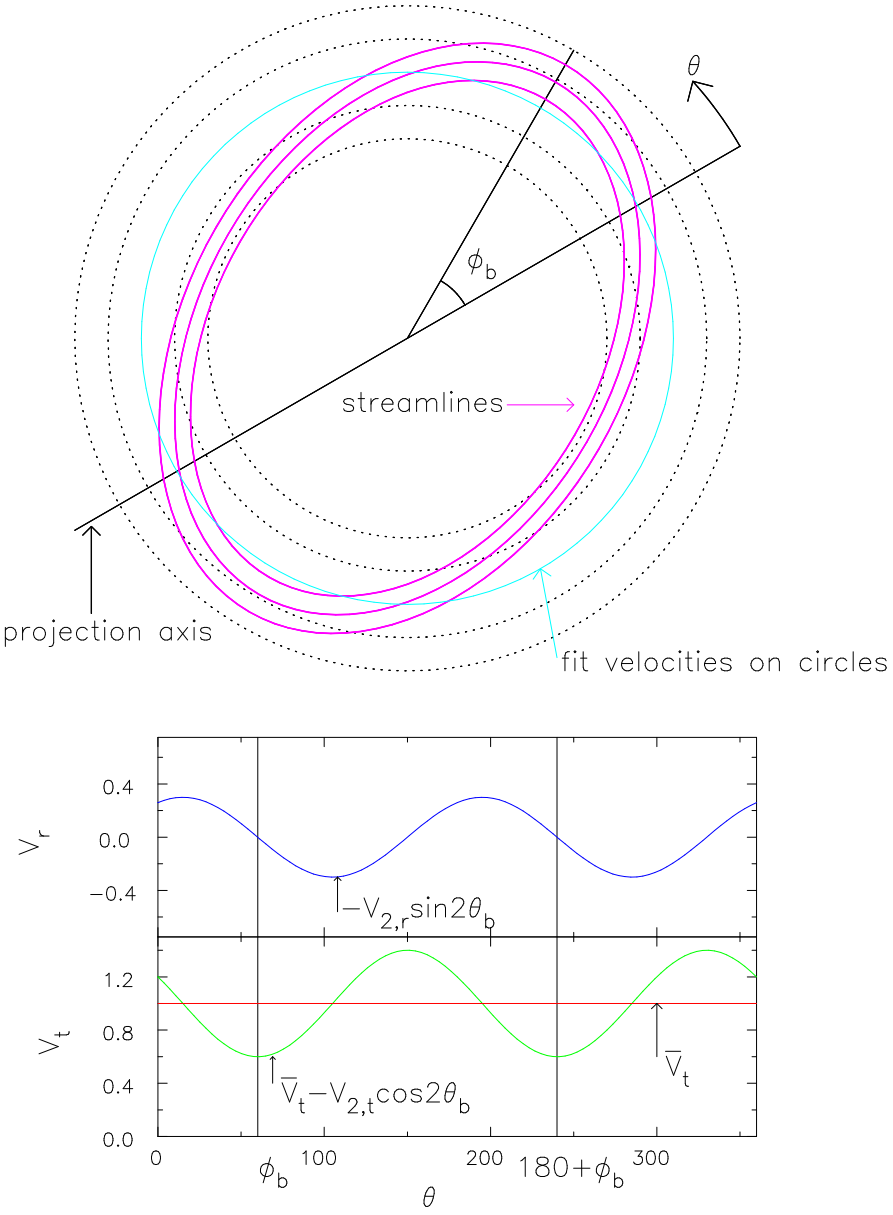

Figure 2.1 A schematic illustration of the approach taken by Spekkens & Sellwood (2007). The magenta lines in the upper panel indicate non-circular streamlines in the disc plane, which is shown face-on. The galaxy is observed in projection, with the intersection of the sky-plane and the disc plane making an angle ϕ_b to the major axis of the elliptical streamlines. Our model of the flow consists of a set of values for $\bar{V}_t$, $V_{2,t}$ and $V_{2,r}$ around rings (dotted) at fixed radii. We project the model and fit to the observed data, using linear interpolation to predict data values between rings.
The lower panels illustrate the bisymmetric variations of the radial and azimuthal model velocities (arbitrary scale) in the disc plane around the cyan circle in the upper panel. The radial velocity (blue) varies with angle $\theta_b = \theta - \phi_b$ to the major axis of the elliptical streaming pattern as $-V_{2,r} \sin 2\theta_b$. The azimuthal velocity (green) varies as $-V_{2,t} \cos 2\theta_b$ about the mean ($\bar{V}_t$ shown in red). This physically-motivated phase difference between the two non-axisymmetric components is embodied in the fit.

flow pattern.[1] Thus, if the projection geometry is allowed to vary from ring to ring, then a large part of the actual non-circular motion may be masked by radial variations in the position angle (PA) and inclination (i). Therefore van Eymeren *et al.* (2009) advocate constraining i & PA to have the same values at all radii. On the other hand, TBWBK justified allowing individual tilts for rings in all the THINGS galaxies from the fact that the magnitudes of non-circular streaming motions in two galaxies (NGC 3198 & DDO 154) were little changed when i & PA were allowed to vary compared with when they were constrained to be constant with radius. Here we show that allowing rings to tilt independently led them to miss a significant non-axisymmetric distortion in at least two galaxies: NGC 2976 & NGC 7793.

The tool *reswri* has a number of disadvantages. First, their method is still subject to the complication $m' = m \pm 1$ introduced by projection as described above (eq. 2.3. Second, it assumes the perturbed velocities are small so that it cannot handle strong perturbations. Third, the estimated circular speed, $V_c(R)$, is biased to the value on the major axis of the projection, see below. Fourth, it treats each ring independently, implying that a mild distortion that is coherent over a significant radial range is more easily masked by noise. Fifth, an estimate of the strength of the mild potential distortion responsible for the detected non-axisymmetric flow requires an undesirable difference between two of the fitted coefficients (as a consequence of the first disadvantage) and also includes the sine of an angle whose value cannot be determined from this approach.

SS07 therefore proposed an alternative approach, the bisymmetric model embodied in the software tool *velfit* (illustrated in Fig. 2.1), which differs at root by postulating a specific model of the flow that includes a possible non-circular streaming pattern about a fixed direction in the disc plane. We refer to this as a "bar model" as a convenient term that encompasses any straight bisymmetric distortion no matter what its origin or amplitude.

[1] In fact, the kinematic signatures of an oval potential and a warp are degenerate only when the principal axis of the potential coincides with either the major or minor axis of the projection (Pence & Blackman 1984; Franx, van Gorkom & de Zeeuw 1994).

Fitting of such a model to the projected data avoids the complications caused by the coupling of different angular periodicities. In particular, SS07 assume a flat disc plane and a distortion having a fixed orientation at all radii, although its amplitude may vary with R. The tool *velfit* then fits the projected model velocity at a general point (eq. 5, of SS07):

$$\begin{aligned} V_{\rm model} \;\; = \;\; V_{\rm sys} + \sin i \;\; \big[\bar{V}_t \cos\theta \; - \; V_{2,t} \cos 2(\theta - \phi_b) \cos\theta \\ - V_{2,r} \sin 2(\theta - \phi_b) \sin\theta \, \big] \, , \end{aligned} \tag{2.4}$$

to derive $\bar{V}_t(R)$, $V_{2,t}(R)$, $V_{2,r}(R)$, the angle ϕ_b, the systemic velocity $V_{\rm sys}$, and i & PA (these quantities are defined in the caption to Fig. 2.1). The code allows the radial extent of the distortion to be restricted, if desired, while a simple axisymmetric flow is fitted over the remainder of the data. SS07 describe the algorithm in detail.

This tool avoids all the above-listed disadvantages of the method devised by Schoenmakers *et al.* (1997), as follows. (1) It can fit for arbitrarily large distortions because does not require $V_{2,t}(R)$ & $V_{2,r}(R)$ to be related by the epicycle approximation. (2) It yields $\bar{V}_t$, which is an improved estimate of the average orbital speed at each radius, as discussed below. (3) It uses all the data in a single fit, making it easier to identify coherent mild distortions in noisy data and to go some way towards "averaging over" small-scale spiral streaming. (4) The magnitude of a mild potential distortion is much more directly related to the fitted velocity coefficients, as we show in section 2.2.

The assumption of a flat disc plane is equivalent to requiring constant i & PA in *reswri*, as van Eymeren *et al.* (2009) recommend, except that *velfit* has the further advantage that it determines the optimal values as part of the fit. It is justified for the inner parts of spiral galaxy discs, which are believed to be flat: warps generally start near the edge of the optical disc (*e.g.* Briggs 1990) and the massive inner disk is coherent enough to resist bending (Shen & Sellwood 2006).

With the projection angles held fixed, it may seem from Fig. 2.1 that fitting a simple circular flow model, *e.g.* with *rotcur*, would yield the same $\bar{V}_t$ as a bisymmetric model

from *velfit*. However, the estimated circular speeds for an axisymmetric model are biased towards values on the major axis where orbital velocities are directed most closely into the line-of-sight. Since gas moving on elliptical orbits has its smallest orbital speed at apocenter,[2] the fitted $\bar{V}_t$ is biased low when the streaming pattern is closely aligned with the major axis. Conversely, we should expect an axisymmetric fit to be biased high by the higher-than-average speed of the gas near pericenter when the bar is oriented close to the projected minor axis, and to yield a fair estimate of $\bar{V}_t$ when the bar is at intermediate angles. Note also that even though $\bar{V}_t$ is a fairer estimate than that from an axisymmetric fit, it is not the circular speed in the equivalent axisymmetric potential, as is evident from Fig. 2.1.

Because *reswri* fits each ring independently, it is not easy to apply a smoothing constraint to the fit. Spiral arms, turbulence, *etc.*, produce localized distortions to the flow that can lead to "wiggles" in the fitted velocities, as well as small-scale variations in $V_{\rm sys}$, i, & PA. The user of *reswri* can, and probably should, hold these global parameters fixed, but the tool does not have the option to smooth the fitted velocities. While excessive smoothing is clearly dangerous, *e.g.* it could reduce the slope of the inner rotation curve, a small degree of smoothing applied to constrain the fit can be beneficial. In Appendix A we describe how an optional radial smoothing penalty can be applied within *velfit* to the fitted functions $\bar{V}_t(R)$, $V_{2,t}(R)$, & $V_{2,r}(R)$; the magnitude of the penalty can be set independently for the axisymmetric and non-axisymmetric terms.

One weakness of *velfit* is that it tends to return absurd velocities when the bar angle, ϕ_b, is near zero or 90° because a degeneracy arises between the velocity components at these special orientations. To see this, consider equation (2.4) for the predicted projected velocity when $\phi_b = 0$: the products $\cos 2\theta \cos\theta$ and $\sin 2\theta \cos\theta$, can be separated into a part that varies as $\cos\theta$ and another that varies as $\cos 3\theta$ or $\sin 3\theta$. Therefore $\bar{V}_t$ is partly

[2]This statement is independent of the angular rotational speed of the potential that drives the non-circular flow. Even in strong bars, where angular momentum is not approximately conserved, gas at apocenter of the stream lines must be moving slower than the average since it plunges inwards after that point.

degenerate with both $V_{2,t}$ and $V_{2,r}$, and a similar partial degeneracy arises when $\phi_b = 90°$. In principle, the 3θ variation of the model breaks the degeneracy, but these more rapid angular variations are more susceptible to noise, and the "best fit" values of the three velocity components can be absurd. We show an example in section 2.3.3, where we also explain how to combat the problem.

As already indicated, *velfit* assumes a distortion about a fixed axis with prescribed phase relations between the non-axisymmetric coefficients that imply the distortion has no spirality. The bisymmetric flow sketched in Fig. 2.1 does not, however, imply that the code can fit only bars, or oval features, although that is its most useful application. The same code can be used to fit models having higher or lower rotational symmetry. Experience indicates, however, that nothing useful results from generalizing to fit for more than a single distortion at once.

It should be noted that *velfit* is purely a fitting procedure. It does not, in general, yield a direct estimate of the mass responsible for the fitted velocity distortions, except when departures from axial symmetry are mild, as we now show.

2.2 Mildly Distorted Potentials

Where the forced non-circular speeds are a small fraction of the circular speed, we can use the formulae for the orbits of test particles on near circular orbits in weakly barred potentials from Binney & Tremaine (2008, hereafter BT08).[3] Their equation (3.147a, p190) gives the forced radial displacement as a function of time, which can easily be differentiated to find the forced radial speed. The radial velocity at radius R_0 varies sinusoidally with amplitude

$$V_{m,r} = \left[\frac{d\Phi_b}{dR} + \frac{2\Omega\Phi_b}{R(\Omega-\Omega_b)}\right]_{R_0} \frac{m(\Omega_0-\Omega_b)}{\kappa_0^2 - m^2(\Omega_0-\Omega_b)^2}, \tag{2.5}$$

where Φ_b is the weak non-axisymmetric part of the potential that rotates at angular rate Ω_b, and $\Omega(R)$ & $\kappa(R)$ are the usual frequencies of rotation and epicycle motion for mildly

[3]Gas streamlines trace test particle orbits when pressure and magnetic forces can be neglected.

eccentric orbits. We make a number of assumptions in order to simplify this formula: we assume $\Omega_b \ll \Omega_0$ since we suspect the halo to be rotating slowly, we set $\kappa_0^2 = 2\Omega_0^2$ for a flat rotation curve, and we assume the potential perturbation varies slowly with radius so that $d\Phi_b/dR \ll \Phi_b/R$. With these assumptions, choosing $m = 2$ for a bisymmetric distortion and setting $R_0\Omega_0 = V_c$, the equation for the forced velocity amplitude reduces to

$$V_{2,r} = -\frac{2\Phi_b}{V_c}. \tag{2.6}$$

The time derivative of the equation for the tangential displacement (*e.g.* Sellwood & Wilkinson 1993, eq. 10b), converted to the same notation and abbreviating $\omega = m(\Omega - \Omega_b)$, gives

$$V_{m,t} = \left[\frac{2\Omega}{\omega}\frac{d\Phi_b}{dR} + \frac{4\Omega^2 - \kappa^2 + \omega^2}{\omega^2}\frac{m\Phi_b}{R}\right]_{R_0} \frac{\omega_0}{\kappa_0^2 - \omega_0^2}. \tag{2.7}$$

With the same set of assumptions, this expression reduces to $V_{2,t} \simeq -3\Phi_b/V_c$. Thus if the perturbed velocities are caused by a weak, non-rotating, oval distortion to a quasi-logarithmic potential, we should expect the perturbed velocity coefficients to be in the ratio $V_{2,t} \simeq 1.5V_{2,r}$ and, in particular, they should have the same sign. Note that we do not expect the perturbed coefficients to have this ratio when the oval distortion is strong and/or rapidly rotating, such as for bars, or in the inner parts where the rotation curve is rising.

In order to relate Φ_b to the potential shape, we assume a non-axisymmetric potential of the form (*cf.* eq. 2.71a of BT08)

$$\Phi(R,\theta) = \frac{V_0^2}{2}\ln\left[R_c^2 + R^2\left(1 + \frac{1 - q_\Phi^2}{q_\Phi^2}\sin^2\theta\right)\right], \tag{2.8}$$

where V_0 sets the velocity scale, R_c is the core radius, and q_Φ is the axis ratio of the potential. Expansion of this potential for small $(1 - q_\Phi^2)/q_\Phi^2$, and comparison with the definition of Φ_b in equations (3.136) and (3.143) of BT08, we find $\Phi_b = -V_c^2(1-q_\Phi^2)/(4q_\Phi^2)$. Combining this result with eq. (2.6) and equating $\bar{V}_t$ to V_c, we finally obtain

$$q_\phi = \left(\frac{\bar{V}_t}{\bar{V}_t + 2V_{2,r}}\right)^{1/2}. \tag{2.9}$$

We stress that this formula assumes a mildly distorted, slowly rotating potential and a flat rotation curve, and it will not yield a reliable estimate in other circumstances. As is well known, the density that gives rise to this potential is about three times more elongated than the potential, so that $q_\rho \simeq 1 - 3(1 - q_\Phi)$ (BT08, p. 77).

2.3 Results

Here we apply the tool *velfit* to several galaxies in the THINGS sample (Walter *et al.* 2008). The HI Nearby Galaxy Survey (THINGS) used the Very Large Array operated by the National Radio Astronomy Observatory[4] to make spectral observations of the 21cm line emission of neutral hydrogen in a sample of 34 galaxies. The data are in the public domain. We do not reanalyse the entire THINGS sample here, but choose a few representative galaxies to illustrate the advantages of *velfit* over *reswri*.

We selected data with natural weighting, which have higher signal-to-noise (S/N) and lower spatial resolution than when robust weighting is used, and downloaded maps of the intensity-weighted mean velocity. In order to apply a S/N cut-off, we also downloaded the data cubes. We determined the noise level, σ, from parts of channel maps with no signal, and discarded velocity measurements from the maps for which the peak intensity in any channel $< 5\sigma$.

We do not use the line widths or the formal (generally very low) uncertainties in the mean velocities, but instead assume a constant uncertainty of 10 km s^{-1}. This strategy implies that the shape of, and values on, the χ^2 surface are of no statistical significance; we therefore estimate uncertainties using the bootstrap technique described in Appendix B.

We adopt the beam size as the spacing between the rings in our fits so that each ring is independent. The beam size differs for each galaxy, ranging from $7.41''$ for NGC 2976 to $15.6''$ for NGC 7793. We use the smoothing option, described in Appendix A, for NGC 2903

[4]NRAO is a facility of the National Science Foundation operated under cooperative agreement by Associated Universities Inc.

Table 2.1 Best-fit parameters for NGC 2976 and NGC 7793

	NGC 2976	NGC 7793
Systemic vel. (km s^{-1})	1.58 ± 0.12	226.87 ± 0.13
Disc inclination i	$60\overset{\circ}{.}51 \pm 1\overset{\circ}{.}03$	$44\overset{\circ}{.}37 \pm 4\overset{\circ}{.}68$
Disc PA, ϕ'_d	$323\overset{\circ}{.}37 \pm 0\overset{\circ}{.}80$	$291\overset{\circ}{.}98 \pm 0\overset{\circ}{.}36$
Bar axis ϕ_b	$-29\overset{\circ}{.}48 \pm 5\overset{\circ}{.}90$	$50\overset{\circ}{.}64 \pm 8\overset{\circ}{.}02$
Projected bar axis ϕ'_b	$307\overset{\circ}{.}82 \pm 2\overset{\circ}{.}98$	$333\overset{\circ}{.}068 \pm 7\overset{\circ}{.}28$

only.

2.3.1 NGC 2976: A Case Study

NGC 2976 is a nearby dwarf galaxy in the THINGS sample which was also studied in great detail by Simon *et al.* (2003). Velocity maps have therefore been made using the 21 cm line of HI, the optical Hα emission lines, and the ^{12}CO($J = 1 \rightarrow 0$) line. Clear distortions are visible in all three velocity maps, indicating departures from a simple, coplanar axisymmetric flow.

Simon *et al.* (2003) fitted their data with a model that combined the usual circular flow pattern with an axisymmetric radial flow. SS07 found that an oval or bar-like distortion could yield an equally good fit to the same data. TBWBK find that a tilted ring model fits the HI data, which they conclude is consistent with tiny deviations from a round potential, albeit with a $\lesssim 30^\circ$ variation in the inclination and a similar change of PA in the inner part of the galaxy.

Fig. 2.2(a) shows our fit to the same HI observations used by TBWBK when we assume a flat disc plane and fit for bisymmetric flows to $R = 105''$ only. The error bars show $\pm\sigma$ uncertainties from the bootstrap. de Blok *et al.* (2008) report a mild warp for $R \gtrsim 125''$, but we exclude data at these large radii because they have low S/N. While our estimate of PA (Table 2.1) is in good agreement with that derived from the same HI data by de Blok *et al.* (2008), our value of the inclination is somewhat lower than the $i = 65^\circ$ they adopted, although their value is estimated from the restricted annular range $80'' \leq R \leq 110''$, whereas ours is from a global fit that includes bi-symmetric streaming over most of the disc. Fig. 2.3

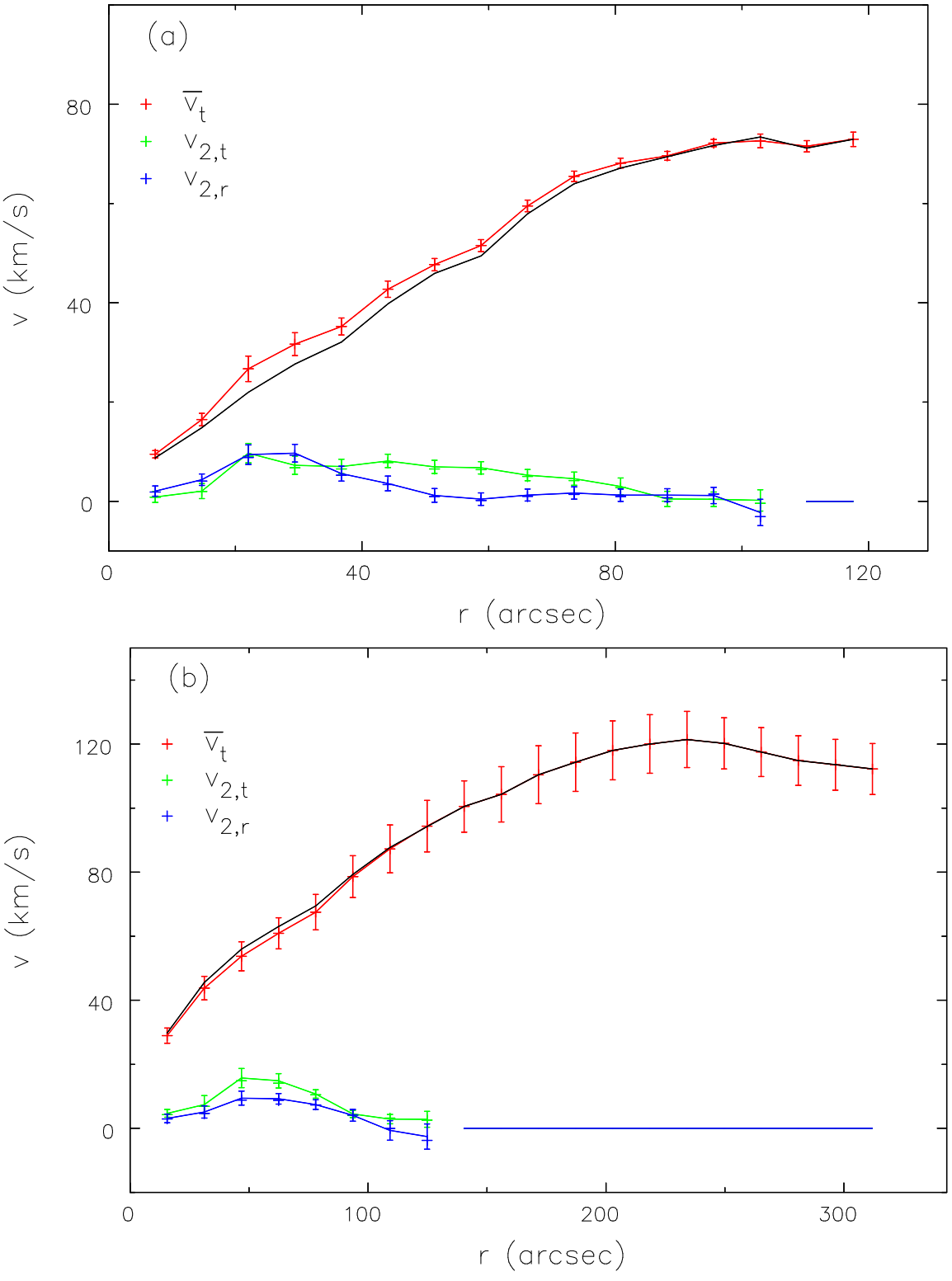

Figure 2.2 Our best fit rotation curve and streaming velocities derived using *velfit* on the THINGS data for (a) NGC 2976 and (b) NGC 7793. The black line shows the result of an axisymmetric fit to all radii and the error bars represent $\pm\sigma$ uncertainties.

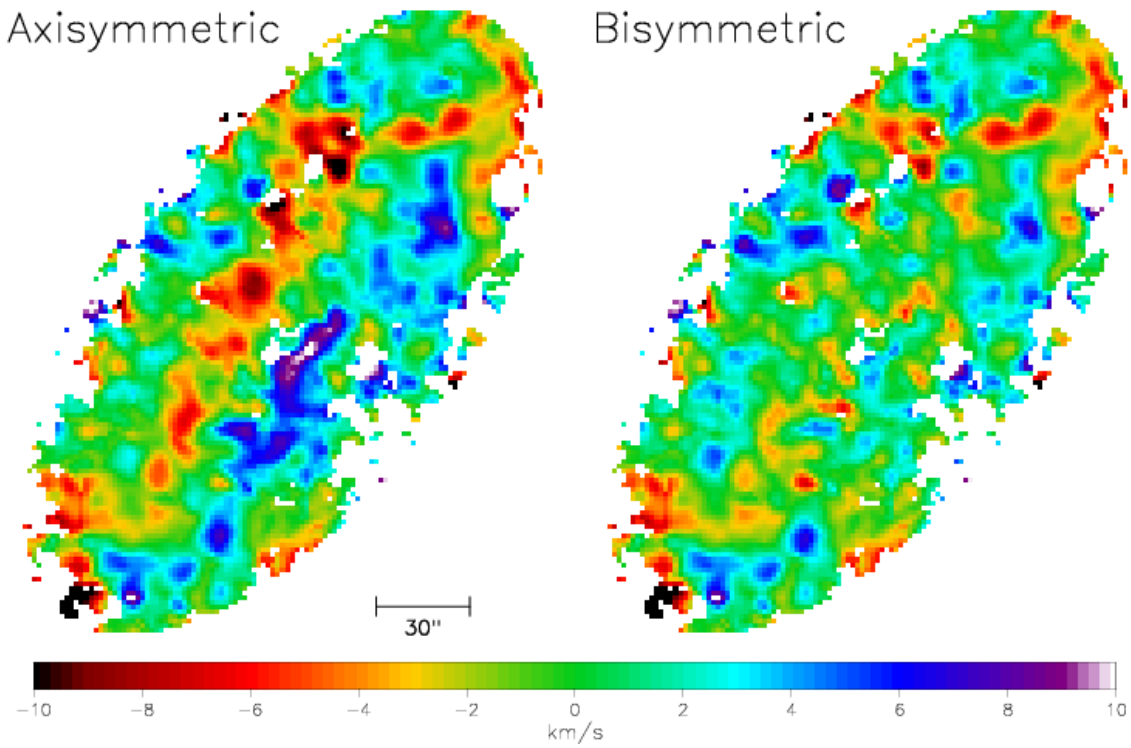

Figure 2.3 Residual maps for axisymmetric (left) and bisymmetric (right) fits to NGC 2976.

shows residual maps for the axisymmetric (left) and bisymmetric (right) fits. The latter is clearly a better representation of the data since it removes most of the blue-red systematic residuals in the inner regions where the bisymmetric model was applied.

We find clear non-circular streaming motions (Fig. 2.2a) in the inner galaxy in these HI data that are similar to, but somewhat smaller than, those found by SS07 from the combined Hα and CO data. We also find a smaller inclination angle than $i \sim 64°$ fitted by SS07. The origin of these differences is clearly due to fitting different datasets, with the slightly lower-resolution HI data arising from a different physical component. These differences are clearly seen in Fig. 2.4 where we have subtracted HI velocities from about 1000 Hα velocities measurements from optical fibers (Simon *et al.* 2003). We have interpolated the residuals to render it clearer and drew a $120''$ long line to illustrate the bisymmetric angle. Although most residuals are small (~ 6 km s^{-1}) they seem to be systematic and consistent with the bisymmetric amplitudes being larger in the Hα map as we have found (*e.g.*, the Hα velocities are smaller at apocenter and larger at pericenter than those from HI). Note

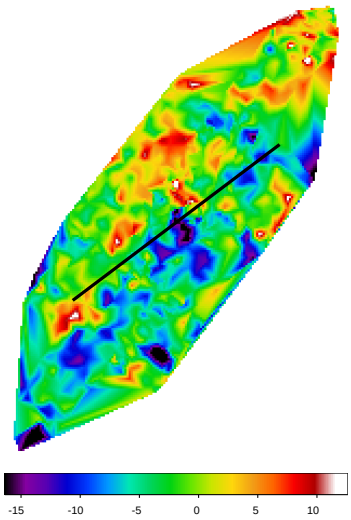

Figure 2.4 Difference in km s^{-1} between the Hα and HI observations. The map was created by interpolating about 1000 different pointings.

that the small difference in systemic velocities between the two datasets causes the center color (green) not to be at exactly zero velocity.

We estimate the projected orientation of the bar or oval to be $\phi_b' \simeq 308^\circ \pm 3^\circ$, which is barely consistent with the $\sim 315^\circ \pm 4^\circ$ estimated (from different data) by SS07. The difference in angles implies that the bar is slightly farther from the major axis, which in turn reduces the difference (Fig. 2.2a) between $\bar{V}_t$ and the axisymmetric fit, for the reason given in section 2.1. Note, however, that we obtain a projected bar angle in closer agreement with that estimated by SS07 if we fix the galaxy inclination at their estimated value.

Since all three models, with radial flows (Simon *et al.* 2003), a twisted disc TBWBK, or oval streaming (SS07 and Fig. 2.2a), are adequate fits to the data, there is no statistical reason to prefer one over another. However, the oval streaming model both avoids the "continuity problem" inherent in radial flow models, and also avoids a strong twist in the plane of the inner disc; TBWBK suggest the disc plane at $R \sim 20''$ ($\simeq 300$ pc) is inclined to the plane of the main part of disc at $R \sim 1.5$ kpc by $\sim 30^\circ$, while the light distribution does not give any indication of such an unusual feature.

2.3.2 Effects of bar orientation

The value of $\bar{V}_t$ in Fig. 2.2(a), while smaller than obtained from different data by SS07, is higher than results from a purely axisymmetric flow fit, shown by the black line. The bisymmetric fitted $\bar{V}_t$ is larger in this case because the "bar" is oriented such that its principal axis is not far from to the major axis of projection for the galaxy, as discussed in section 2.1. We therefore also present a case where the bisymmetric fit has little effect on $\bar{V}_t$.

Fig. 2.2(b) shows a fit to the THINGS data for NGC 7793. As always, we attempt to fit only the flat part of the disc; in this galaxy, de Blok *et al.* (2008) find a mildly varying disc inclination over the entire radial range, but the PA clearly rises steadily for $R \gtrsim 320''$, which we interpret as the start of a warp. We fit a bisymmetric flow over the inner disk $R < 125''$ only and an axisymmetric model to $R = 320''$. The best fit parameters and uncertainties are given in Table 2.1. Our best-fit i & PA are in good agreement with the values estimated by de Blok *et al.* (2008) from their tilted ring analysis. Residual maps (Fig. 2.5) clearly show how the bisymmetric model fitted to the inner region removes the bisymmetric residuals there.

The uncertainty in our estimate of the inclination is, however, rather larger than in other cases, possibly because of spiral streaming in the outer disc (see Fig. 2.5), which is not included in our model, or perhaps because the entire disk is warped, as suggested by TBWBK. Their explanation seems the more likely because the bootstrap values for this parameter have a distinctly bimodal distribution symmetrically distributed about the best-fit value; conservatively, we estimate the uncertainty from the rms spread of the bootstrap iterations. The uncertainty in the inclination is reflected in the uncertainties in the velocities, which therefore seem large relative to the smoothly varying means.

We find clear evidence (Fig. 2.2b) for non-circular streaming in the inner parts. Since we find $\phi_b \simeq 49°$, the estimated "rotation curve" from the bisymmetric fit is in close agreement with that from the simple circular flow model, as expected from the discussion

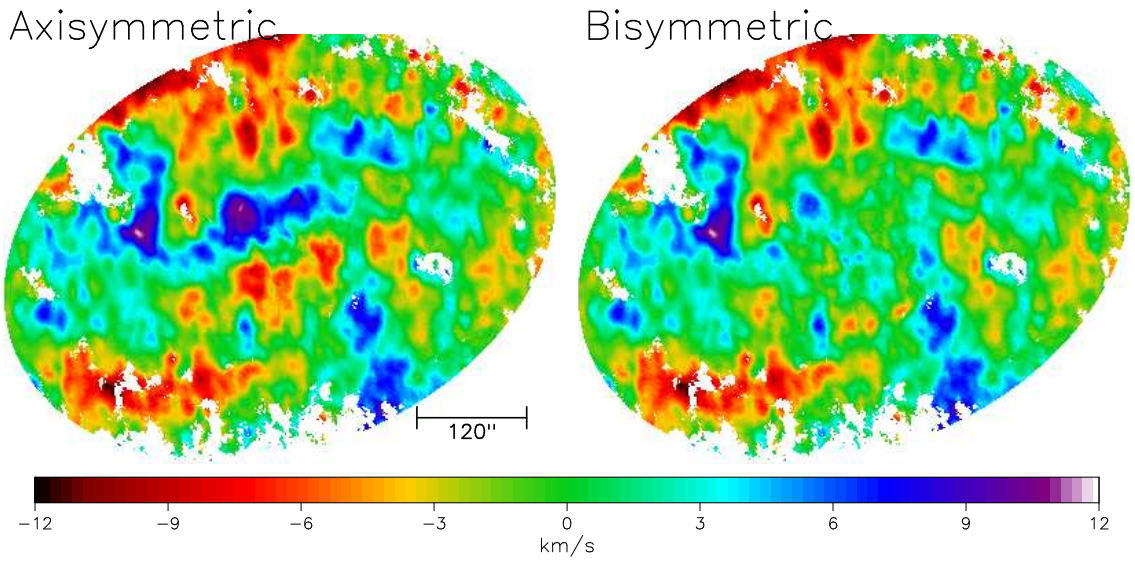

Figure 2.5 Residual maps for axisymmetric (left) and bisymmetric (right) fits to NGC 7793.

Table 2.2 Best-fit parameters for NGC 2903

	THINGS data	BHαBar data
Systemic vel. (km s^{-1})	549.85 ± 0.26	554.12 ± 0.48
Disc inclination i	$63\overset{\circ}{.}65 \pm 0\overset{\circ}{.}71$	$66\overset{\circ}{.}01 \pm 3\overset{\circ}{.}03$
Disc PA, ϕ'_d	$201\overset{\circ}{.}49 \pm 0\overset{\circ}{.}49$	$203\overset{\circ}{.}97 \pm 1\overset{\circ}{.}16$
Bar axis ϕ_b	$5\overset{\circ}{.}75 \pm 14\overset{\circ}{.}31$	$-12\overset{\circ}{.}27 \pm 7\overset{\circ}{.}53$
Projected bar axis ϕ'_b	$204\overset{\circ}{.}05 \pm 6\overset{\circ}{.}38$	$198\overset{\circ}{.}92 \pm 4\overset{\circ}{.}24$
Smoothing penalty, λ	2.6×10^{-6}	6.6×10^{-5}

in section 2.1.

2.3.3 Strong bars

TBWBK find non-circular motions that are consistent with a round potential in all the THINGS galaxies, despite the fact their sample contains several galaxies that are quite strongly barred. In these cases, however, the 21cm line emission from the barred region is generally too weak to yield reliable velocity estimates; velocities can be measured in limited patches in some cases, *e.g.* NGC 925, but not anywhere in others, *e.g.* NGC 3627. However, the data from NGC 2903 are good enough over almost the entire barred region ($R \lesssim 60''$) to yield velocities above our S/N threshold, yet TBWBK estimate non-circular motions in the bar region of only ~ 14 km s^{-1}.

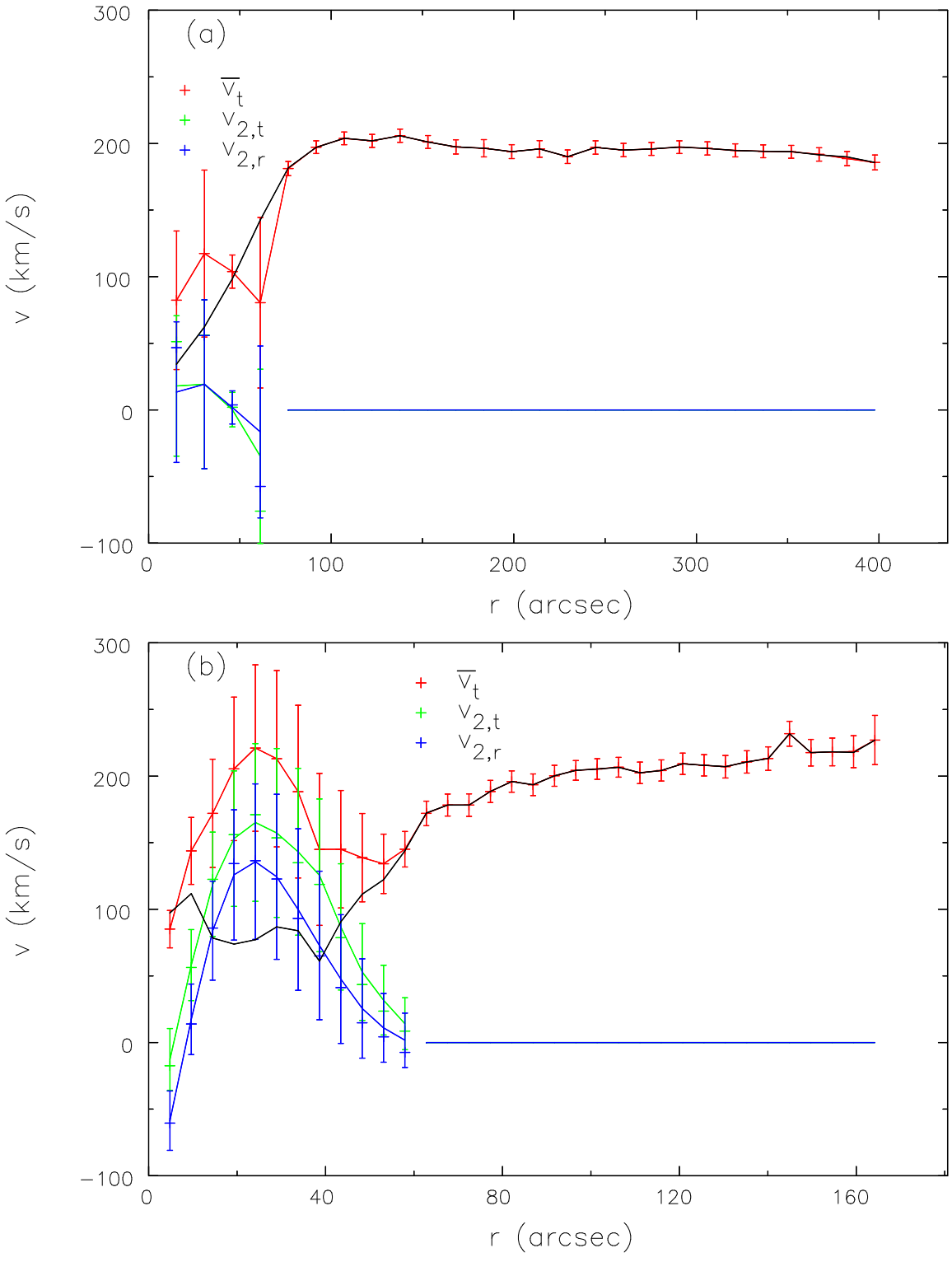

Figure 2.6 Our best fit rotation curve and streaming velocities derived for NGC 2903 using *velfit* on (a) the THINGS data and (b) the BHαBar data – note the different scales.

The application of *velfit* to this galaxy presents a substantial challenge because the bar is so closely aligned with the major axis of projection. As discussed in section 2.1, the velocities $\bar{V}_t$, $V_{2,t}$ & $V_{2,r}$ become harder to distinguish as $|\phi_b| \to 0$, and *velfit* can return unphysically large values for all ($\gg 1000$ km s^{-1} in magnitude), even though they still fit the data well when combined as eq. (2.4). We overcome this problem to a large extent by applying a very slight smoothing penalty, as described in Appendix A. Fig.2.6(a) shows the results from *velfit* applied to the THINGS data for $R < 400''$; the parameters of this fit are given in Table 2.2, when we adopt $\lambda = 2.6 \times 10^{-6}$.

The smoothing penalty successfully eliminates absurd velocities in the bar region obtained from the bootstrap analysis, but at the cost of introducing a strong bias against finding $|\phi_b| \lesssim 2^\circ$. The reason appears to be a ridge in the χ^2 surface as $\phi_b \to 0$ caused by the smoothing penalty, which disfavours the wildly varying velocities that would achieve the smallest residuals. We therefore prefer a very small smoothing penalty since larger values widen the range of disfavoured bar angles even though they further reduce the scatter of fitted velocities from the bootstrap iterations. On the other hand, a very heavy smoothing penalty, such as $\lambda = 0.0052$, leads to an almost linear rise in $\bar{V}_t$, even for the bisymmetric fit, which illustrates the perils of oversmoothing.

Our best-fit estimate of the bar angle is $\phi_b \sim 6^\circ$. It should be noted that neither this angle, nor the best fit values of $\bar{V}_t$ change significantly when we eliminate the smoothing penalty altogether.

Our fitted values of i & PA are in good agreement with those estimated by de Blok *et al.* (2008), and their rotation velocities are in good agreement with our axisymmetric fit, the black line in Fig. 2.6(a), that rises in a quasi-linear fashion from the origin. Naturally, they find wildly varying values of both i and PA in their innermost few rings, whereas *velfit* requires a flat plane and consequently our bisymmetric fit (red line) finds different velocities in this region. We also find significantly larger non-circular speeds in the bar region than those estimated by TBWBK, although they also have large uncertainties and could also be

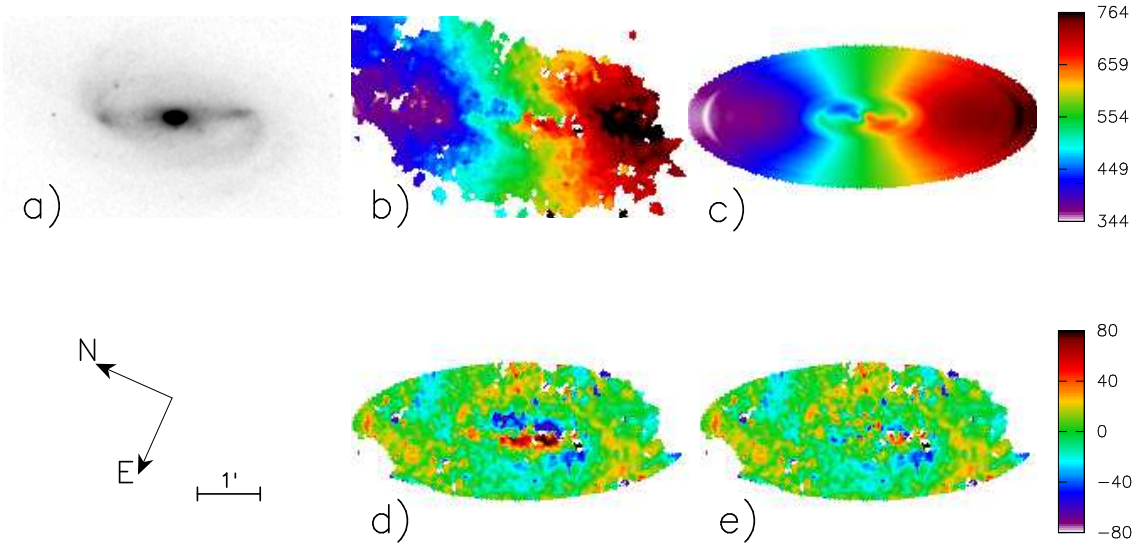

Figure 2.7 (a) An H-band image of NGC 2903 from 2MASS (Skrutskie *et al.* 2006). (b) The velocity map made using the Hα line (Hernandez *et al.* 2005). (c) Our best fit model with a bar flow. (d) Residuals after subtracting the best fit axisymmetric model – note the large values in the bar region. (e) Residuals after subtracting our best fit bi-symmetric flow model. The velocity scales to the right are in km s^{-1}; all images have the same orientation and spatial scale, indicated by the 1′ scale bar.

consistent with a round potential. Thus, the surprisingly weak bar streaming motions are not merely an artefact of *reswri*.

Since the beam width of the HI data we fit is $\sim 15''$ (equal to our ring spacing in *velfit*), it is likely that the HI data is unable to resolve the bar flow.[5] Fortunately, the velocity field of this galaxy has also been mapped at higher spatial resolution in the ^{12}CO($J = 1 \rightarrow 0$) line (Helfer *et al.* 2003) and in Hα using a Fabry-Pérot instrument (Hernandez *et al.* 2005). We here show fits to the Hα data (kindly made available by Olivier Hernandez) since they extend to larger radii than do the CO data, albeit with lower spatial resolution ($4.8''$).

Fig. 2.7(a) shows a 2MASS[6] H-band image of the galaxy, together with (b) the velocity map from the BHαBar survey, (c) our best fit model and (d) & (e) residuals from an axisymmetric and full bar flow fits.

---

[5]Robust weighting of HI data yields velocity maps with higher spatial resolution but lower S/N. For NGC 2903, however, these data from the bar region have too low S/N to allow meaningful fits.

[6]Atlas Image obtained as part of the Two Micron All Sky Survey (2MASS), a joint project of the University of Massachusetts and the Infrared Processing and Analysis Center/California Institute of Technology, funded by the National Aeronautics and Space Administration and the National Science Foundation.

Table 2.2 and Fig. 2.6(b) give the results we obtained from by applying *velfit* to the Hα data for NGC 2903 – note that the radial scales in panels (a) & (b) of Fig. 2.6 differ. We needed to smooth the optical data more heavily ($\lambda = 6.6 \times 10^{-5}$ in this case) in order to eliminate absurdly large velocities in the bootstrap analysis, which introduces a bias, as before, against bar angles close to zero; since this causes a strong skewness in the distribution of bar angles, we estimated the uncertainty in this quantity from only those values more negative than the best fit value. The parameters of the fit to these data are generally in good agreement with those from the HI data, and the projected bar angles differ within their uncertainties.

However, the Hα data show a much more pronounced non-circular flow pattern within the bar region ($R \lesssim 60''$), with perturbed velocities almost as large as $\bar{V}_t$, which in turn significantly exceeds the estimated circular speed from an axisymmetric fit to the same data and the derived $\bar{V}_t$ from the HI data. The fitted velocities from the two datasets are in reasonable agreement outside the bar region, for as far as the optical data extend. The uncertainties in the bar region are still large, and significantly larger than the point to point variation in the best fit suggesting that slightly more aggressive smoothing could be warranted.

Thus beam smearing in the HI data is the reason TBWBK concluded that non-circular motions within the bar were small. Data having better spatial resolution do reveal a pronounced non-circular streaming pattern, as expected for this strongly barred galaxy.

2.3.4 Searching for Aspherical Halos

We here attempt to constrain the shapes of dark matter halos by searching for non-circular streaming motions in the outer discs of the THINGS sample. Since it assumes the galaxy plane to be flat, *velfit* cannot be used in warped regions, which generally arise outside the visible disc. We are therefore restricted to just two galaxies in the sample, NGC 3198 & NGC 2403, for which the extended HI disc is known from the analysis of de Blok *et al.*

Table 2.3 Best-fit parameters for NGC 3198 and NGC 2403

	NGC 3198	NGC 2403
Systemic vel. (km s^{-1})	660.15 ± 0.30	133.50 ± 0.25
Disc inclination i	$70\overset{\circ}{.}37 \pm 0\overset{\circ}{.}30$	$63\overset{\circ}{.}79 \pm 1\overset{\circ}{.}33$
Disc PA, ϕ'_d	$216\overset{\circ}{.}19 \pm 0\overset{\circ}{.}47$	$123\overset{\circ}{.}79 \pm 0\overset{\circ}{.}56$
Bar axis ϕ_b	$46\overset{\circ}{.}29 \pm 13\overset{\circ}{.}69$	$296\overset{\circ}{.}46 \pm 11\overset{\circ}{.}68$
Projected bar axis ϕ'_b	$235\overset{\circ}{.}55 \pm 4\overset{\circ}{.}67$	$82\overset{\circ}{.}21 \pm 4\overset{\circ}{.}79$

(2008) to be approximately coplanar with the inner disc.

Even though these two galaxies are not strongly warped, the analysis of TBWBK, which allows changes in PA and i from ring to ring, may underestimate the ellipticity of the dark matter halos in the disc plane. However, the main advantage of *velfit* over *reswri* in these circumstances is that it searches for a bisymmetric distortion that is coherent over a wide range of radii and could, in principle, detect very mild distortions that might be masked by various sources of noise, such as turbulence and local spiral streaming. Since it is a more sensitive probe of halo shapes, it should either detect mild distortions, if they are present, or place a tighter lower bound on the axis ratio of the potential.

NGC 3198

Fig. 2.8 shows the residual map to $R = 456''$ when a flat, axisymmetric model is subtracted from the THINGS data for NGC 3198. The residual velocities are generally small, peaking at ± 20 km s^{-1}, which is consistent with the small variations in i & PA for $r > 200''$ reported by de Blok *et al.* (2008). However, the residual pattern reveals clear indications of mild spiral arm streaming, even far outside the optical disc ($R_{25} \simeq 255''$ in the B-band de Vaucouleurs *et al.* 1991).

In order to search for a possible mildly non-axisymmetric halo, we tried fitting a bisymmetric model, with no spirality, to the outer disc. Such a model may be able to identify a weak bar flow that could be buried in the spiral noise. The parameters of our best fit model, which includes a bisymmetric flow for $R \gtrsim 220''$, are listed in Table 2.3. Our estimated values of $V_{\rm sys}$, i, & PA are in excellent agreement with those given by de Blok *et al.* (2008).

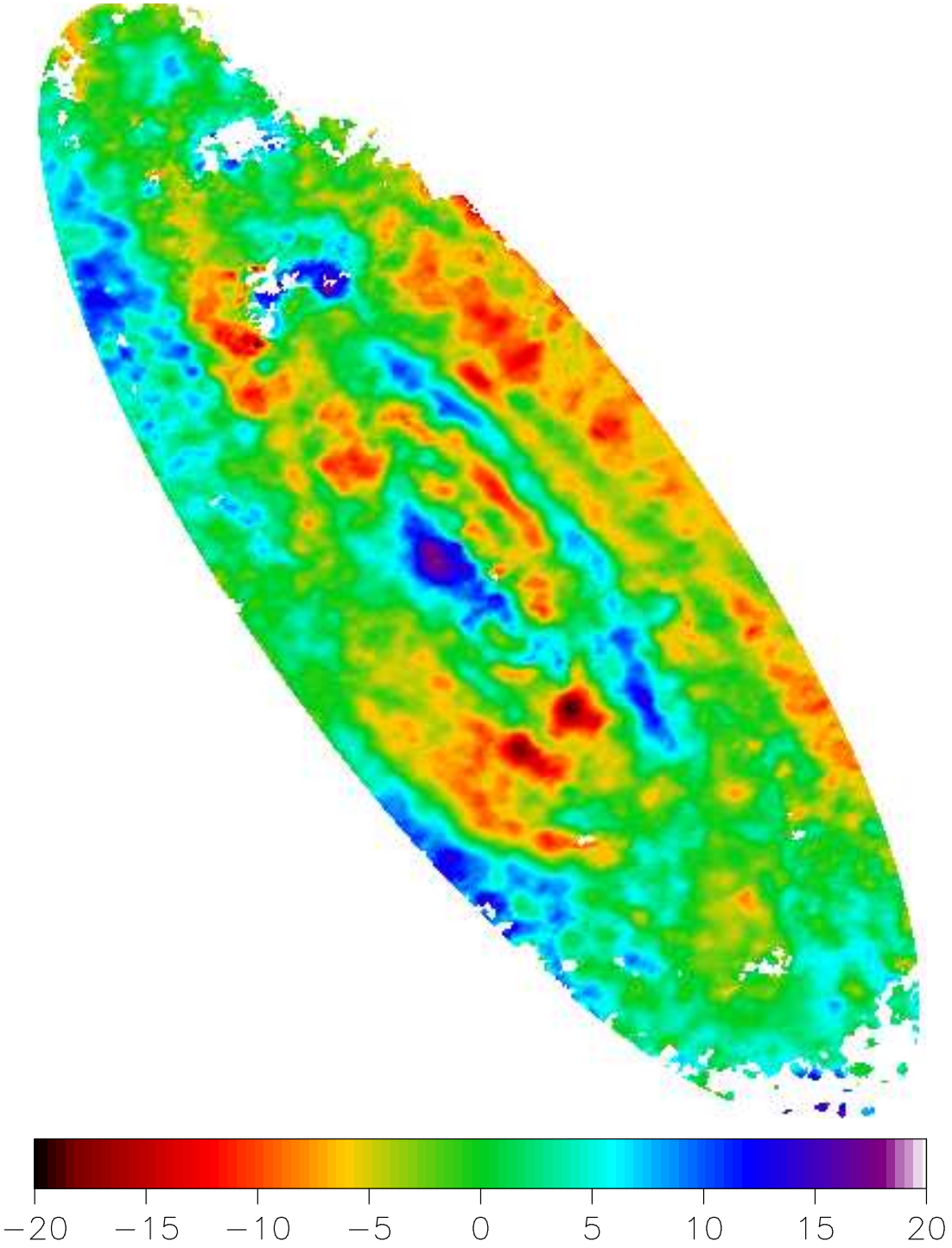

Figure 2.8 Residuals after fitting an axisymmetric model to the THINGS data for NGC 3198. The outer ellipse has a semi-major axis of $r = 456''$ and velocities in the color bar are in km s^{-1}.

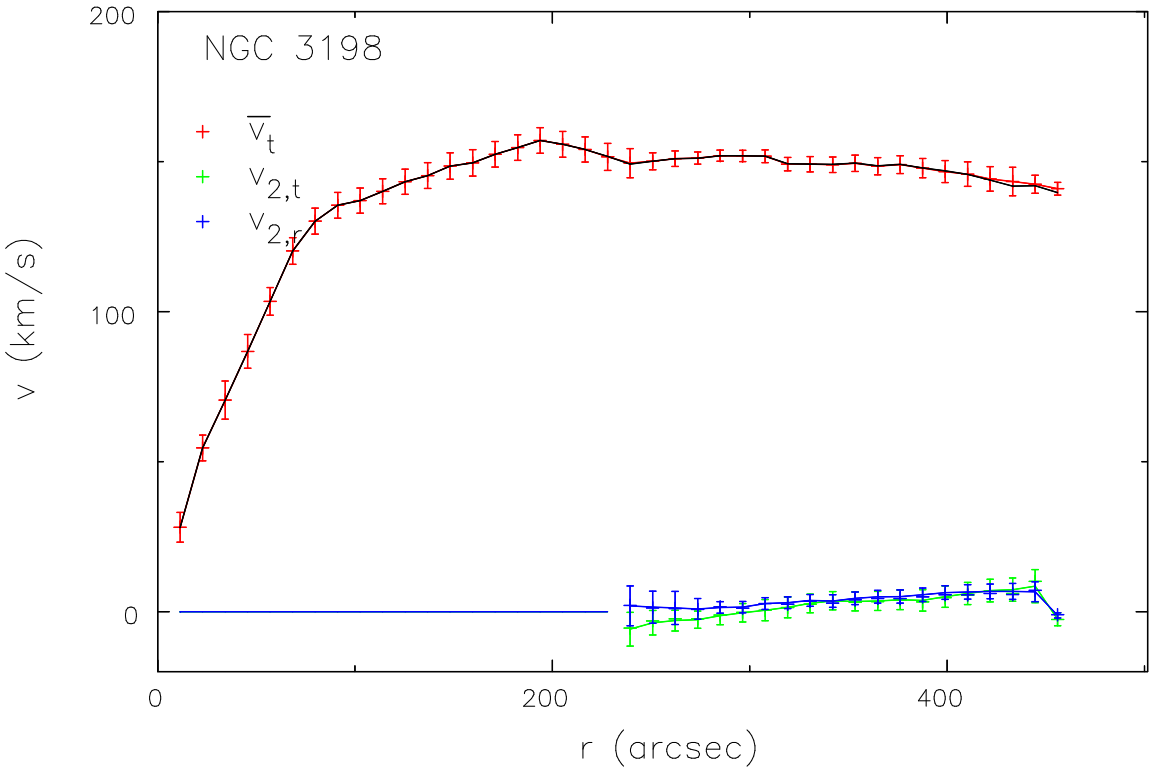

Figure 2.9 Results from *velfit* using THINGS data for NGC 3198. The black line shows the result of an axisymmetric fit to all radii, while the colored points show $\bar{V}_t(R)$ (red), $V_{2,t}(R)$ (green), & $V_{2,r}(R)$ (blue) from a bisymmetric fit restricted to the range $240'' \leq R \leq 460''$ with an axisymmetric model fitted to other radii.

Fig. 2.9 shows that the best fit non-axisymmetric velocities are no larger than $\sim 6\%$ of the circular speed and vary slowly with radius. If the perturbed velocities are caused by a slowly-rotating, mild oval distortion of the halo in the outer parts where the rotation curve is approximately flat, we should observe $V_{2,t} \simeq 1.5 V_{2,r}$ (see §2.2). In fact, the coefficients are not in this predicted ratio at any radius and even the signs differ over the inner part of the fitted range suggesting a different origin for the perturbed velocities, such as spiral arm streaming for which a fixed axis and slow rotation for the perturbation are inappropriate assumptions. Our fitted values of ϕ_b, $V_{2,t}(R)$, and $V_{2,r}(R)$ are merely those that achieve the largest reduction in χ^2 from the residual pattern shown in Fig. 2.8. In particular, the PA of the fitted "bar" varies with radius as we sub-divide the fitted region, as one would expect if the fit is picking up different fragments of the spirals.

Thus we are unable to identify a velocity pattern indicative of a non-axisymmetric halo. Whatever possible halo distortion may be present, it is clearly still weaker than the mild spiral features we do detect. We therefore concur with TBWBK that the data from NGC 3198 are consistent with this galaxy living in a perfectly round halo.

Even though we do not have a firm detection of a bar-like distortion in the halo, we can use the results in Fig. 2.9 to place a lower bound on its shape. We assume that velocities due to a halo distortion do not dominate the maximum disturbed velocities, which appear to be due to spiral arm streaming. So as a conservative bound, we use a straight average of both $|V_{2,t}|$ and $|V_{2,r}|$, or 3.5 km s^{-1}, as the disturbed velocity in the formula (2.9) and set $\bar{V}_t = 140$ km s^{-1}. Using these values, we obtain $q_\Phi \gtrsim 0.975$, and $q_\rho \gtrsim 0.92$ as our estimated lower limit on the axis ratio of the halo in NGC 3198.

NGC 2403

Fig. 2.10 shows that a simple, flat, axisymmetric model is a good fit to the THINGS data for NGC 2403, consistent with the tiny variations in i & PA reported by (de Blok *et al.* 2008). The small residuals are somewhat less indicative of spiral streaming than in

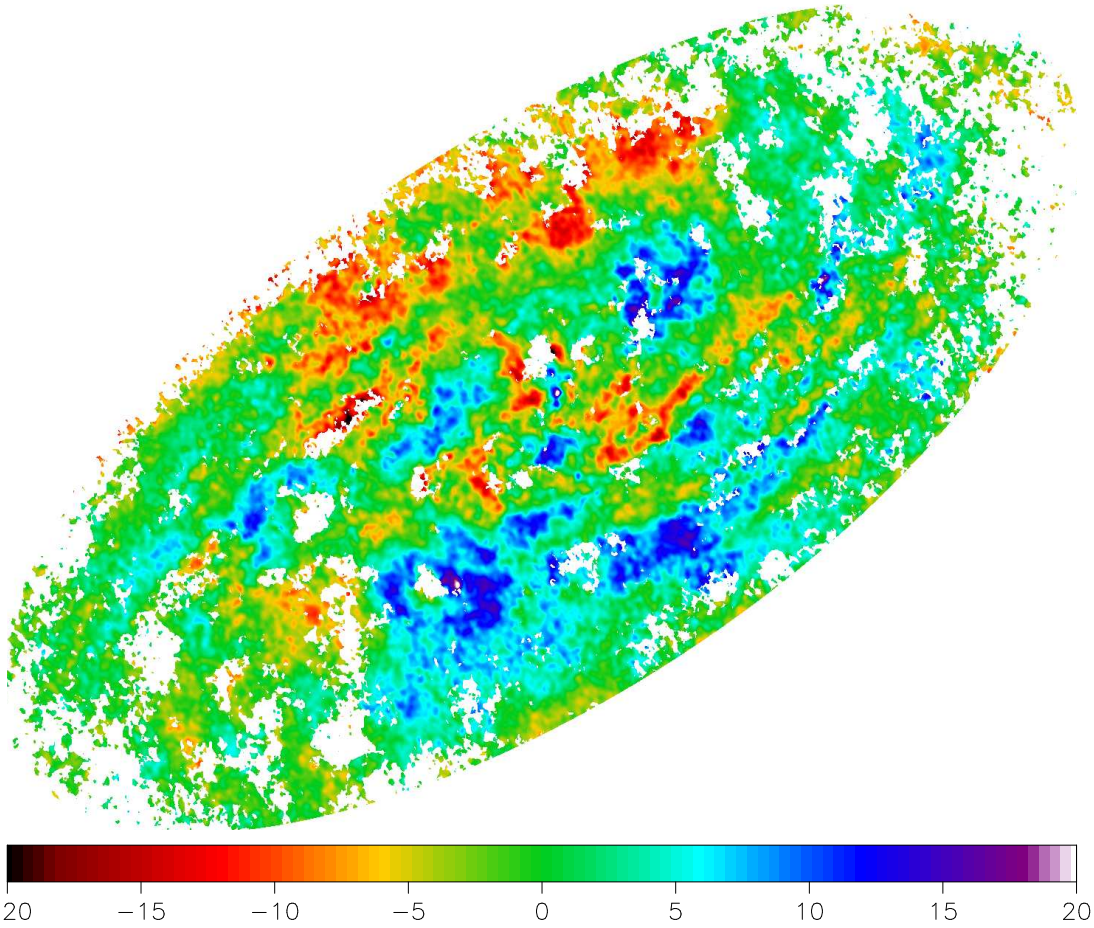

Figure 2.10 Residuals after fitting an axisymmetric model to the THINGS data for NGC 2403. The outer ellipse has a semi-major axis of $r = 844''$ and velocities in the color bar are in km s^{-1}.

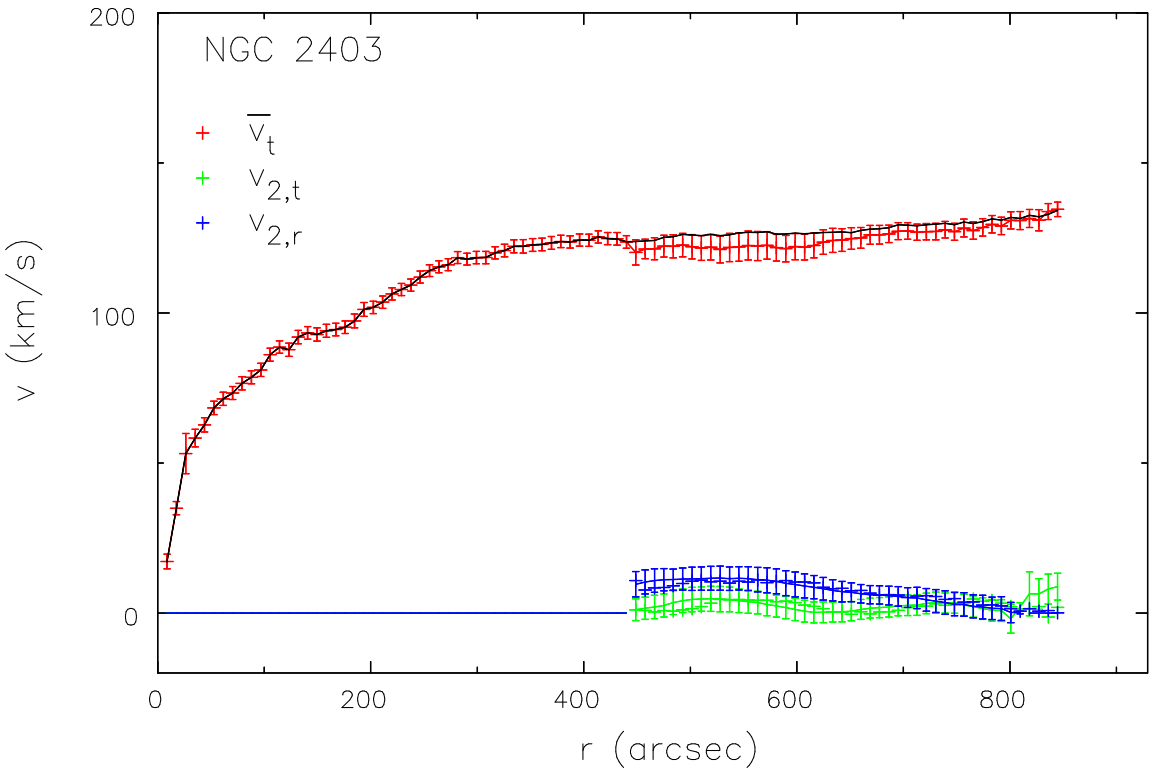

Figure 2.11 Same as for Fig. 2.9 but for NGC 2403.

NGC 3198, and show hints of a more global N-S anti-symmetry at larger projected radii ($R_{25} \simeq 656''$ in the B-band de Vaucouleurs *et al.* 1991).

Our fitted values of $V_{\rm sys}$, i & PA from a model that includes bisymmetric streaming velocities for $R > 450''$, listed in Table 2.3, are in excellent agreement with those found by de Blok *et al.* (2008). Fig. 2.11 shows that the perturbed velocities are $\lesssim 10$ km/s, but the radial component is generally the larger, which is inconsistent with a non-rotating, bar-like distortion. Thus we again concur with TBWBK that the THINGS data on this galaxy are consistent with it living in a perfectly round halo.

While the perturbed velocities are not of the form expected for a halo distortion, we proceed as for NGC 3198 and use the average of the absolute values of these fitted velocity components, 4.5 km s^{-1}, as an upper bound on the non-circular motions caused by a possible oval distortion of the halo. Since $\bar{V}_t \simeq 120$ km s^{-1}, we find $q_\Phi \gtrsim 0.96$, and $q_\rho \gtrsim 0.89$.

2.4 Conclusions

In this chapter, we have shown that the bisymmetric model (Spekkens & Sellwood 2007), embodied in the software *velfit*, is a powerful tool for quantifying non-circular streaming flows in galaxies. We argue in section 2.1 that it is altogether superior to the commonly used *reswri* (Schoenmakers *et al.* 1997). This is because it can fit strong distortions, it is more sensitive to radially coherent disturbances, it readily allows radial smoothing of the fitted velocities, and the estimated disturbed velocities are more easily related to the potential distortion. We also argue that while *velfit* assumes a flat plane for the inclined disc, this is not a weakness since tilts of individual rings, as *reswri* allows, are dangerous and can lead to severe underestimation of the distorted velocities. We illustrate these advantages for a number of galaxies.

We show that the THINGS data for NGC 2976 can indeed be fitted by an inner bar-like distortion, albeit somewhat milder than that found by SS07 from other data having higher spatial resolution. We argue that a bar flow is more natural than either the radial flow fitted by Simon *et al.* (2003) or the twisted disk model of Trachternach *et al.* (2008). We also illustrate that *velfit* yields a revised estimate of the mean orbital speed of the gas that differs from the simple mean fitted by tools such as *reswri*. The difference, which arises from the bias to the velocity on the major axis, can be of either sign depending on the orientation of the bar to the major axis of projection.

We have also shown that neutral hydrogen observations are not well suited to tracing gas dynamics in strongly barred potentials. The neutral hydrogen generally has a low column density in the barred region, and the velocity maps are generally too noisy or sparsely sampled to yield a clear indication of bar flow. Smoothing to lower spatial resolution improves signal-to-noise, and yielded an almost fully sampled velocity map throughout the bar region of NGC 2903, which enabled us to identify an oval flow pattern of about the right physical size and with signifiant streaming velocities, but the large uncertainties imply

they are also consistent with zero. However, a strong bar flow is unambiguously detected in data of higher spatial resolution, which we show by fitting to the Hα velocity map of Hernandez *et al.* (2005).

Our analysis of the THINGS data for NGC 3198 & NGC 2403 reaches a similar conclusion to that of TBWBK: that the halos of these two galaxies are very close to round. Jog (2000) and Bailin *et al.* (2007) show that the self-consistent response of the disc can mask a large part of the distortion in the halo, but only when the disc is massive. In these two cases, the outer gas disc has very little mass and therefore could not hide a more substantial halo distortion.

However, it is hard to confront this result with the predictions of LCDM (cited in the introduction): not only is it based on just two galaxies, but it is possible these two galaxies are unrepresentative perhaps because only galaxies with unusually round halos could host an extensive disc of gas that is not warped! Clearly, measurements of halo shapes in a representative galaxy sample will require a tool that can reliably measure potential distortions in warped discs. Other statistical approaches (Franx & de Zeeuw 1992; Trachternach *et al.* 2009) do, however, place some reasonably tight constraints on halo shapes.

Thus, while we confirm the conclusion of Trachternach *et al.* (2008) that many galaxies in the THINGS sample have at most minor departures from axial symmetry, *velfit* reveals that mild bars are present in NGC 2976 and NGC 7793. We also show that their conclusion for strongly barred galaxy NGC 2903 was a consequence of beam smearing, and other data show that this galaxy does indeed have a pronounced non-axisymmetric flow in the bar region.

Another valuable application for *velfit* will be a preliminary analysis of the velocity maps of strongly barred galaxies. It would be very helpful obtain a clear indication of whether the flow pattern is, or is not, well enough sampled and sufficiently regular to yield a result, before embarking on laborious mass modeling by the method described by Weiner *et al.*

(2001). Furthermore, such a study needs approximate axisymmetric mass models, and the estimates of $\bar{V}_t$ from *velfit* will be more useful than the "circular speed" estimated from other less powerful tools.

Bibliography

Allgood, B., Flores, R. A., Primack, J. R., Kravtsov, A. V., Wechsler, R. H., Faltenbacher, A. & Bullock, J. S. 2006, MNRAS, **367**, 1781

Bailin, J., Simon, J. D., Bolatto, A. D., Gibson, B. K. & Power, C. 2007, ApJ, **667**, 191

Begeman, K. G. 1987, PhD. thesis, University of Groningen

Binney, J. & Tremaine, S. 2008, *Galactic Dynamics* 2nd edition (Princeton: Princeton University Press)

Bosma, A. 1978, PhD. thesis, University of Groningen

Briggs, F. H. 1990, ApJ, **352**, 15

Canzian, B. 1993, ApJ, 414, 487

Debattista, V. P., Moore, B., Quinn, T., Kazantzidis, S., Maas, R., Mayer, L., Read, J. & Stadel, J. 2008 ApJ, **681**, 1076

de Blok, W. J. G., Walter, F., Brinks, E., Trachternach, C., Oh, S-H. & Kennicutt, R. C. 2008, AJ, **136**, 2648

de Vaucouleurs, G., de Vaucouleurs, A., Corwin, H. G., Jr., Buta, R. J., Paturel, G., & Fouqué, P. 1991, Third Reference Catalogue of Bright Galaxies (New York: Springer)

Dubinski, J. 1994, ApJ, **431**, 617

Franx, M. & de Zeeuw, T. 1992, ApJL, **392**, L47

Franx, M., van Gorkom, J. H. & de Zeeuw, T. 1994, ApJ, **436**, 642

Hayashi, E. & Navarro, J. F. 2006, MNRAS, **373**, 1117

Hayashi, E., Navarro, J. F. & Springel, V. 2007, MNRAS, **377**, 50

Helfer, T. T., Thornley, M. D., Regan, M. W., Wong, T., Sheth, K., Vogel, S. N., Blitz, L. & Bock, D. C.-J. 2003, ApJS, **145**, 259

Hernandez, O., Carignan, C., Amram, P., Chemin, L. & Daigle, O., 2005, MNRAS, **360**, 1201

Jing, Y. P. & Suto, Y. 2002, ApJ, **574**, 538

Jog, C. J. 2000, ApJ, **542**, 216

Kranz, T., Slyz, A. D. & Rix, H.-W. 2003, ApJ, **586**, 143

Oh, S-H., de Blok, W. J. G., Walter, F., Brinks, E. & Kennicutt, R. C. 2008, AJ, **136**, 2761

Pence, W. D. & Blackman, C. P. 1984, MNRAS, **210**, 547

Schoenmakers, R. 1999, PhD. thesis, University of Groningen

Schoenmakers, R. H. M., Franx, M. & de Zeeuw, P. T. 1997, MNRAS, **292**, 349

Sellwood, J. A. & Wilkinson, A. 1993, Rep. Prog. Phys., **56**, 173

Shen, J. & Sellwood, J. A. 2006, MNRAS, **370**, 2

Simon, J. D., Bolatto, A. D., Leroy, A. & Blitz, L. 2003, ApJ, **596**, 957

Skrutskie, M. F. *et al.* 2006, AJ, **131**, 1163

Sofue, Y. & Rubin, V. 2001, ARAA, **39**, 137

Spekkens, K. & Sellwood, J. A. 2007, ApJ, **664**, 204 (SS07)

Trachternach, C., de Blok, W. J. G., Walter, F., Brinks, E. & Kennicutt, R. C. 2008, AJ, **136**, 2720

Trachternach, C., de Blok, W. J. G., McGaugh, S. S., van der Hulst, J. M. & Dettmar, R.-J. 2009, arXiv:0907.5533

Valenzuela, O., Rhee, G., Klypin, A., Governato, F., Stinson, G., Quinn, T. & Wadsley, J. 2007, ApJ, **657**, 773

van den Bosch, F. C. & Swaters, R. A. 2001, MNRAS, **325**, 1017

van Eymeren, J., Trachternach, C., Koribalski, B. S. & Dettmar, R. J. 2009, arXiv: 0906.4654

Walter, F., Brinks, E., de Blok, W. J. G., Bigiel, F., Kennicutt, R. C., Thornley, M.D. & Leroy, A. K. 2008, AJ, **136**, 2563

Weiner, B. J., Sellwood, J. A. & Williams, T. B. 2001, ApJ, **546**, 931

Zánmar Sánchez, R., Sellwood, J. A., Weiner B. J. & Williams, T. B. 2008, ApJ, **674**, 797

Chapter 3

Modeling the Gas Flow in the Bar of NGC 1365

The material in this chapter also appears in print as "Modeling the Gas Flow in the Bar of NGC 1365", Zánmar Sánchez *et al.* 2008, ApJ, 674, 797.

3.1 Introduction

The centrifugal balance of the circular flow pattern in a near-axisymmetric spiral galaxy yields a direct estimate of the central gravitational attraction as a function of radius. However, the division of the mass giving rise to that central attraction into separate dark and luminous parts continues to prove challenging. The radial variation of the circular speed simply does not contain enough information to allow a unique decomposition between the baryonic mass, which has an uncertain mass-to-light ratio, Υ, and the dark halo, whose density profile is generally described by some adopted parametric function (van Albada *et al.* 1985; Lake & Feinswog 1989; Barnes, Sellwood & Kosowsky 2004).

Predictions for Υ from stellar population synthesis models that match broad-band colors (e.g. Bell *et al.* 2003) are useful, but not precise. Despite intense effort, they are still sufficiently uncertain to be consistent with both maximum and half-maximum disk, which is the range of disagreement (e.g. Sackett 1997; Bottema 1997; Sellwood 1999). McGaugh (2005) argues that the values can be refined by minimizing the scatter in the Tully-Fisher and/or mass discrepancy-acceleration relation.

A number of dynamical methods have been employed to break the disk-halo degeneracy. Casertano (1983), Bosma (1998), and others have suggested that the slight decrease in

orbital speed near the edge of the optical disk of a bright galaxy – the "truncation signature" – could be used as an indicator of disk Υ, but in practice it does not provide a tight constraint. Athanassoula, Bosma & Papaioannou (1987) and Fuchs (2003) attempt to constrain the disk mass using spiral structure theory. Bottema (1997) and Verheijen *et al.* (2004) measure the vertical velocity dispersion of disk stars in a near face-on galaxy, which they assume has the same mean thickness of similar galaxies seen edge-on (Kregel, van der Kruit & de Grijs 2002), to constrain the disk mass. A similar approach is reported by Ciardullo *et al.* (2004) using velocity measurements of individual planetary nebulae.

One of the most powerful, although laborious, methods for barred galaxies was pioneered by Weiner, Sellwood & Williams (2001), who made use of the additional information in the driven non-circular motions caused by the bar. By modeling the observed non-axisymmetric flow pattern of the gas in a 2-D velocity map, they were able to determine the mass-to-light ratio of the visible disk material. They found that the luminous disk and bar contributed almost all the central attraction in NGC 4123 inside ~ 10 kpc, requiring the dark halo to have a very low central density. Weiner (2004) reports a similar result for a second case, NGC 3095. The method has also been applied by Pérez *et al.* (2004) for several barred galaxies and by Kranz *et al.* (2003) who modeled motions caused by spiral arms. Bissantz, Englmaier & Gerhard (2003) present a similar study for the Milky Way. Earlier studies (*e.g.* Duval & Athanassoula 1983) did not attempt to separate the disk from the dark matter halo (see Sellwood & Wilkinson 1993, for a review). Here, we apply the (Weiner *et al.* 2001) method to the more luminous barred galaxy NGC 1365 in the Fornax cluster.

As one of the most apparently regular, nearby barred spiral galaxies in the Southern sky, NGC 1365 was selected by the Stockholm group for an in-depth study (see *e.g.* Lindblad 1999). Hydrodynamic models of the bar flow pattern were already presented by (Lindblad, Lindblad & Athanassoula 1996), based mainly on the velocities of emission-line measurements from many separate long-slit observations. Jörsäter & van Moorsel (1995, hereafter JvM95) present a kinematic study using the 21 cm line, which suggests that the galaxy

is somewhat asymmetric in the outer parts, where the shape of the rotation curve is hard to determine. Sandqvist *et al.* (1995) find substantial amounts of molecular gas, but only within 2 kpc of the nucleus, which is resolved in interferometric observations (Sakamoto *et al.* 2007) into a molecular ring in the center plus a number of CO hot spots. Galliano *et al.* (2005) have found previously unknown MIR sources in the inner 10″ around the AGN. They are able to correlate some of these MIR sources with radio sources, which they interpret in terms of embedded star clusters because of the lack of strong optical counterparts. Jungwiert, Combes & Axon (1997) present H-band photometry of the bright inner disk, finding an elongated component in the central region suggesting that NGC 1365 is a double-barred galaxy, although they note that the light in this component is not as smooth as in their other nuclear bar cases. Laine *et al.* (2002) also classify it as a double barred galaxy. However, Emsellem *et al.* (2001) and Erwin (2004) argue against a nuclear bar, citing an HST NICMOS image which resolves the feature into a nuclear spiral. Emsellem *et al.* (2001) also present stellar kinematics from slit spectra using the ^{12}CO bandhead. They propose a model for the inner 2.5 kpc of NGC 1365 consisting of a decoupled nuclear disk surrounded by spiral arms within the inner Lindblad resonance (ILR) of the primary bar. Beck *et al.* (2005) observed NGC 1365 in radio continuum at 9″-25″ resolution and find radio ridges roughly overlapping with the dust lanes in the bar region. They propose that magnetic forces can control the flow of gas at kiloparsec scales.

Here we present new photometric images, a full 2-D velocity map of the Hα emission, and a reanalysis of the neutral hydrogen data from JvM95. We also compare many hydrodynamic models to these new data in an effort to determine the separate disk and dark halo masses in this galaxy.

3.2 Observations

The Weiner *et al.* (2001) method requires both broad band photometry, to estimate the distribution of visible matter, and a high spatial resolution velocity map to determine

the projected non-axisymmetric flow pattern in the barred region. While not absolutely essential, knowledge of the rotation curve at larger radii is helpful to estimate the total central attraction. Velocity maps using the 21cm line of neutral hydrogen have lower spatial resolution but extend to larger radii, and are therefore an ideal complement to the optical data.

Here we adopt the distance to NGC 1365 of 18.6 Mpc, as deduced from Cepheid variables by Madore *et al.* (1999). At this distance, $1''$ corresponds to 90.2 pc.

3.2.1 Surface Photometry

Observations of NGC 1365 were made on the night of 1999 Jan 24 with the Swope 1 m telescope at Las Campanas Observatory. The LCO Tek#5 2048×2048 pixel CCD was used with a pixel scale of $0.''70$ and a field of view of $24'$. We obtained 3×10 minute offset exposures in each of the V & I filters. The seeing was approximately $1.''6$. We reduced the images with IRAF[1] with the standard procedure: subtraction of overscan, bias, and flat-fielding with twilight flats. The LCO CCD detector exhibits fringing and illumination gradients in the I filter. These were removed by constructing a supersky image by combining all the available I-band images taken throughout the night and subtracted from NGC 1365 I-band image. Photometric standard stars from Landolt (1992) were observed at several times during the night and used to derive extinction coefficients.

The resulting calibrated I-band image is presented in the upper panel of Figure 3.1. We have drawn a single isophotal contour and redrawn the same contour rotated through 180° in order to show the symmetry of the bar light distribution. This particular isophote shows the approximate size of the bar, as determined below. We see that the east side of the bar is marginally fatter, at this isophote level, than is the west, but the shape of the bar is remarkably symmetric. In subsequent figures we draw, as a reference, a slightly smoothed

[1]IRAF is distributed by NOAO, which is operated by AURA, Inc., under a cooperative agreement with the National Science Foundation.

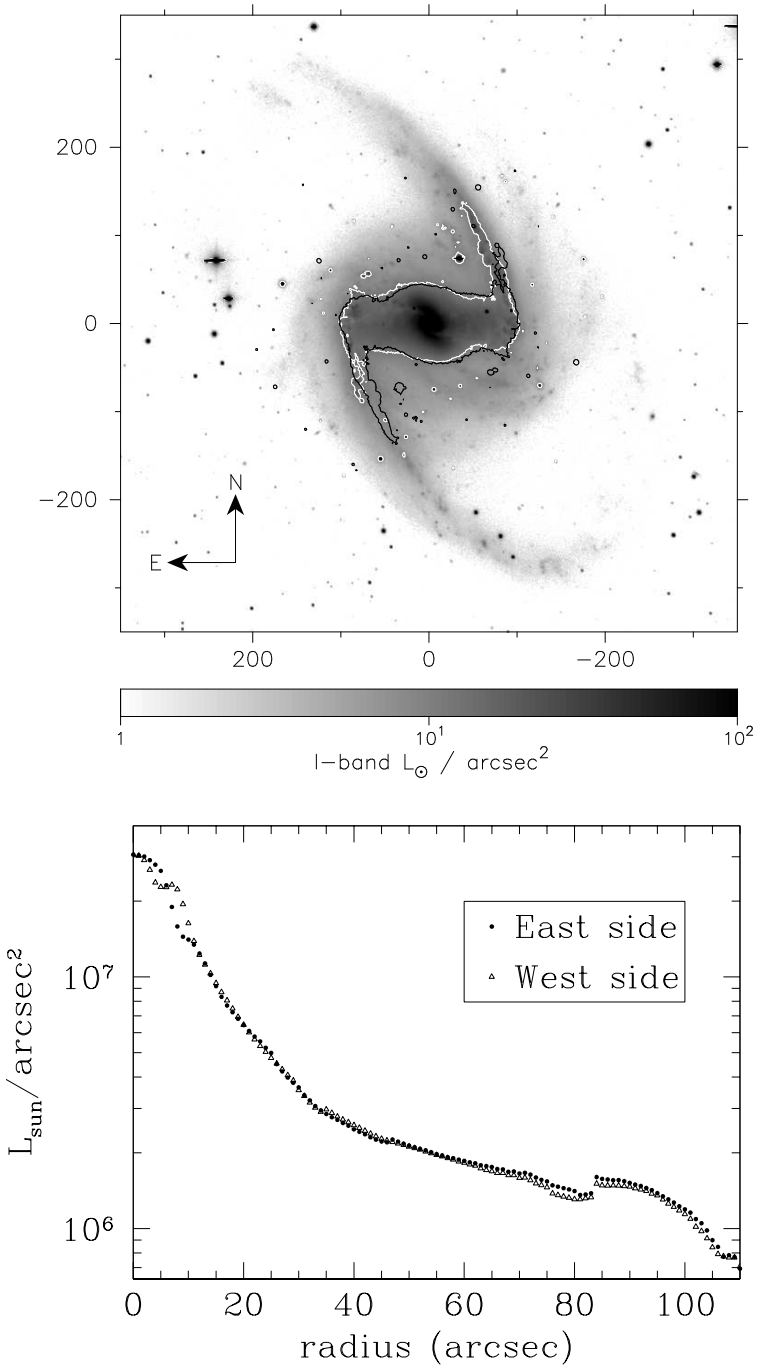

Figure 3.1 *Upper:* A 700″ square region with the I-Band image of NGC 1365 showing intensity on a log scale. The intensity range does not represent the full range and has been chosen to reveal the spiral and bar structures most clearly (*i.e.* the center of the galaxy has a luminosity of $\sim 3\times\ 10^7 L_\odot/arcsec^2$). A white contour with intensity $1.2\times\ 10^6 L_\odot/arcsec^2$ has been plotted to outline the bar. The black contour is the same as the white but rotated by 180°; the similarity of the two contours shows the remarkable 2-fold symmetry of the bar. Subsequent figures show this isophote for reference drawn from a 2-fold rotationally averaged image. *Lower:* Surface brightness profiles for the east and west sides of the bar estimated independently. The length of the semimajor axis of the bar is 100″.

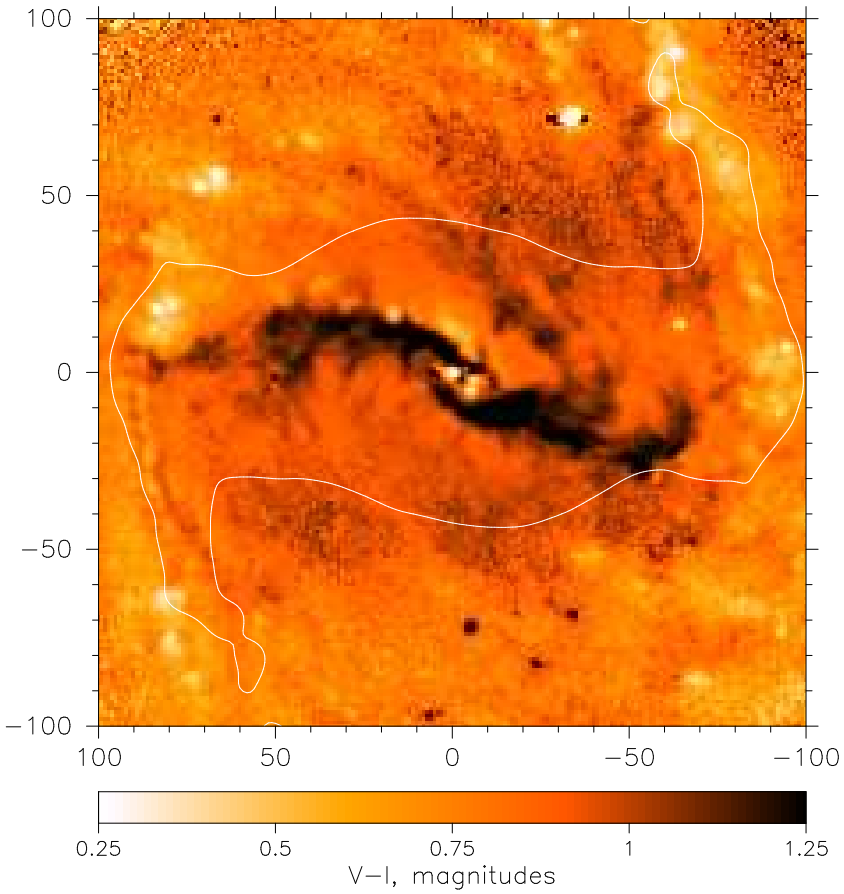

Figure 3.2 V-I color map of the central 200″ square region of NGC 1365. Dust lanes are clearly visible on the leading sides of the bar. The isophote from Fig. 3.1 is included for reference. Note the absence of symmetry in the dust lanes; that on the west side lies farther from the bar major-axis.

version of this isophote from the 2-fold rotationally averaged I-band light distribution.

The lower panel in Figure 3.1 presents independent estimates of the surface brightness profile for the left and right side of the bar, constructed as follows. We ran the IRAF-ellipse tool on a version of the I-band image smoothed to 3″, to find a set of isophotal ellipses with position angle and ellipticity as free parameters, but with a fixed center. We then used the same generated ellipses on the original I-band image to find the mean intensity for the east and west sides independently. This analysis reveals that the light distribution is indeed highly symmetric. The apparent discontinuity in the light profiles at $r \sim 85''$ is due to variations in the fitted ellipticity caused by a number of bright HII regions near the end of bar.

The strong dust lanes in the bar, and other places, are easily visible in the V-I color map of NGC 1365 (Figure 3.2). As usual, the dust lanes are on the leading side of the bar (which rotates clockwise if the spiral arms are assumed to trail). Despite the evident 2-fold symmetry of the bar, the dust lanes are clearly not symmetric; the strongest dust features on the west side lie farther towards the leading edge of the bar than those on the east. This asymmetric extinction could be the cause of the mild asymmetry in the bar light (Fig. 3.1) noted above.

Since the NE side of the galaxy is approaching while the SW receding, trailing spiral arms imply that the NW of the galaxy is tipped towards us. Assuming the redder regions in the color map indicate diffuse dust, there appears to be more extinction on the near (NW) side than on the far (SE) side, which is consistent with expectations for a moderately inclined disk (*e.g.* Binney & Merrifield 1998, §4.4.1). Holwerda *et al.* (2005) present a detailed study of dust extinction in part of NGC 1365.

We deproject the galaxy to obtain a face-on surface brightness profile, adopting the projection geometry indicated by the kinematic maps presented in §3.4: position angle (hereafter PA) = 220° and inclination $i = 41°$. We estimate $R_{23.5} = 348'' \simeq 31.4$ kpc in the I-band, which is comparable to B magnitude $R_{25} = 337''$ (de Vaucouleurs *et al.* 1991), and an exponential scale length for the disk of $r_d \simeq 6.5$ kpc. We estimate the total magnitude within $R_{23.5}$ to be 8.2 in I and 9.4 in V, without any extinction corrections. For our modeling of the potential from the I band, we apply an internal extinction correction $A_{\rm int} = -1.0 \log(b/a)$ from Giovanelli *et al.* (1994) and a galactic extinction from Schlegel, Finkbiner & Davis (1998) for a total correction of -0.16 at I.

We estimated the size of the bar by fitting ellipses to the deprojected I-band image at a number of isophote levels. Ideally, one hopes for an abrupt change in the ellipticity and PA of the radial profiles at the transition between the bar and the disk. The spiral arms, however, force the PA to vary continuously and broaden the ellipticity peak somewhat (Wozniak *et al.* 1995). We estimate the deprojected bar semi-major axis to be $114'' \lesssim r_B \lesssim$

$127''$, where the lower limit is the radius of maximum ellipticity, 0.63, and the upper limit is the radius at which the PA begins to change sharply. This range is in agreement with the value of $r_B = 120'' \pm 10''$ estimated by Lindblad, Lindblad & Athanassoula (1996) using Fourier moment decomposition, and hereafter we adopt their value $r_B = 120'' = 10.8$ kpc as the bar semi-major axis. While physically large, $r_B \simeq 1.66 r_d$, which is typical (Erwin 2005).

In this work, we use our I-band image as a measure of the light from the old disk stars. Although far less problematic than in the V-band, some residual dust obscuration slightly attenuates the I-band light. As the opacity of dust is still lower in infrared light, it might be argued that a better estimate of the underlying stellar light distribution could be obtained from J, H, or K-band images. However, the NIR bands are not a panacea as the light in these bands is more seriously affected by AGB stars and hot dust in HII regions, as may be seen by the lumpiness of the 2MASS (Strutskie *et al.* 1997) K-band image. In addition, no available NIR detector is large enough to cover this galaxy well out to the sky without mosaicking, and no existing near infrared image is deep enough (*e.g.* 2MASS) to yield the accurate measure of the outer disk surface brightness profile we require. Furthermore, de Jong (1996) shows that the dependence of the I-band surface brightness on age and star formation history is only slightly stronger than for the K-band. We therefore adopt our I-band image as the best available estimator of the underlying disk light down to very low surface brightness levels.

3.2.2 Fabry-Perot Imaging Spectroscopy

NGC 1365 was observed in the Hα line on the nights of 1993 November 3-4 with the CTIO[2] 1.5m telescope using the Rutgers Imaging Fabry-Perot interferometer. A Tektronix 1024×1024 CCD detector was used with $0.''98$ pixels. The field of view of the etalon was $7.'8$ in diameter. Hourly calibrations were taken in order to correct for temporal drifting

[2]CTIO is operated by AURA under contract to the NSF.

of the wavelength zero point and optical axis center.

The first night of the observations was photometric but the second night was plagued with intermittent cloud, and three exposures had to be discarded. The remaining NGC 1365 observations consist of 16 separate 10-minute exposures spanning 17.4 Å in steps of ∼1.2 Å (54 km s^{-1}) and covering a range of velocities from 1010 to 2031 km/s. The reduction methods are similar to those described elsewhere (Palunas & Williams 2000; Weiner *et al.* 2001). The images were reduced with IRAF: overscan subtraction, bias, and flat fielding. After the removal of cosmic rays, the images were spatially registered and sky subtracted to build the data cube. The typical seeing as measured from foreground stars was around 2.4″. Sky transparency variations occurred throughout the observation and are a major source of uncertainties in line profiles (Williams *et al.* 1984). We measure the flux of the brightest, isolated foreground star in the field of view and scale the frames to a common transparency. Corrections never exceed 3%.

Four frames of our cube seem to be mildly contaminated by sky lines $\lambda = 6604.13$ and $\lambda = 6596.64$ Å produced by air OH rotation-vibration transitions (Osterbrock & Martel 1992). A model of the sky ring can be easily constructed because the spectral width of sky lines is very narrow and we should recover only the unresolved instrumental Voigt profile. Nevertheless, the peak intensity of the sky ring is hard to determine because of the confusion with the light of the embedded galaxy. We tried a range of peak intensity values and convinced ourselves that it is no more that 4-5 counts above the background level. Subtraction of these sky rings eliminated spurious fits in the faint outskirts of the galaxy and had no noticeable effect on the velocity fits within the galaxy.

The Fabry-Perot has a spectral resolution of 2.5 Å at Hα or FWHM $\simeq$ 150 km s^{-1}. The spectral profile was approximated with a Voigt function with Gaussian $\sigma_G = 21.6$ km s^{-1} and Lorentzian $\sigma_L = 61.4$ km s^{-1}. In order to improve the S/N of our line profiles, we combined data from adjacent pixels using a varying Gaussian kernel of up to 5×5 pixels for which the FWHM is adapted depending on the strength of the line. We use only the

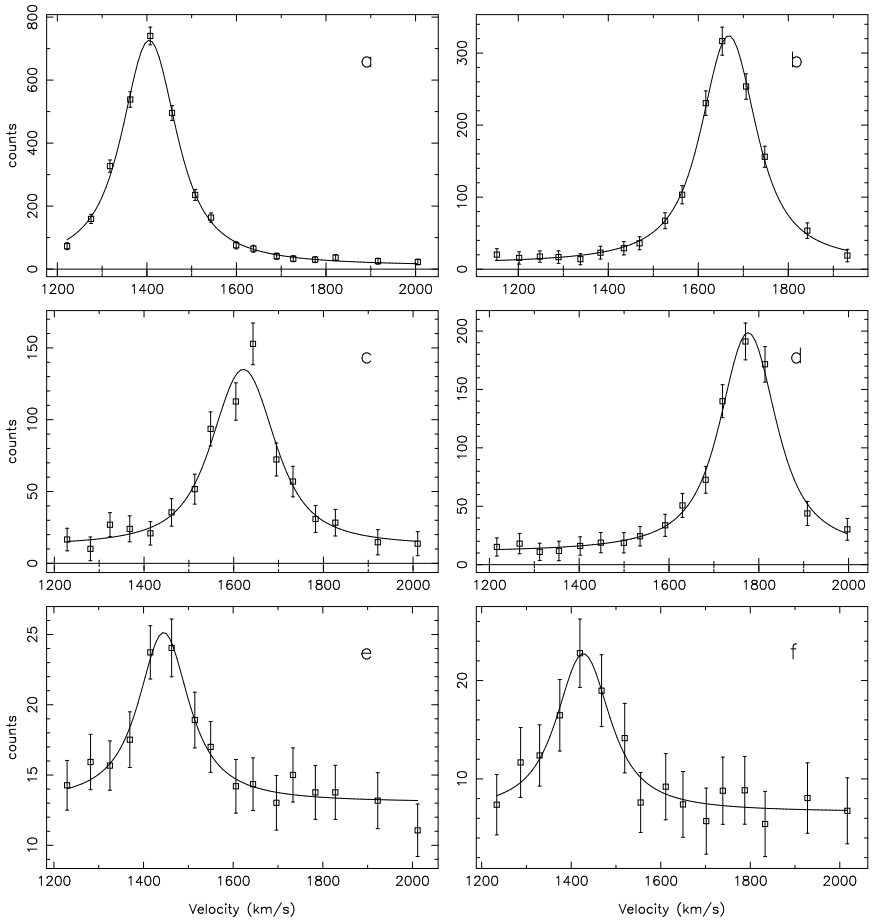

Figure 3.3 Example line profiles. *a.)* and *b.)* Bright HII region on spiral arm. *c.)* and *d.)* Bright HII regions from east and west side of the bar respectively; *c.)* is from the region labeled R2 in Fig. 3.5. *e.)* and *f.)* Diffuse emission from east side of the bar.

central pixel when the line is very strong, but bin pixels 3×3 (FWHM=1.6″) for lines of intermediate strength, and use a 5×5 box (FWHM=3.3″) for very weak emission.

Fabry-Perot images are not strictly monochromatic because of the angular dispersion of the instrument. For every pixel, the wavelength is calculated from a quadratic variation with the radial distance from the optical axis determined from calibration lamp exposures. With the fluxes and wavelengths for every pixel, a Voigt function of five parameters can be fitted with least-squares techniques. After some experimentation, we decided to fix the Lorentzian width to the instrumental value and fitted the four remaining parameters: center wavelength (velocity), Gaussian line width, peak intensity of the emission and the continuum level. Figure 3.3 shows a selection of resultant emission line profiles: (a) and

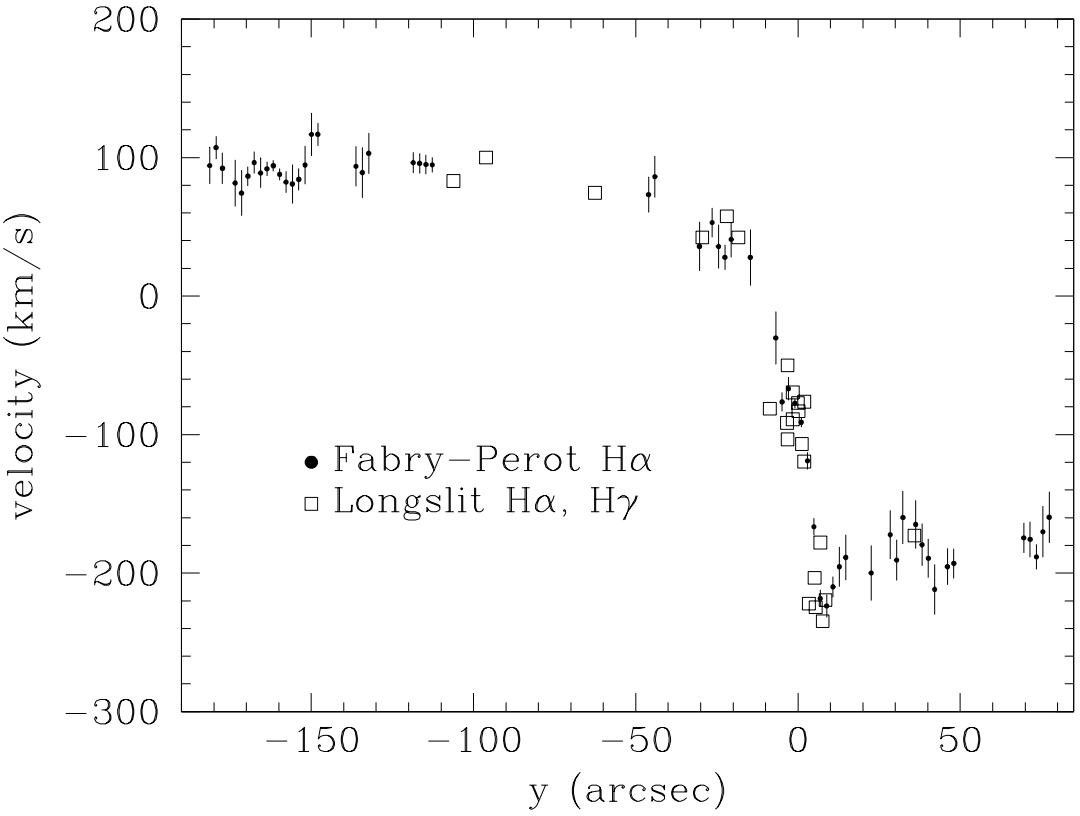

Figure 3.4 Comparison between line-of-sight velocities from Fabry-Perot data (filled points) and the long slit measurements (open symbols) from Lindblad *et al.* (1996). Data from their Fig. 2e are based on the Hα and Hγ lines from a slit positioned in the N-S direction and centered on the bright HII region L33.

(b) are of very bright HII regions in the spiral arms, (c) and (d) are of bright HII regions in the eastern and western side of the bar respectively, while (e) and (f) are of diffuse emission from the east side of the bar.

Fits to every pixel yield maps of velocity, line strength, line width, continuum level and the estimated uncertainty in each quantity. Figure 3.5 presents the velocity map; regions where the velocity uncertainty exceeds 20 km s^{-1} are left blank. We illustrate the velocities using 10 colors only so that the interface between two colors marks an isovelocity contour. The dotted outline is the reference isophote of the bar while the two straight solid lines in the outer regions lie along the estimated (see §3.4) minor axis of the galaxy and help to identify kinks in the velocity field inside the bar.

Figure 3.4 presents a comparison between our Fabry-Perot velocity measurements and the long slit measurements using Hα and Hγ from Lindblad *et al.* (1996), taken from their Fig 2.e. Their slit was centered on bright HII region L33 and runs along the South-North direction with the zero point of the velocity set to 1630 km/s. We also find very good agreement (within $1-\sigma$) between our measured velocities for other bright HII regions L2, L3, L4, L29, L32, as labeled by Alloin *et al.* (1981), and HII region containing supernova 1983V. Our estimates for the nucleus and L1 differ from theirs by $\sim$ 40 km/s, which is not surprising since NGC 1365 is a Seyfert galaxy and several authors (Phillips *et al.* 1983; Edmunds *et al.* 1988; Lindblad *et al.* 1996) have detected splitting of the high excitation line [OIII]. Double-valued velocities are thought to arise from a disk component and a bipolar hollow conical outflow, as first proposed by Phillips *et al.* (1983).

The velocity map reveals steep gradients in the bar region, especially on the leading edges, where the dust lanes are also found, as has been reported previously (Jörsäter *et al.* 1984; Lindblad *et al.* 1996; Teuben *et al.* 1986, and references therein). These steep gradients are strongly asymmetric as is clear in our velocity map. The velocity jumps on the west side of the bar extend farther to the leading side of the bar, consistent with the asymmetric arrangement of the dust lanes. The asymmetry can also be seen in Fig. 4 of Lindblad *et al.* (1996), although based on a rather sparse spatial coverage (interpolated map from 35 slits).

The line profile (Fig. 3.3c) of the bright HII region on the east side of the bar labeled R2 in Fig. 3.5 (offset from the nucleus $x = \Delta\alpha\cos\delta = 54.60''$, $y = \Delta\delta = 13.88''$), is not well fitted by a single broadened velocity, but seems to be more complex. Furthermore, the mean fitted velocity at this location differs substantially from that of the faint emission in the surrounding pixels (see inset of Fig. 3.5). Other bright HII regions on the east side of the bar (*e.g.* R1 at $x = 45.90''$, $y = 20.64''$ and R3 at $x = 55.33''$ $y = -0.84''$) show similar anomalies.

In order to quantify the velocity difference between these three bright regions and that

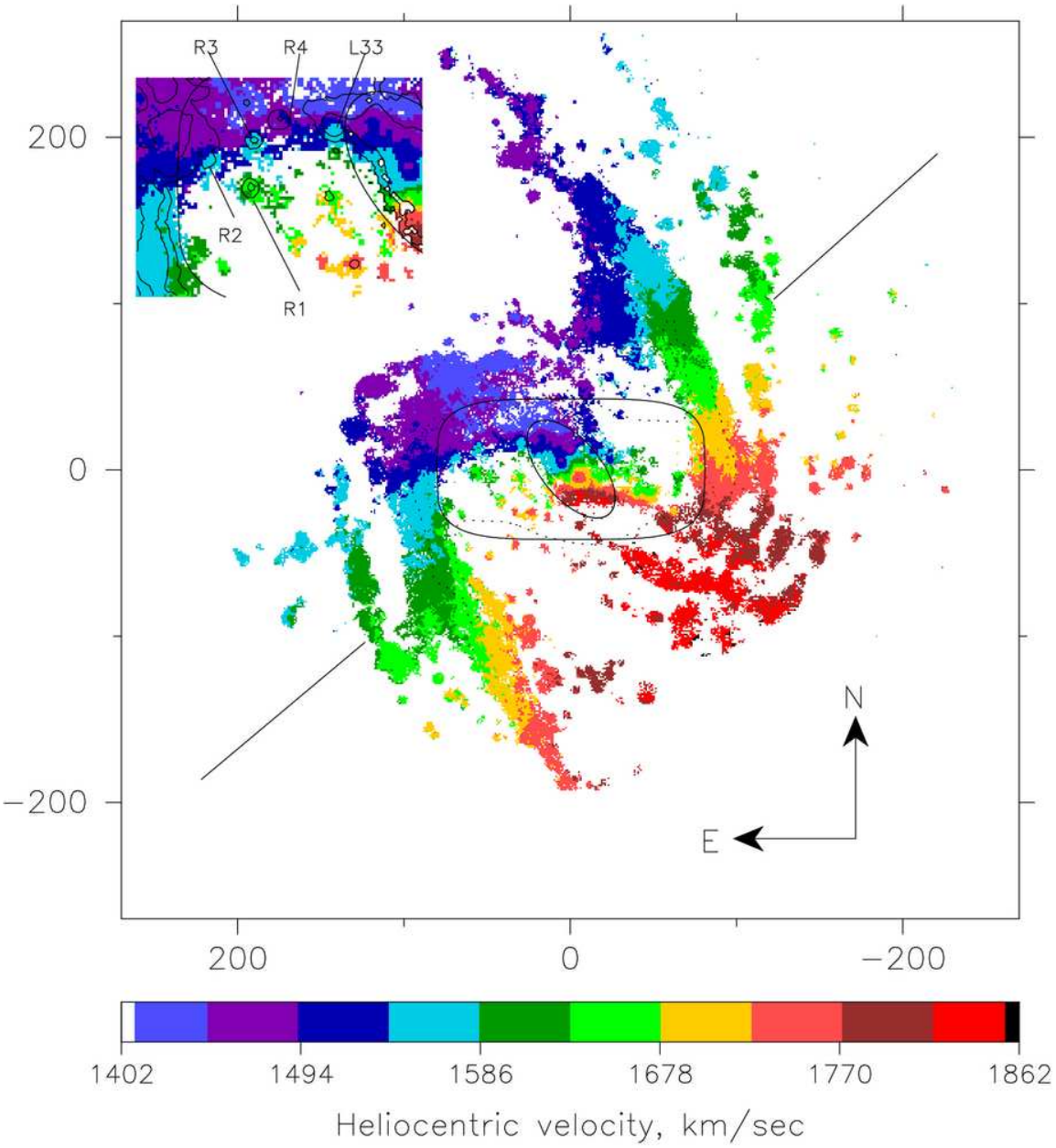

Figure 3.5 The velocity map of NGC 1365 from Fabry-Perot observations of the Hα emission line. The color map has been binned in 10 colors to outline velocity contours. The dotted line shows the contour from Fig. 3.1. The closed solid curves are described in §3.6.1. The upper-left inset shows an enlargement of the east side of the bar with contours of intensity to show the positions of several labeled bright HII regions.

of the surrounding diffuse gas, we fit a bi-linear velocity gradient to the diffuse emission over a small square patch (20×20 pixels) surrounding each bright region. The interpolated velocity at the center of the HII regions differs by between 60 & 80 km/s from the measured value. These complicated profiles may result from disturbance by infalling gas, as discussed in §3.3.

3.2.3 HI radio observations

NGC 1365 was observed at the VLA in the HI 21 cm line in 1986 (see JvM95) for 48 hours in three different configurations: BnA, CnB and DnC. The observations were collected on 11 different days; further details of the observations are given in JvM95. Motivated by improvements in numerical routines in AIPS and by the puzzling declining rotation curve reported by these authors, RZS spent a summer at NRAO[3] re-analyzing these observations of NGC 1365 under the supervision of Gustaaf van Moorsel.

Data from the different days were reduced independently and then combined in the UV plane using standard AIPS calibration procedures (DBCON, UVLIN). The resulting combined beamsize was $10.3'' \times 9.7''$. Only 31 channels with a corresponding velocity resolution of 20.84 km s^{-1} were used.

An image cube was created with the task IMAGR using robust weighting (see Briggs 1995). Natural and uniform weighting are controlled in AIPS by the robustness parameter and we explored the range from -4 (uniform weighting) to 4 (natural weighting) by measuring the RMS of an empty box in the resulting map and by checking the dirty beam size. A robustness of zero gave the best compromise between noise and beam size. The resulting RMS value was 2.7×10^{-4} Jy/Beam and we cleaned our maps to a depth of 1-σ. Images of HI intensity, velocity field, and velocity dispersion were obtained with XMOM in AIPS after blanking unnecessary channels with the task BLANK.

---

[3]The NRAO is operated by Associated Universities, Inc., under a cooperative agreement with National Science Foundation.

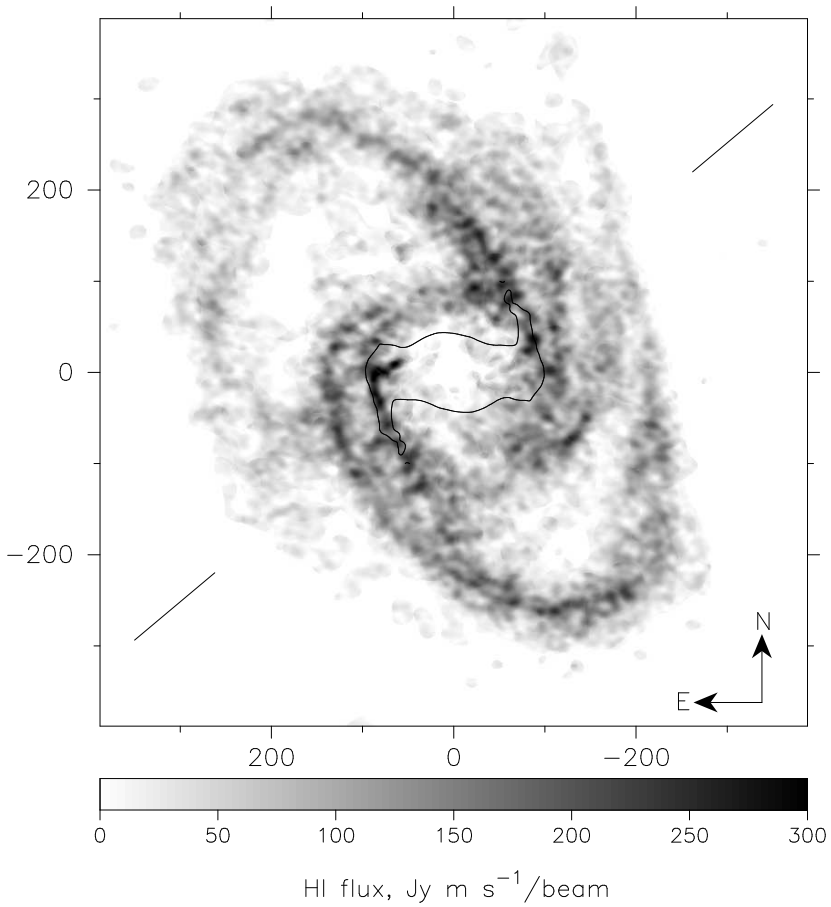

Figure 3.6 The distribution of neutral hydrogen, from the velocity-integrated 21-cm surface brightness. The beam size is $10.3'' \times 9.7''$

The velocity-integrated HI distribution is presented in Fig. 3.6. The eastern spiral arm has a clear double ridge in HI where it joins to the bar, while the inner arm fades farther out. The western arm is also double, possibly even triple, but in this case the innermost arm is that most easily traced to the outer disk. As shown in Fig. 7 of JvM95, the HI distribution extends only slightly farther out than the light; there is very little neutral gas beyond a deprojected radius of $400''$, while we already reported above that $R_{23.5} = 348''$ in the I-band. Furthermore, the outer distribution is asymmetric, with a single spiral arm extending to the NW.

The velocity field mapped in the 21cm line, presented in Fig. 3.7, is nowhere characterized by a simple planar, near-circular flow pattern. The strong bar and spiral arms produce

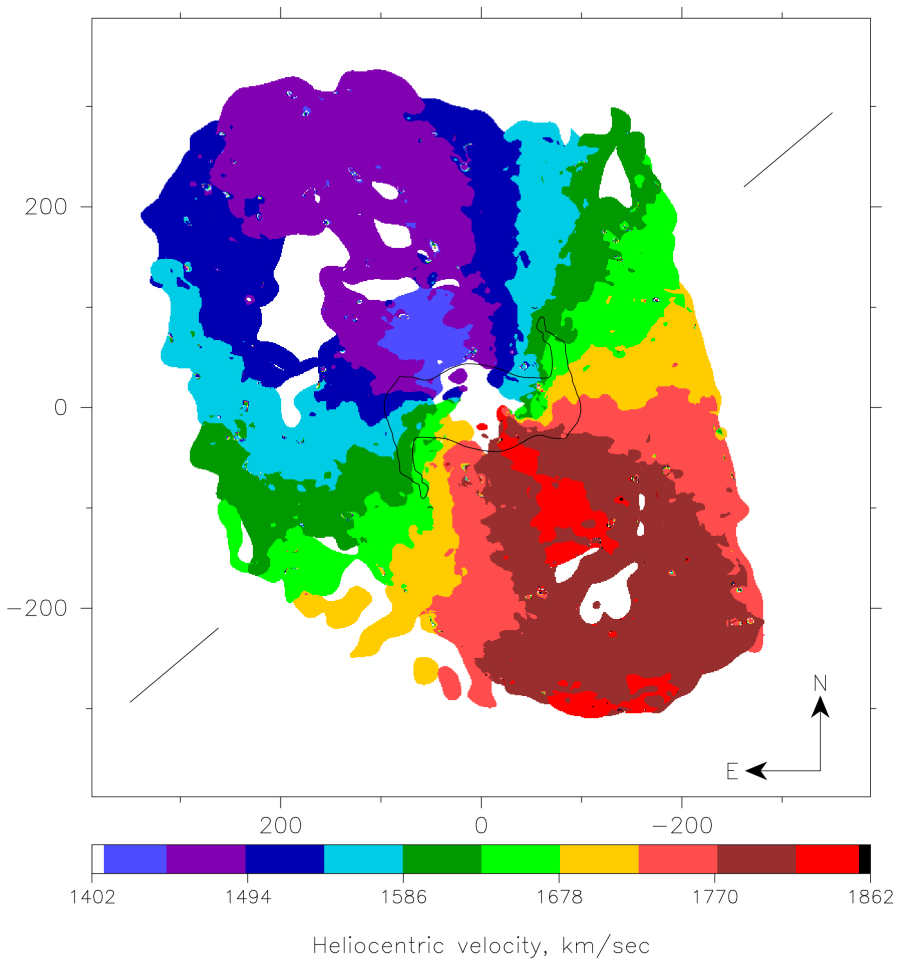

Figure 3.7 The velocity map of NGC 1365 from observations of the 21-cm emission line. The color map has been binned in the same 10 colors used in Fig. 3.5 to outline velocity contours.

non-axisymmetric distortions to the flow pattern that are revealed by kinks in the isovelocity contours. Also a mild warp is suggested by the bending of the isovelocity contours towards the north in the north-east side and towards the south in the south-west side of the galaxy. All of these factors conspire to make the rotation curve of NGC 1365 very difficult to determine. JvM95 concluded that the outer disk was strongly warped, leading them to report a steeply declining rotation curve.

3.3 Asymmetries

While asymmetries of all kinds are evident at larger radii, the inner parts of NGC 1365 are at once remarkably symmetric in the I-band light (Fig. 3.1), and strikingly asymmetric in the position of the dust lane and gas kinematics. The Hα velocities in the bar region also reveal a number of patches of emission with strongly anomalous velocities when compared with the mean flow. These facts point to some kind of on-going disturbance to the gas flow in the inner galaxy that has little effect on the light.

The galaxy is a member of the Fornax cluster; its projected position is near the cluster center, while its systemic velocity differs from the cluster mean by about 200 km/s (Madore *et al.* 1999). Thus the outer parts of NGC 1365 could be affected by the tidal field of the cluster and/or ram-pressure of the intra-cluster gas. However, tidal forces are unlikely to be strong enough to affect the inner parts of this massive galaxy, where asymmetries must have a different origin.

One possibility that NGC 1365 is in the advanced stages of a minor merger. However, the absence of noticeable disturbance to the stellar bar requires that the infalling dwarf had a low enough density to have been tidally disrupted before reaching the bar region. Another possible explanation might be that a stream of gas has fallen in, perhaps from a tidally disrupted cloud or gas-rich dwarf galaxy. Such a stream, which would have to be more substantial than that detected in NGC 6946 (Kamphuis & Sancisi 1993; Boomsma *et al.* 2004) or the high-velocity clouds of the Milky Way (Wakker & van Woerden 1997), may have passed to the west of the center and ahead of the leading side of the bar. The ram pressure of this gas acting on the gas in the galaxy mid-plane might have removed a good fraction of the upstream gas ahead of the original position of the shock, and allowing the shock to advance to its observed position. This scenario is not without its problems, however; most notably, the HI distribution is not noticeably depleted and the velocity pattern is not strongly disturbed where the gas stream is supposed to have punched through the

mid-plane.

Whatever their origin, the peculiarities of the velocity field have proved a major obstacle to the objectives of this study.

3.4 Rotation Curve

We first determine the center, systemic velocity, position angle and inclination from the Hα velocity map using the χ^2 minimization technique proposed by Barnes & Sellwood (2003). Their method uses the entire kinematic map (excluding the sparse gas in the bar region), in order to estimate these projection parameters. We find that the center lies only a few arcsec from the reported position of the nucleus (Lindblad *et al.* 1996), and adopt their quoted position of the nucleus as the kinematic center for the rest of our analysis. The fitted inclination of 41° and PA of 220° agree well with the values obtained from the AIPS routine GAL, while the fitted heliocentric velocity of 1631.5 for the Hα map and 1632 km/s for the HI map are in excellent agreement with the value of 1632 km/s reported by JvM95.

Applying a similar χ^2 minimization to the I-band image yielded the same PA but a higher inclination: $i = 52°$, which is in tolerable agreement with the value $i = 55°$ estimated by Lindblad (1978) also from photometric isophotes (see JvM95 and references therein). The large discrepancy between the kinematic and photometric inclinations is probably due to the strong spiral features that happen to lie near the projected major axis (see Palunas & Williams 2000; Barnes & Sellwood 2003). Since the spiral arms appear to bias the photometric inclination more, we adopt the kinematic inclination of $i = 41°$, consistent with most other work. For completeness, we have also followed our analysis through using the photometric inclination, but find (§ 3.6.1) the kinematic inclination leads to superior fits.

In order to re-estimate the rotation curve from the HI velocity map, we excluded gas beyond a deprojected radius of 255″ (23 kpc) from the center. Although the data extend 133″ (12 kpc) farther, pronounced asymmetries in these outer parts suggest the gas layer

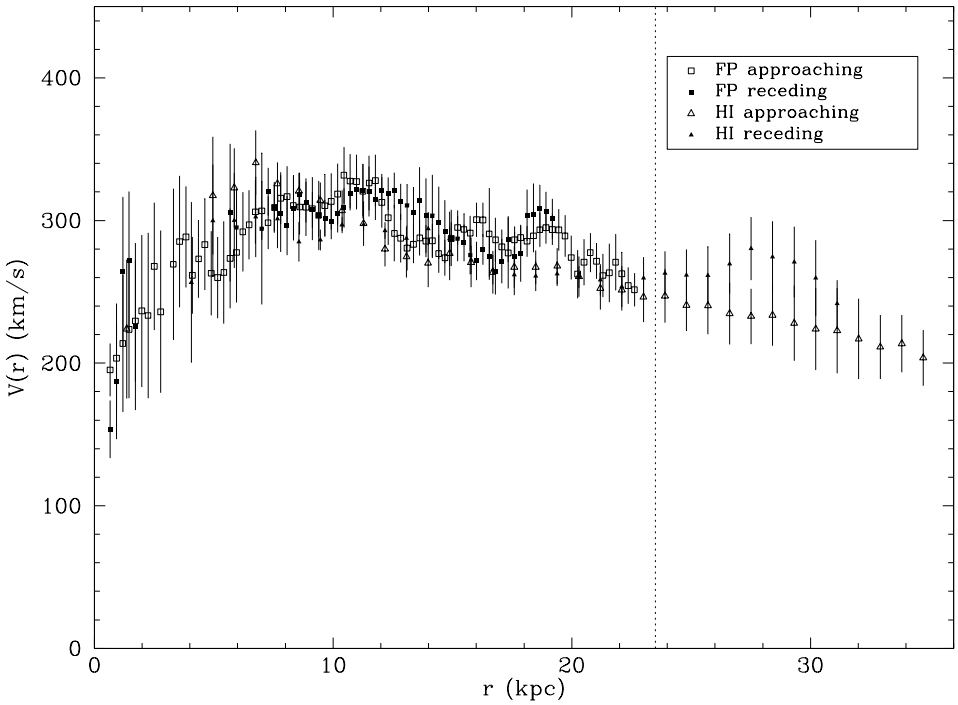

Figure 3.8 Rotation curve from 21-cm and Hα observations. V(r) was fitted for receding and approaching sides independently. Annuli for Fabry-Perot (FP) are 3 arcsec wide and HI map is 10 arcsec. Data outside r=23.5 kpc, marked by the vertical dotted line, has been ignored from our dark matter halo modeling.

is disturbed and may not be in simple rotational balance. While we cannot exclude the possibility that the gas layer in our selected inner region is warped, we here adopt the simpler assumption that the gas in the inner 255″ is everywhere flowing in a single plane.

With the PA, inclination and systemic velocity fixed, we fitted for the circular velocity in annuli of 3 arcsec and 10 arcsec wide for the Hα and HI data respectively. We fitted the approaching and receding sides separately, producing four separate estimates of the rotation curve, which we present in Fig. 3.8. Squares (triangles) represent fits to the Fabry-Perot (HI) observations, and we use open symbols for the approaching side of the galaxy and filled ones for the receding side. The uncertainties in the bar region are large because we here fit simple rotational motion to a flow pattern that is manifestly non-circular; we improve on this below. Fits with standard deviations greater than 60 km/s were discarded. In the inner disk, where we expect the galaxy to be flat, we find the four fitted velocities generally agree

within the estimated uncertainties. However, there are substantial differences between the receding and approaching sides in the HI data beyond the vertical dotted line drawn at $R = 23$ kpc. Accordingly, we exclude data beyond 23 kpc (the region excluded for finding PA, inclination), for fitting our dark matter halo (§3.5.3).

The rotation speed declines significantly outside 10 kpc, although not as steeply as that derived by JvM95. A decline within the visible disk is not uncommon for galaxies of this luminosity (Casertano & van Gorkom 1991; Noordermeer *et al.* 2007).

3.5 Mass models

The first stage of our modeling procedure is to build a family of axisymmetric mass models with differing mass disks that, when combined with a halo, yield our adopted axisymmetric rotation curve, at least in the outer parts.

3.5.1 Disk

We compute the disk contribution to the central attraction by first assuming a fixed M/L ratio (Υ_I) for all the luminous matter, after rectifying the I-band image to face-on and applying a global correction for extinction. We used the inclination and PA obtained from the kinematic maps to perform the deprojection.

A constant Υ_I is a good assumption provided that the stellar population is homogeneous and dust obscuration is negligible. Most variations in the V-I color visible in Fig. 3.2 appear to be due to dust, which affects the V-band surface brightness much more than the I-band. While Fig. 3.1 shows that dust still diminishes the I-band surface brightness, especially in the bar region, we have not attempted to correct for the patchiness of the dust.

As we need the in-plane forces for both the strongly non-axisymmetric light distribution, and for an azimuthally averaged light profile, we adopt the same numerical procedure for both. We assume a finite thickness for the disk with the usual mass profile normal to the plane of the galaxy: $\rho(z) \propto \mathrm{sech}^2(z/2h_z)$ with $h_z = 0.5$ kpc consistent with observations of

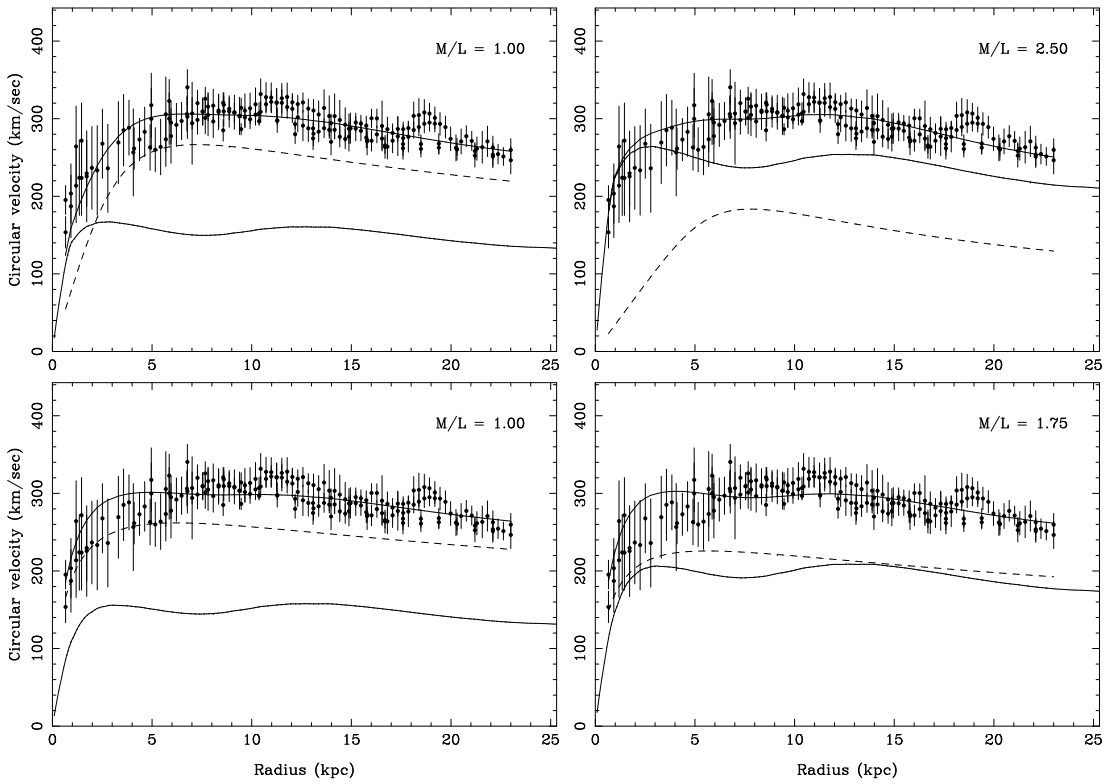

Figure 3.9 Mass models for the rotation curve. *Points and error bars:* Observed rotation curve in both HI and Hα. *Uppermost solid line:* Best-fit total rotation curve. *Dotted line:* Contribution of the best-fit halo. *Lower solid line:* Contribution of the stellar disk to the total rotation curve. The left panels have disk $\Upsilon_I = 1.0$ and the right panels have disk $\Upsilon_I = 2.50$ and $\Upsilon_I = 1.75$. The top panel use pseudo-isothermal halos with bulge b1075. Bottom panels use NFW halos.

edge-on galaxies for our measured disk scale length $r_d = 6.5$ kpc (Kregel, van der Kruit & de Grijs 2002).

Forces from the visible matter scale linearly with the adopted M/L ratio; we explore a discrete set of values for Υ_I ranging from 0.50 to 3.75 in steps of 0.25. Axisymmetric rotation curves from the visible matter for three different Υ_I values are shown by the solid lines in Fig. 3.9.

We have not explicitly determined the contributions from the mass of the neutral and molecular gas to the rotation curve. Most of the neutral gas, $\sim 1.7 \times 10^{10} M_\odot$ after helium correction, is outside the bar whereas all the molecular gas is inside the bar and nucleus, $\sim 1.7 \times 10^{10} M_\odot$ of which $5.4 \times 10^9 M_\odot$ lies in the central 2.0 kpc (see Sandqvist *et al.*

1995). Altogether gas accounts for about 10% of the total mass, as measured from the HI rotation curve (JvM95). The combined distribution of the two phases has a density profile that resembles that of the light and therefore can be taken into account by simply associating the stellar mass-to-light ratio to be roughly 90% of the fitted value. While this approximation neglects the different thicknesses of the star and gas layers, the total rotation curve will be very little affected by taking into account the marginally stronger central attraction from the small fraction of mass in the gas.

3.5.2 Bulge

The assumptions of constant Υ_I and disk thickness at all radii are clearly the simplest we could adopt, but may not be correct, especially in the center. While the light distribution in the inner bar region is somewhat rounder than that in the outer bar, it does not really suggest a spheroidal bulge because deprojection, which stretches the image along the minor axis, still leaves this component roughly aligned with the bar. However, it is possible that the inner bulge-like feature is thicker than the disk and bar and it may also have a higher Υ_I than the rest of the disk.

To allow for a possible enhanced Υ in the inner disk, we consider some simple variants of our constant Υ_I models. For $r \leq r_b$, we scale the Υ_I by the function

$$F(r) = 1 + f \times \left(1 - \frac{r}{r_b}\right)\left(1 + \frac{r}{r_b}\right)^2, \tag{3.1}$$

where r_b is the radius of the bulge and f is a constant. We have adopted three separate values of r_b and of f, and label the five bulge models we study here as b1025, b1075, b2050, b2075, b3075. The first numerical digit denotes r_b in kpc and the last 3 digits are 100 times the value of f; *i.e.* b2050 denotes a model bulge with $r_b = 2$ kpc and $f = 0.50$.

This approach assumes that the possible bulge is as thin as the outer disk, which may not be true. A thicker component would exert slightly weaker central forces, which will result in our fits preferring a slightly lower value of f than the population has in reality. However,

we do not need to know the relative flattening of this mass component; our procedure simply allows for the possibility that it may give rise to some extra central attraction.

As found by Jungwiert, Combes & Axon (1997) for their H-band image, the inner light profile of our I-band image is extended at a different position angle from that of the main bar. Jungwiert *et al.* and Laine *et al.* (2002) suggest this is evidence of a decoupled nuclear bar although an HST NICMOS image resolves this feature into a nuclear spiral (Emsellem *et al.* 2001; Erwin 2004). Whatever the correct interpretation, this distortion in the inner light distribution is inside the region we exclude from our fits to the observed velocities, and does not affect our conclusions.

3.5.3 Halo

The total central attraction should account for the rotational balance, and generally requires a dark halo. We have adopted 2 different dark halo forms: a generalized pseudo-isothermal halo and the NFW density profile (Navarro *et al.* 1997).

In order to fit the declining rotation curve, we adopt a slightly generalized pseudo-isothermal dark matter halo density profile of the form proposed by van Albada *et al.* (1985):

$$\rho(r) = \rho_o \frac{1}{1 + (r/r_c)^k}. \tag{3.2}$$

The exponent k is treated as an independent parameter that allows the halo circular speed to decline if $k > 2$. Since large values of k lead to a halo rotation curve with a sharp, narrow peak, we apply the additional constraint $k \leq 5$.

NFW (Navarro *et al.* 1997) dark halo profiles have the form

$$\rho(r) = \frac{\rho_s r_s^3}{r(r + r_s)^2}. \tag{3.3}$$

For both density profiles we fit the total rotation curve by minimizing χ^2 to find the best fit halo to be combined with each adopted disk Υ_I and bulge model. The results are given in Table 3.1 and Table 3.2, with the values of c and V_{200} being computed for a

Table 3.1. Halo Parameters

Disk Υ_I	ρ_0	r_c	k	χ^2/N	Disk Υ_I	ρ_0	r_c	k	χ^2/N
	b1025					b2050			
1.00	1433.20	1.45	2.61	0.92	1.00	691.78	2.13	2.76	0.92
1.50	420.20	2.64	3.00	0.92	1.50	212.37	3.75	3.31	0.89
2.00	184.70	3.72	3.50	0.91	2.00	109.76	4.75	3.86	0.89
2.50	81.20	5.16	4.78	0.93	2.50	53.03	5.97	5.0	0.95
3.00	67.20	4.60	5.0	0.99	3.00	36.85	5.18	5.0	1.08
	b1075					b2075			
0.50	1422.16	1.58	2.62	0.97	1.00	381.17	2.96	2.98	0.90
0.75	784.56	2.11	2.77	0.96	1.50	166.99	4.20	3.44	0.86
1.00	346.08	3.19	3.10	0.92	2.00	90.10	5.14	3.98	0.90
1.25	354.20	3.01	3.05	0.87	2.50	43.60	6.31	5.0	1.00
1.50	241.21	3.55	3.27	0.86	3.00	30.49	5.23	5.0	1.18
1.75	173.99	4.02	3.51	0.86		b3075			
2.00	126.70	4.51	3.81	0.87	1.00	305.24	3.29	3.05	0.92
2.25	91.30	5.06	4.29	0.89	1.50	134.05	4.59	3.52	0.88
2.50	62.55	5.72	5.0	0.92	2.00	82.60	5.06	3.76	0.92
2.75	56.43	5.41	5.0	0.97	2.50	32.46	6.63	5.0	1.05
3.00	49.10	4.87	5.0	1.06	3.00	14.77	5.85	5.0	1.26
3.25	49.92	4.06	5.0	1.21					
3.50	18.16	3.87	5.0	1.36					
3.75	2.02	1.36	5.0	1.70					

Note. — Dark matter halo parameters for five different bulge models. For models with $\Upsilon_I = 2.75$ and 3.00, the k parameter was fixed to 5 to avoid a sharp edge on the halo profile

Hubble constant $H_0 = 70$ km s^{-1} Mpc^{-1}. No bulge modification was applied to the NFW halo since extra bulge mass combined with the cuspy halo would have complicated the fits to the inner rotation curve. Figure 3.9 shows possible fits to the data with different Υ_I exemplifying the disk-halo degeneracy for both dark matter halo profiles adopted. The pseudo-isothermal profile plotted uses a bulge model b1075.

Both our adopted halo functions assume spherical symmetry, whereas we need assume only that the halo is axisymmetric in the disk plane. The flow pattern in our simulations depends on Υ_I and the corresponding halo attraction; the possible flattening of the halo affects only the interpretation of the halo attraction in terms of a mass profile. As a flattened halo gives rise to stronger central attraction in the mid-plane for the same interior mass (*e.g.* Fig. 2-12 Binney & Tremaine 1987), the simplest assumption of spherical symmetry

Table 3.2. NFW Halo Parameters

Disk Υ_I	ρ_s	r_s	c	V_{200}	χ^2/N
0.50	829.96	2.90	67	135	0.92
0.75	802.80	2.84	66	131	0.93
1.00	710.48	2.87	63	127	0.90
1.25	685.32	2.80	62	122	0.92
1.50	662.08	2.71	61	116	0.93
1.75	641.40	2.61	61	111	0.96
2.00	563.16	2.61	58	106	0.98
2.25	182.60	3.94	38	105	1.16
2.50	190.40	3.55	38	96	1.15
2.75	208.36	3.08	40	86	1.15
3.00	240.20	2.54	42	75	1.17
3.25	229.16	2.22	41	64	1.26
3.50	173.00	1.85	37	48	1.33
3.75	0.36	2.17	3	4	1.42

Note. — Dark matter halo parameters for NFW halo. The densities are in $10^{-3} M_{\odot} pc^{-3}$, the radii in kpc, and V_{200} is in km s^{-1}.

allows a more massive halo than would be required if the halo were significantly oblate.

3.6 Gas Dynamics simulations

We here give a brief summary of our procedure; see Weiner *et al.* (2001) for a more detailed description. As usual, we neglect self-gravity of the gas, which would add considerably to the computational complexity of our many simulations. This simplifying assumption is justified because the gas density in the bar, where we are most interested in comparing with the observed velocities, is a small fraction of the mass in stars.

We compute the gas flow using the flux splitting code written and tested by van Albada (1985) and kindly provided by Athanassoula. Pérez (2007) has shown that results from the 2-D code we use and the 3-D SPH code used in her work agree very well for the same mass model, which is reassuring.

Since the I-band light has excellent 2-fold rotation symmetry (Fig. 3.1), we force bi-symmetry in the simulations and employ an active grid covering only one half of the galaxy.

In order to avoid initial transients resulting from non-equilibrium starting conditions, we begin our simulations in an axisymmetric potential, and gradually change to the full non-axisymmetric barred potential over the first 2.5 Gyr of evolution. Careful inspection of the simulations revealed that the gas does not settle to a quasi-steady flow until several bar rotations (3 Gyr or from 6 to 15 rotations for $\Omega_p = 12$ and 32 respectively) are completed. At this time, we take a snapshot of the simulation and compare it to the data. We stress that the final state of the gas doesn't depend on the growing time, but the bar growth rate does affect how quickly the gas flow settles down.

We experimented with different sound speeds and grid resolutions, which generally yielded reproducible results except in the central few resolution elements. We found that flows at the highest resolution (grid cell size 128 pc) did not ever settle to quasi-steady patterns for the most massive disks, but did do so for a cell size of 300 pc; this change in behavior is caused by the stabilizing influence of greater numerical viscosity on the coarser grid. We therefore work with the results from simulations with a grid cell size of 300 pc for all disk masses.

Modeling the ISM with a simple fluid code is clearly an approximation. An isothermal equation of state with sound speeds in the range 6 to 10 km s^{-1} is reasonably appropriate for the warm neutral and warm ionized components, which have temperatures of $\sim 10^4$ K, and we attempt to fit our models to the observed kinematics of the ionized component. The neutral HI component of the Milky Way (Gunn, Knapp & Tremaine 1979) and other galaxies (*e.g.* Kamphuis 1993) is also observed to have intrinsic line widths in this range. Furthermore, dense clouds are observed also to maintain a velocity dispersion of ~ 8 km s^{-1} (Stark & Brand 1989). Englmaier & Gerhard (1997) showed that the gas flow pattern in their simulations changed materially when they increased the sound speed to 25 km s^{-1}; however, such a large sound speed is not representative of any dynamically significant component of the ISM. We therefore confine our tests of the gas parameters to realistic ranges, and find the significant properties of the flow are almost independent of the exact

values adopted.

The non-circular flow pattern produced by a bar depends both on the mass of the bar and its pattern speed or rotation rate (Roberts *et al.* 1979). For the photometric disk model described above, the bar mass scales directly with the adopted Υ_I, while the total central attraction includes the contribution from the adopted halo, which is assumed to be axisymmetric. For each adopted Υ_I ratio, we compute the gas flow in the disk plane using 2-D gas dynamics simulations, for a number of different bar pattern speeds, Ω_p. We project the resulting flow patterns as the galaxy is observed, and compare with Fabry-Perot velocity maps using a χ^2 analysis to find the best match to the observations, in order to estimate the disk Υ_I and Ω_p.

We explored pattern speeds in the range $12 \leq \Omega_p \leq 32$ km s^{-1} kpc^{-1}, corresponding to corotation radii in the range $2.0 r_B \gtrsim r_L \gtrsim 0.9 r_B$. In all we ran 154 simulations to cover the grid in Ω_p and Υ_I for each of the pseudo-isothermal and NFW halo models.

3.6.1 Comparison between models and data

Before attempting any comparison between simulations and data, it is necessary to smooth the simulations to the atmospheric seeing during the observations and also by the largest kernel used to produce the velocity map (see §3.2.2), which requires a smoothing kernel of FWHM = $4''$. Kamphuis (1993) reports that the velocity dispersion of HI gas rises inwardly for a number of galaxies to values that exceed 10 km s^{-1} in the bright inner parts of massive galaxies. Since the velocity in each pixel may reflect that of an individual HII region, we add 12 km s^{-1} in quadrature to the formal error estimates of the Hα velocities to allow for a possible peculiar velocity relative to the mean flow.

Since our simulations assume a gas with a finite sound speed, the full non-linear velocity distribution at every point takes into account our adopted velocity spread. No further correction, *e.g.* for asymmetric drift, is therefore needed.

We compare the projected snapshot from the simulation using the standard goodness

of fit estimator

$$\chi^2 = \frac{1}{N}\sum_{i=1}^{N} z_i^2, \tag{3.4}$$

where the summation is over all N pixels in the region selected for comparison, and z_i is the usual difference between the observed velocity $V_{i,\mathrm{obs}}$ and that predicted from the simulation $V_{i,\mathrm{mod}}$, weighted by the uncertainty σ_i; viz.

$$z_i = \frac{V_{i,\mathrm{obs}} - V_{i,\mathrm{mod}}}{\sigma_i}. \tag{3.5}$$

We include 2280 pixels in the fit, but they are not all independent because of seeing and smoothing. Furthermore, the quantity χ^2 is regularized somewhat by adding 12 km s^{-1} in quadrature to the errors. Thus it is not a formal estimator of confidence intervals, but can be used to compare relative goodness of fit.

Our mass model is bi-symmetric, in line with the light in this galaxy, but the velocity data are not. Our simulations are therefore unable to fit both sides of the bar simultaneously[4]. Since the dust lane and steep velocity gradients are quite uncharacteristically almost outside the bar on the west side, we confine our fits to the east side, where we suspect that the flow pattern is less disturbed.

We further restrict the region from which we evaluate χ^2 to only those pixels in the area between the inner ellipse and the outer rounded rectangle shown in Fig. 3.5, because our models are most sensitive to the parameters we have varied in this region. The inner ellipse has a semimajor axis of 35″ and ellipticity 0.5, while the semi-axes of the outer curve are 80″ & 42″. We exclude the center for several reasons: the observed velocities are degraded somewhat by beam smearing, our assumptions of a thin disk are most likely violated in the center (see section 3.5.2), and the predicted gas velocities vary with grid resolution in this region. We exclude data in the spiral arms because the gas flow outside the bar never settles to a steady pattern in our simulations, and some studies (*e.g.* Sellwood & Sparke 1988) suggest that these features evolve over time.

[4]Since the I-band light distribution is almost perfectly bisymmetric (Fig. 1), relaxing the assumption of bi-symmetry had a negligible effect on the model predictions.

The value of χ^2 varies substantially as the two parameters are varied, but the minimum remains large, even when we restrict the region of comparison with the data to the eastern half of the bar. Maps of the residuals, shown below, reveal a number of isolated regions with substantially discrepant velocities that coincide with the regions labeled in Fig. 3.5. In order to check whether the position of the minimum was being displaced by the pixels with large anomalous velocities, we employed Tukey's biweight estimator (Press *et al.* 1992)

$$\chi^2_{\rm bw} = \frac{1}{N}\sum_i \begin{cases} z_i^2 - z_i^4/c^2 + z_i^6/(3c^4) & |z_i| < c, \\ c^2/3 & \text{otherwise}, \end{cases} \tag{3.6}$$

with the recommended value for the constant $c = 6$. In fact, the position remained unchanged for both the isothermal and NFW halos, and we revert for the remainder of the paper to the usual χ^2 statistic defined by eq. (3.4).

The minimum of the reduced χ^2 is unreasonably high: $\chi^2 = 2.7$ for the best isothermal halo and $\chi^2 = 2.4$ for the NFW halo. It is evident from the residual maps (Figure 3.10a & b) that a large part of the mismatch from the model comes from the five anomalous regions identified already in Fig. 3.5. We therefore masked each of these regions with circular mask of radius 4 or 5 pixels, which decreased the minimum of χ^2 to 1.6 for the isothermal models and 1.5 for then NFW halo models. While these values are still on the high side, we should not expect $\chi^2 = 1$ since the fluid model is idealized. We therefore consider we have satisfactory models for most of the flow pattern in the eastern half of the bar.

Since we approximate the ISM as an isothermal gas, the shock in the simulations must be as close as the code can resolve to a discontinuity, whereas it is possible that gas velocities in NGC 1365 vary more gradually. We therefore experimented with additional smoothing of the simulations above the FWHM = $4''$ that matches the resolution of our data. The value of χ^2 decreases considerably to $\chi^2 = 1.3$ when we smooth the simulations by $10''$, although the position of the minimum did not change. At least some of this improvement appears to result from a better match to the velocity gradient across the shock. We have not included this extra smoothing in the fits below, however, because it degrades our resolution

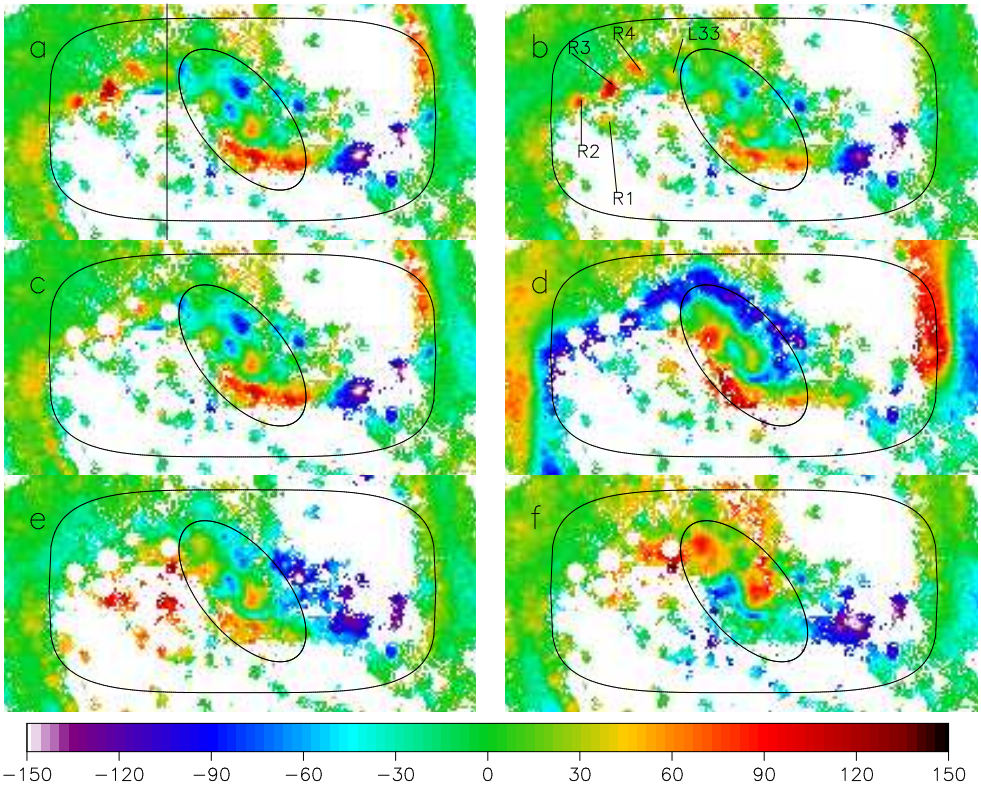

Figure 3.10 (a) & (b) Residual maps for respectively the best-fit pseudo-isothermal and NFW halo models. The velocities of the anomalous HII regions, identified in (b), are shown in these two panels only. The N-S line in (a) is described in §3.6.3. (c)-(f) 4 characteristic b1075 models, with the anomalous HII regions masked out: *c.)* Υ_I = 2.50, Ω_p =24; *d.)* 1.0,24; *e.)* 2.50,16; *f.)* 1.0,16.

everywhere and reduces the curvature of the χ^2 surface.

3.6.2 Best fit models

Figure 3.11 shows contours of χ^2 in the space of the two principal parameters: Υ_I & Ω_p. The quantity contoured is the value from eq. (3.4) using pixels from the east side of the bar only with the 5 anomalous regions masked out.

For the pseudo-isothermal halos, models with low pattern speed and high Υ_I are very strongly disfavored and the χ^2 function also rises strongly, but somewhat less steeply towards higher pattern speeds and low Υ_I. We show the residual map for the best fit parameters and, for comparison, three other cases for two different values of Ω_p and Υ_I in Figure 3.10(c)-(f).

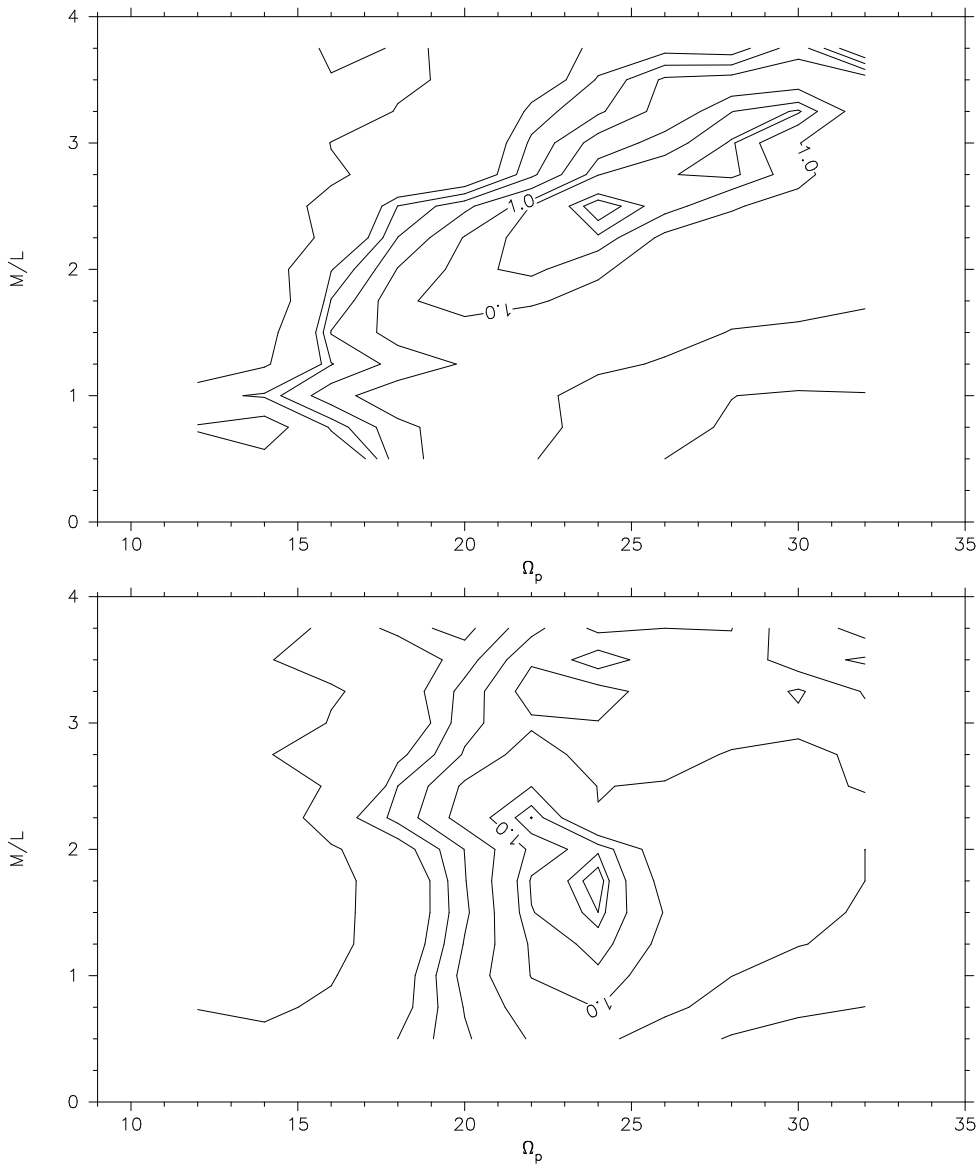

Figure 3.11 *Upper:* The χ^2 surface for the b1075 pseudo-isothermal model. The minimum value (1.6) lies at $\Upsilon_I = 2.50$ and $\Omega_p = 24$. Contours are drawn at $\Delta\chi^2/N = 0.1$, 0.2, 0.5, 1, 2, 3, 4, 5 & 10 above the minimum. *Lower:* The same for the NFW halo model. The minimum is 1.5 for model with $\Upsilon_I = 1.75$ and Ω_p=24.

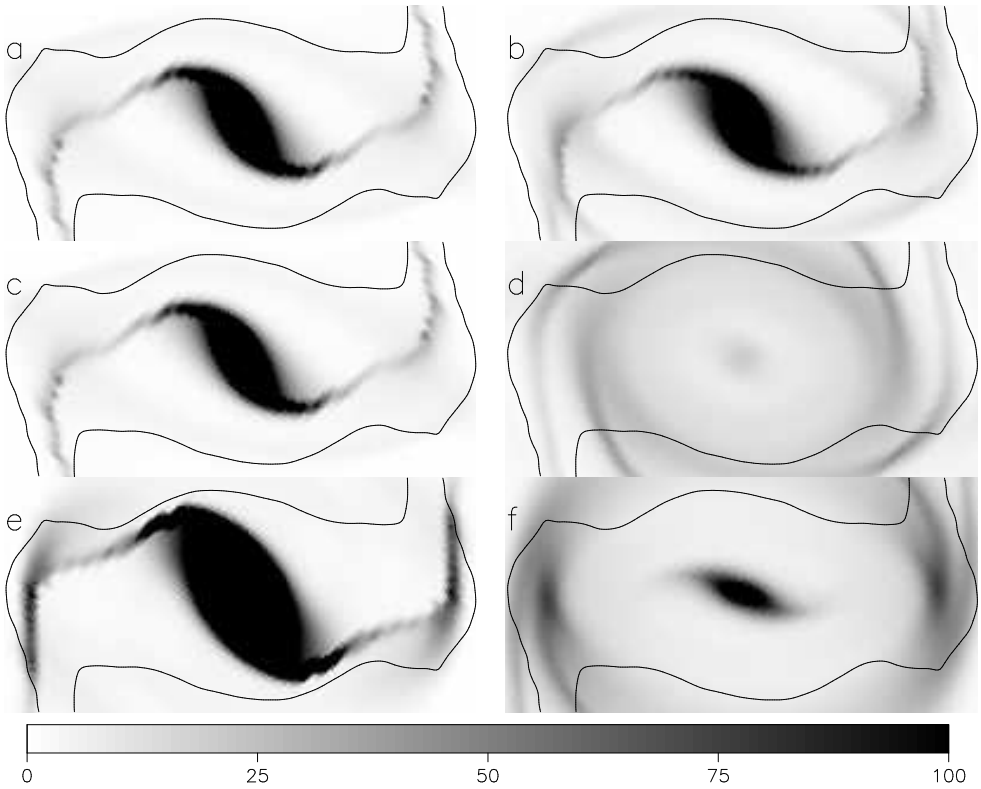

Figure 3.12 Gas surface density in the same models shown in Fig. 3.10, panels (a) & (c) are identical, therefore. Panels (c) thru (f) show that the density response to bar forcing changes dramatically as the disk mass and pattern speed are varied.

Figure 3.12 shows the gas density response in the inner regions of the same set of models. Shocks are regions of locally high gas density along the bar that coincide with steep velocity gradients in the flow. The shocks in the best fit models (top row) are displaced towards the leading edge of the bar, as usual, and all-but disappear in the low-mass disks, panels (d) & (f). The shocks in panel (e) are too far towards the bar's leading edge, and the inner oval is too large, because the x_2 family that is responsible for this behavior (Sellwood & Wilkinson 1993) grows in spatial extent as the pattern speed is reduced. Although the position of the dust lane in the west of the bar is indeed shifted towards the leading edge, it does not have the shape predicted by low pattern speed models.

It is difficult make a more quantitative comparison between the gas density in the models and that observed. We do not have sufficient information about the distribution of all the multiphase components of the ISM; we do not have a complete CO map, and the spatial

resolution of the HI map from the VLA is too low to attempt a meaningful fit.

The best fit pattern speed for both the pseudo-isothermal and NFW halos is for $\Omega_p =$ 24 km s^{-1}kpc^{-1} which places corotation at $r_L \approx 1.23 r_B$. This value of Ω_p is in good agreement with that obtained by Lindblad, Lindblad & Athanassoula (1996) in their bar-only model (after correcting their assumed distance to ours).

However, the minimum χ^2 is at $\Upsilon_I = 2.50$ for the pseudo-isothermal halos, whereas the somewhat lower value $\Upsilon_I = 1.75$ is preferred for NFW halo models. The rotation curve decompositions for these two models are show in the right hand panels of Fig. 3.9. An estimate of the statistical uncertainty in the parameters is indicated by the $\Delta\chi^2 = 1$ contour in Fig. 3.11. Both results are in agreement with each other within the uncertainties and favor fast bars and moderately massive disks.

Finally, we reworked our entire analysis using the photometric inclination of $i = 52°$ instead of the conventionally adopted kinematic inclination of $i = 41°$ in the foregoing analysis. This required redetermining the gravitational potential of the differently oriented and projected bar and disk, refitting for the halo parameters for each adopted Υ_I, and running a new grid of models over the two free parameters. The resulting fits were far worse, with the minimum value of $\chi^2 \simeq 3.8$, even after masking out the HII regions having anomalous velocities. This test confirms that the kinematically-determined inclination is the more appropriate.

3.6.3 Pseudo-slit cut through data

Shocks across dust lanes are readily identified as steep velocity gradients. The data points in Figs. 3.13 and 3.14 show the observed velocities along a pseudo-slit placed perpendicular to the bar major axis as shown in Fig. 3.10(a); this cut across the bar has the most extensive data. The lower panel shows the V-I color along the same line, which reveals that the projected velocity gradient of almost 200 km s^{-1} is coincident with the prominent dust lane. The vertical dotted lines mark the bar width as presented in the bar isophote

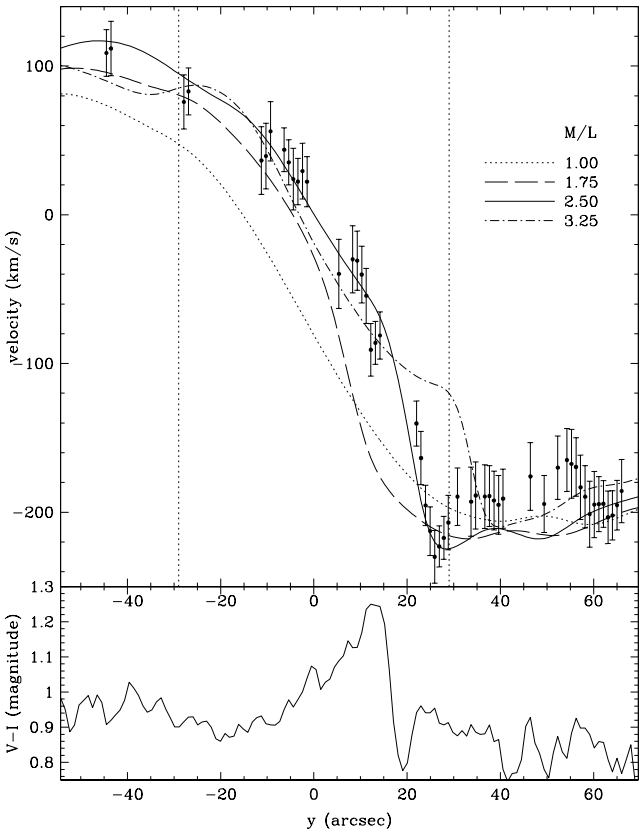

Figure 3.13 Data points with error bars show the Hα velocities along a pseudoslit passing perpendicular through the bar as indicated in Fig. 3.10(a). The two vertical dotted lines mark the width of the bar. Different curves show the simulated velocities in models with different Υ_I ratios for $\Omega_p = 24$ and the b1075 model. Lower panel shows the color profile along the same pseudoslit through our extinction map (Fig. 3.2).

in Figs. 3.1 and 3.2. The other lines in the upper panel show velocities from our b1075 isothermal simulations for different Υ_I with a fixed $\Omega_p = 24$ km s^{-1}kpc^{-1} (Fig. 3.13) and for different Ω_p for a fixed $\Upsilon_I = 2.50$ (Fig. 3.14).

These figures show that $\Upsilon_I = 1$ does not produce a strong enough shock, and $\Omega_p \neq 24$ puts the shock/velocity gradient in the wrong place. In fact, the systematic dependences of the velocity gradient on Υ and on Ω_p are quite similar to those shown in the pseudoslits for NGC 4123 (Weiner *et al.* 2001), where the effects of these physical parameters are explained.

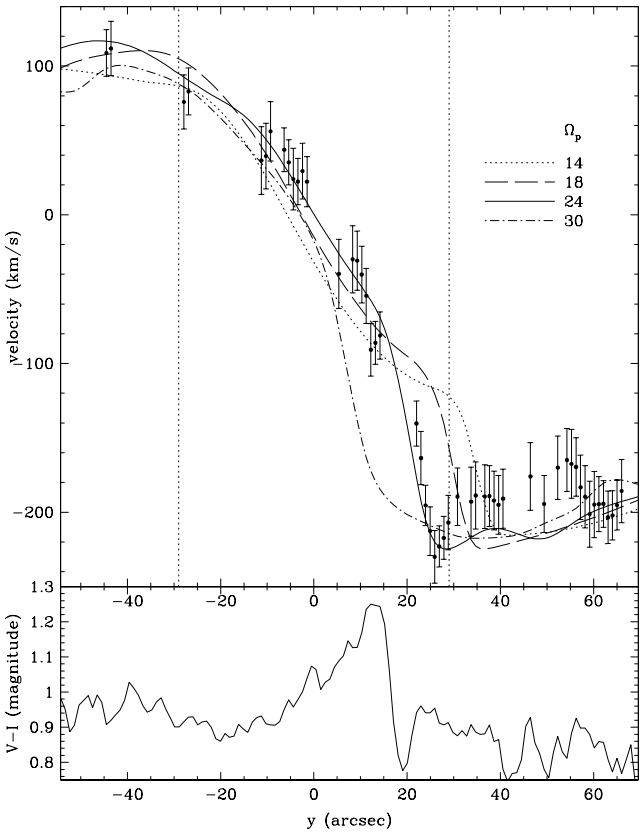

Figure 3.14 As for Fig. 3.14 but here the curves show simulations having different Ω_p for fixed $\Upsilon_I = 2.50$.

3.7 Discussion

In the previous section, we argued that the underlying gas flow in the eastern half of the bar can be modeled with a somewhat massive disk embedded in one of two different halos. Neither model makes a compelling fit, however, and the properties of both best-fit halo models are distinctly non-standard. The outer profile of both our fitted dark halo models already yields a declining circular speed by the edge of the visible disk. This finding may simply be a reflection of a mis-estimated rotation curve, possibly due to a warp or tidal disturbance. However, in their attempt to fit a warp, JvM95 obtained a more strongly declining rotation curve, which would require a still less orthodox halo model.

3.7.1 Disk mass

Our principal finding is that the bar must be massive and rapidly rotating in order for the underlying gas flow pattern to resemble that observed. We obtain improved fits with the isothermal model when we increase the baryonic mass in the inner (bulge-like) region and also when we adopt a halo function that has a high density near the center. This fact suggests that the flow pattern requires a high density in the center, but cannot determine whether the mass should be flattened or spherical, baryonic or dark.

3.7.2 Dynamical friction

The disk contribution to the central attraction in our best fit model with the NFW halo function, though large, is not fully maximal (Fig. 3.9), yet the bar is required to be fast. This model therefore presents the additional puzzle that dynamical friction (Debattista & Sellwood 2000) has not slowed the bar. The uncertainty in Υ_I is great enough that more massive disks are acceptable, although such models would further increase the uncomfortably high ratio of baryonic to dark mass of the best fit model. A lower value of Υ_I may allow a more reasonable baryonic fraction, but exacerbates the puzzle of the fast bar in a yet denser halo.

3.7.3 Halo decompression

The halo of our best-fit NFW model has $V_{200} = 111$ km s^{-1} and a concentration $c = 61$. These parameters, which are defined in Navarro *et al.* (1997), are not in line with the predictions of LCDM theory (*e.g.* Bullock *et al.* 2001); the concentration is very high and the value of V_{200} much lower than expected for a large galaxy.

However, these fitted parameters are for the current halo of NGC 1365, which must have been compressed as the massive disk formed. We have therefore adopted the procedure described by Sellwood & McGaugh (2005) to try to determine the parameters of the original uncompressed halo before the disk formed. The value $\Upsilon_I = 1.75$ for our best fit model

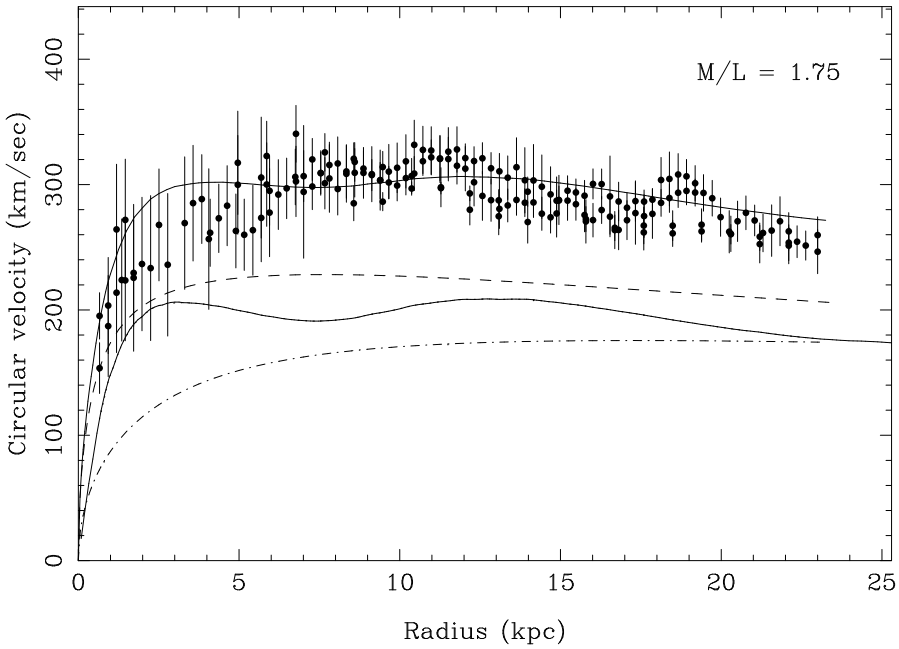

Figure 3.15 Rotation curve of the compressed NFW halo model. The dot-dash line shows the uncompressed halo, the dashed line shows the halo after compression, while the other two lines show the disk contribution and the total rotation curve.

yields a disk mass $M_d = 1.6 \times 10^{11}$ $M_\odot$, which must have condensed from the original uncompressed halo to its present radial distribution. Assuming the dark matter in the original halo to have an isotropic velocity distribution, we determine the final mass profile of the dark matter from some assumed initial NFW form. We proceed by trial and error to determine the initial halo that yields a final rotation curve that closely resembles the fit shown in the right-bottom panel of Fig. 3.9 for $\Upsilon_I = 1.75$

We find that an initial NFW halo with the properties $c = 22$, $V_{200} = 123$ km s^{-1}, $M_{200} = 5.9 \times 10^{11}$ $M_\odot$, and $r_s = 8$ kpc resembles the mass model of the final best-fit NFW halo, as shown in Figure 3.15. The inner halo is an excellent match, but the density of the compressed halo is fractionally higher than in Fig. 3.9 beyond $r = 10$ kpc, which we tolerate because it errs on the side of allowing a more massive halo. Nevertheless, the concentration is still high, though less extreme than if compression is neglected, and V_{200} is still low for such a massive galaxy. Furthermore the disk mass fraction, $M_d/M_{200} \simeq 0.27$ is much greater than the expected value of ~ 0.05 (e.g. Dutton *et al.* 2007). Since our

Table 3.3. Comparison with Population Synthesis

Galaxy	B	V	I	Pred 1 Υ_I	Pred 2 Υ_I	Dynamical Υ_I
NGC 4123	11.97	11.38	10.36	1.22	1.48	2.25 ± 0.25
NGC 3095	11.72	11.16	10.10	1.16	1.67	2.00 ± 0.25
NGC 1365		9.21	8.05		2.28	2.00 ± 1.00

Note. — Our galaxy isophotal magnitudes in 3 color bands corrected for internal and foreground extinction. Prediction 1 Υ_I is from B-V color using Bell *et al.* (2003) table 7. Prediction 2 Υ_I from V-I color using Bell & de Jong (2001) table 1. Our dynamical estimate of Υ_I.

estimated value even exceeds the cosmic dark matter fraction (Spergel *et al.* 2007), it may indicate an unusual formation history for this galaxy.

3.7.4 Population synthesis models

In this study, we have obtained a dynamical estimate of Υ_I for NGC 1365. In previous work, we obtained estimates by the same procedure for NGC 4123 (Weiner *et al.* 2001) and NGC 3095 (Weiner 2004). Here we compare our estimated values of Υ_I with the predictions from population synthesis models by Bell *et al.* (2003) for a galaxy of the observed B-V color. Since Bell *et al.* (2003) do not give predictions for our measured V-I color index, we also compare with the earlier predictions of Bell & de Jong (2001).

Table 3 presents the comparison for all three galaxies. We give isophotal magnitudes corrected for internal (Giovanelli *et al.* 1994; Sakai *et al.* 2000) and foreground extinction (Schlegel, Finkbiner & Davis 1998), and determine the predicted Υ_I from the B-V color using table 7 of Bell *et al.* (2003), and from the V-I color using table 1 of Bell & de Jong (2001). Bell *et al.* (2003) suggest the uncertainty in their prediction is 0.1 dex, or some 25%. The final column gives our dynamically-estimated value of Υ_I for each of the three galaxies.

Our dynamical estimates of $\Upsilon_I \simeq 2 - 2.25$ agree reasonably well with the values of 1.5

– 2.1 deduced from the stellar population V-I colors for a "diet Salpeter" IMF (Bell & de Jong 2001). However, our dynamical modeling estimates are higher than those inferred from B-V colors (Bell *et al.* 2003), suggesting that these galaxies are somewhat bluer in B-V for a given V-I than are the stellar population models; B-V is more sensitive than V-I to the details of recent star formation.

Our fluid dynamical Υ_I values provide a zeropoint normalization for the stellar population models that is at or slightly higher than the preferred normalization of de Jong & Bell (2007). The present work makes this conclusion firmer by removing some distance uncertainty in Υ, since NGC 1365 has a Cepheid distance while NGC 3095 and NGC 4123 do not. The Υ_I values from dynamics make it difficult to have a very low disk, $\Upsilon_I \lesssim 1.0$, as advocated by some authors to reconcile the Tully-Fisher relation zeropoint or lack of radius dependence with theoretical expectations (Portinari, Sommer-Larsen & Tantalo 2004; Pizagno *et al.* 2005).

3.8 Conclusions

We have presented a detailed study of the strongly-barred galaxy NGC 1365, including new photometric images and Fabry-Perot spectroscopy, as well as a detailed re-analysis of the neutral hydrogen observations by Jörsäter & van Moorsel (1995). We find the galaxy to be at once both remarkably bi-symmetric in its I-band light distribution and strongly asymmetric in the distribution of dust and gas, and in the kinematics of the gas. These asymmetries extend throughout the galaxy, affecting the bar region, the distribution of gas in the spiral arms and the neutral hydrogen beyond the edge of the bright disk. The velocity field mapped in the Hα line showed bright HII regions with velocities that differed by up to ~ 80 km s^{-1} from that of the surrounding gas. Our sparsely-sampled line profiles in these anomalous velocity regions hint at unresolved substructure, suggesting a possible double line profile.

The strong bar and spiral arms complicate the determination of the projection geometry

of the disk, assuming it can be characterized as flat in the inner parts. The inclination of the plane we derive from the kinematic data is smaller by about 10° from that determined from the photometry. The strong spiral arms that cross the projected major axis far out in the disk seem likely to bias the photometric inclination and we therefore adopt, in common with other workers, the inclination derived from the gas kinematics. This preference is supported by the much poorer fits to the observed kinematics obtained when we adopt the photometric inclination (§ 3.6.1).

Our attempts to derive the rotation curve of NGC 1365 were complicated by the fact that neither the Hα nor the HI velocity maps are consistent with a simple circular flow pattern over a significant radial range. The bar and spirals clearly distort the gas flow in the luminous disk. The neutral hydrogen extends somewhat beyond the visible disk but unfortunately has neither a uniform distribution nor regular kinematics. JvM95 attempted to fit a warp to the outer HI layer that extends into the visible disk, and derived a strongly declining rotation curve. We chose instead to assume a coplanar flow out to a deprojected radius of 255″ and to neglect the asymmetric velocities in the neutral hydrogen beyond. The velocities derived separately from the Hα and HI data are in good agreement. Our resulting rotation curve shows a gentle decrease beyond a radius of $\sim$ 10 kpc, similar to those observed in other massive galaxies (Casertano & van Gorkom 1991; Noordermeer *et al.* 2007).

We used our deprojected I-band image to estimate the gravitational field of the luminous matter, which can be scaled by a single mass-to-light ratio, Υ_I. We also employed a gradual increase to Υ_I in the central few kpc to allow for an older bulge-like stellar population, although the light distribution does not appear to have a substantially greater thickness near the center. We combined the central attraction of the axially-symmetrized disk for various values of Υ_I with two different halo models to fit the observed rotation curve in the region outside the bar – finding, as always, no significant preference for any Υ_I.

We attempt to fit hydrodynamic simulations of the gas flow pattern in the bar region, in

order to constrain Υ_I. For each type of halo adopted, we run a grid of simulations covering a range of both Υ_I and Ω_p, the pattern speed of the bar. We then project each simulation to our adopted orientation of the galaxy and compare the gas flow velocities in the model with those observed. Since the light distribution in NGC 1365 is highly symmetric, our simulations were constrained to be bi-symmetric, yet the observed gas flow has strong asymmetries. None of our simulations is capable, therefore, of fitting both sides of the bar simultaneously.

The anomalous position of the dust lane in the western part of the bar suggests that side is the more likely to be disturbed, and we therefore fit our models to the eastern half of the bar only. After smoothing the model to match the resolution of the kinematic data and masking out five blobs of gas with strongly anomalous velocities, we are able to obtain moderately satisfactory fits to the remaining velocities. The best fit pattern speed is $\Omega_p = 24$ km s^{-1}kpc^{-1} for both types of halo which places corotation for the bar at $r_L \simeq 1.23 r_B$, in excellent agreement with the value found by Lindblad, Lindblad & Athanassoula (1996) and consistent with most determinations of this ratio for other galaxies (*e.g.* Aguerri, Debattista & Corsini 2003).

Our estimated mass-to-light ratio values are $\Upsilon_I \simeq 2.50 \pm 1$ for the isothermal halo models and $\Upsilon_I = 1.75 \pm 1$ for the NFW halo. While the constraints are disappointingly loose, the preferred mass-to-light ratio in both our halo models, $\Upsilon_I \simeq 2.0 \pm 1$, is consistent with that obtained by Weiner *et al.* (2001) and Weiner (2004) in two other cases. For NGC 1365, however, this value implies a massive, but not fully maximal, disk, and we do not find support for the disk-only model with no halo that was suggested by JvM95. Although such a model can reproduce the declining rotation curve (see their Fig. 24), the simulated gas flow produced by such a model (which in the I band is $\Upsilon \sim 3.75$) is quite strongly excluded.

The preferred value of Υ_I is nicely consistent with those obtained in the two previous studies using this method (Weiner *et al.* 2001; Weiner 2004), but suggest somewhat more

massive disks than predicted by population synthesis models (Bell & de Jong 2001; Bell *et al.* 2003) for galaxies of these colors.

The halos of our two models required to fit the declining rotation curve in the outer disk are distinctly non-standard, however. The circular speed in the pseudo-isothermal model declines steadily outside the large core, while the NFW halo has a very high concentration and small scale radius. Even allowing for compression of the halo as the massive disk forms within it, the original NFW halo has $c \simeq 22$, $V_{200} \simeq 123$ kms. The total dark matter mass out to r_{200} in this case is less than three times our estimated disk mass, and the halo is quite unlike those predicted by LCDM models for a galaxy of this mass.

The disturbed distribution and kinematics of the gas in this galaxy clearly complicates our attempt to identify a preferred mass model. Its projected position near the center of the Fornax cluster, together with its velocity within 200 km s^{-1} of the cluster mean, suggest it is a cluster member. The disturbed nature of the outer HI distribution should not therefore be regarded as surprising. But the high central density of this massive galaxy should ensure that tidal forces have little influence on the inner part, where we indeed see that the bar and inner spirals are very pleasingly bi-symmetric in the I-band light. The existence of such strong asymmetries in the inner parts of the gas and dust is rather surprising, therefore.

The asymmetry in the dust distribution and the kinematic map, combined with the existence of a number of patches of Hα emission with anomalous velocities all suggest that the agent that caused the disturbance was an infalling gas cloud. We cannot say whether the gas was an isolated intergalactic cloud not associated with a galaxy, or whether it could be a stream of debris from a gas-rich dwarf galaxy that had been tidally disrupted. The anomalous velocities clearly suggest that the infalling gas has yet to be assimilated in the disk of NGC 1365.

Bibliography

Aguerri, J. A. L., Debattista, V. P. & Corsini, E. M. 2003, MNRAS, **338**, 465

Alloin, D., Edmunds, M. G., Lindblad, P. o. & Pagel, B. E. J. 1981, A&A, **101**, 377

Athanassoula, E., Bosma, A. & Papaioannou, S. 1987, A&A, **179**, 23

Barnes, E. I., Sellwood, J. A., 2003, AJ, **125**, 1164

Barnes, E. I., Sellwood, J. A. & Kosowsky, A. 2004, AJ, **128**, 2724

Beck, R., Fletcher, A., Shukurov, A., Snodin, A., Sokoloff, D. D., Ehle, M., Moss, D. & Shoutenkov, V. 2005, A&A, **444**, 739

Bell, E. F. & de Jong, R. 2001, ApJ, **550**, 212

Bell, E. F., McIntosh, D. H., Katz, N. & Weinberg, M. D. 2003, ApJS, **149**, 289

Binney, J. & Merrifield, M. 1998, *Galactic Astronomy*, (Princeton: Princeton University Press)

Binney, J. & Tremaine, S. 1987, *Galactic Dynamics* (Princeton: Princeton University Press)

Bissantz, N., Englmaier, P. & Gerhard, O. 2003, MNRAS, **340**, 949

Boomsma, R, van der Hulst, T., Osterloo, T., Fraternali, F. & Sancisi, R. 2004, in IAU Symposium **217**, eds. P.-A. Duc, J. Braine & E. Brinks (San Francisco: ASP), 142

Bosma, A. 1998, in *Galactic Halos*, ed. D. Zaritsky (San Francisco: ASP) **136**, p. 193

Bottema, R. 1993, A&A, **275**, 16

Bottema, R. 1997, A&A, **328**, 517

Bottema, R., van der Kruit, P. C. & Freeman, K. C. 1987, A&A, **178**, 77

Briggs, D. S. 1995, Ph.D. thesis, New Mexico Institute of Mining and Technology

Bullock, J. S., Kolatt, T. S., Sigad, Y., Somerville, R. S., Kravtsov, A. V., Klypin, A. A., Primack, J. R. & Dekel, A. 2001, MNRAS, **321**, 559

Casertano, S. 1983, MNRAS, **203**, 735

Casertano, S. & van Gorkom, J. H. 1991, AJ, **101**, 1231

Ciardullo, R., Durrell, P. R., Laychak, M. B., Herrmann, K. A., Moody, K., Jacoby, G. H. & Feldmeier, J. J. 2004, ApJ, **614**, 167

Debattista, V. P. & Sellwood, J. A. 2000, ApJ, **543**, 704

Duval, M. F. & Athanassoula, E. 1983, A&A, **121**, 297

de Grijs, R., van der Kruit, P. C. 1996, A&AS, **117**, 19

de Jong, R. S. 1996, A&A, **313**, 377

de Jong, R. S. & Bell, E. F. 2007, "Island Universes – Structure and Evolution of Disk Galaxies", p107 (astro-ph/0604391)

de Vaucouleurs, G., de Vaucouleurs, A., Corwin, H. G., Jr., Buta, R. J., Paturel, G. & Fouque, P. 1991, Volume 1-3, XII (Berlin Heidelberg New York: Springer-Verlag)

Dutton, A. A., van den Bosch, F. C., Dekel, A., Courteau, S. 2007, ApJ, **654**, 27

Edmunds, M. G., Taylor, K. & Turtle, A. J. 1988, MNRAS, **234**, 155

Emsellem, E., Greusard, D., Combes, F., Friedli, D., Leon, S., Pécontal, E.,& Wozniak, H. 2001, A&A, **368**, 52

Englmaier, P. & Gerhard, O. 1997, MNRAS, **287**, 57

Erwin, P. 2004, A&A, **415**, 941

Erwin, P. 2005, MNRAS, **364**, 283

Fuchs, B. 2003, Ap&SS, **284**, 719

Galliano, E., Alloin, D., Pantin, E., Lagage, P. O. & Marco, O. 2005, A&A, **438**, 803

Giovanelli, R., Haynes, M. P., Salzer, J. J., Wegner, G., da Costa, L. N. & Freudling, W. 1994, AJ, **107**, 2036

Giovanelli, R., Haynes, M. P., Herter, T., Vogt, N. P., Wegner, G., Salzer, J. J., da Costa, L. N. & Freudling, W. 1997, AJ, **113**, 22

Gunn, J. E., Knapp, G. R. & Tremaine, S. D. 1979, AJ, **84**, 1181

Helfer, T. T., Thornley, M. D., Regan, M. W., Wong, T., Sheth, K., Vogel, S. N., Blitz, L. & Bock, D. C.-J. 2003, ApJS, **145**, 259

Holwerda, B. W., Gonzalez, R. A., Allen, R. J. & van der Kruit, P. C. 2005, AJ, **129**, 1381

Jörsäter, S., Peterson, C. J., Lindblad, P. O. & Boksenberg, A. 1984, A&AS, **58**, 507

Jörsäter, S., van Moorsel, G. A. 1995, AJ, **110**, 2037

Jungwiert, B. Combes, F. & Axon, D. J. 1997, A&A, **125**, 479

Kamphuis, J. 1993, PhD thesis, University of Groningen

Kamphuis, J. & Sancisi, R. 1993, A&A, **273**, L31

Kranz, T., Slyz, A. & Rix, H.-W. 2003, ApJ, **586**, 143

Kregel, M., van der Kruit, P. C. & de Grijs, R. 2002, MNRAS, **334**, 646

Laine, S., Shlosman, I., Knapen, J. H. & Peletier, R. F. 2002, ApJ, **567**, 97

Lake, G. & Feinswog, L. 1989, AJ, **98**, 166

Landolt, A. U. 1992, AJ, **104**, 340

Lindblad, P. O. 1978,

Lindblad, P. O. 1999, A&A Rev., **9**, 221

Lindblad, P. O., Hjelm, M., Hoegbom, J., Jörsäter, S., Lindblad, P. A. B. & Santos-Lleo, M. 1996, A&AS, **120**, 403

Lindblad, P. A. B., Lindblad, P. O. & Athanassoula, E. 1996, A&A, **313**, 65

McGaugh, S. S. 2005, ApJ, **632**, 859

Madore, B. F., *et al.* 1999, ApJ, **515**, 29

Mathewson, D. S. & Ford, V. L. 1996, ApJS, **107**, 97

Navarro, J. F., Frenk, C. S. & White, S. D. M. 1997, ApJ, 490, 493

Noordermeer, E., van der Hulst, J. M., Sancisi, R., Swaters, R. S. & van Albada, T. S. 2007, MNRAS, to appear (arXiv:astro-ph/0701731)

Osterbrock, D. E. & Martel, A. 1992, PASP, **104**, 76

Palunas, P. & Williams, T. B. 2000, AJ, **120**, 2884

Pérez, I. 2007, A&A, to appear (arXiv:0710.2855)

Pérez, I., Fux, R. & Freeman, K. 2004, A&A, **424**, 799

Phillips, M. M., Edmunds, M. G., Pagel, B. E. J. & Turtle, A. J. 1983, MNRAS, **203**, 759

Pizagno, J., *et al.* 2005, ApJ, **633**, 844

Portinari, L., Sommer-Larsen, J. & Tantalo, R. 2004, MNRAS, **347**, 691

Press, W. H., Flannery, B. P., Teukolsky, S. A. & Vetterling, T. A. 1992, Numerical Recipes (Cambridge: Cambridge Univ. Press)

Roberts, W. W., Huntley J. M. & van Albada G. D. 1979, ApJ, **233**, 67

Sackett, P. D. 1997, ApJ, **483**, 103

Sakai, S., *et al.* 2000, ApJ, **529**, 698

Sakamoto, K., Ho, P. T. P., Mao, R.-Q., Matsushita, S. & Peck, A. B. 2007, ApJ, **654**, 782

Sandqvist, A., Jörsäter, S. & Lindblad, P. O. 1995, A&A, **295**, 585

Schlegel, D. J., Finkbeiner, D. P. & Davis, M. 1998, ApJ, **500**, 525

Sellwood, J. A. 1999, in *Galaxy Dynamics – A Rutgers Symposium*, eds. D. Merritt, J. A. Sellwood & M. Valluri (San Francisco: ASP) **182**, p. 351

Sellwood, J. A. & McGaugh, S. S. 2005, ApJ, **634**, 70

Sellwood, J. A. & Sparke, L. S. 1988, MNRAS, **231**, 25P

Sellwood, J. A. & Wilkinson, A. 1993, *Rep. Prog. Phys.*, **56**, 173

Spergel, D. N., *et al.* 2007, ApJS, **170**, 377

Stark, A. A. & Brand, J. 1989, ApJ, **339**, 763

Strutskie *et al.* 1997, in The impact of Large Scale Near-IR Sky Surveys, ed. F. Garzon *et al.* (Dordrecht:Kluwer), 25

Teuben, P. J., Sanders, R. H., Atherton, P. D. & van Albada, G. D. 1986, MNRAS, **221**, 1

van Albada, G. D. 1985, A&A, **142**, 491

van Albada, T. S., Bahcall, J. N., Begeman, K. & Sancisi, R. 1985, ApJ, **295**, 305

van Moorsel, G. A., Wells, D. C. 1985, AJ, **90**, 1038

Verheijen, M. A. W., Bershady, M. A., Andersen, D. R., Swaters, R. A., Westfall, K., Kelz, A. & Roth, M. M. 2004, Astronomische Nachrichten, **325**, 151

Wakker, B. P. & van Woerden, H. 1997, ARA&A, **35**, 217

Weiner, B. J. 2004, in IAU Symp. 220, Dark Matter in Galaxies, ed. S. Ryder, D. J. Pisano, M. Walker & K. Freeman (Dordrecht: Reidel), 35

Weiner, B. J., Williams, T. B., van Gorkom, J. H. & Sellwood, J. A. 2001, ApJ, **546**, 916

Weiner, B. J., Sellwood, J. A. & Williams, T. B. 2001, ApJ, **546**, 931

Williams, T. B., Caldwell, N. & Schommer, R. A. 1984, ApJ, **281**, 579

Wozniak, H., Friedli, D., Martinet, L., Martin, P. & Bratschi, P. 1995, A&AS, **111**, 115

Chapter 4

Constraining the Mass-to-light of M80 with Fabry-Perot Spectroscopy

It has been more than 30 years since the pioneering work of Gunn & Griffin (1979), hereafter G&G, set the road for a number of subsequent dynamical studies of globular clusters that used high-quality stellar velocities (see Meylan 1993 for a list of references). However, most aspects that involved the modeling of the clusters suffered from large uncertainties, i.e. the amount of dark remnants, the initial mass function, and the luminosity function. Researchers therefore had to rely, for example, on plausible power-law initial mass functions. An important step forward was made with the advent of the Huble Space Telescope (HST). This made possible, among many other things, the construction of luminosity functions from which a present-day main-sequence mass function (PDMF) was derived (Paresce & De Marchi 2000). With this uncertainty possibly out of the picture, one can concentrate on other aspects of the modeling. For example, on the amount of dark remnant stars which, even with HST, are hard to study directly.

In this work we report on the measurement of 543 stellar radial velocities using the Rutgers Fabry-Perot spectrograph in the globular cluster M80. With the aid of HST observations to discard blended stars, we are able to determine the cluster dispersion near the center of the cluster. With our large number of velocities we detect M80's rotation and use them to constrain anisotropic King-Michie dynamical models *à la* G&G but with recent prescriptions for dark remnants and the PDMF. This allows us to estimate the mass-to-light ratio (M/L) and put some limits on the amount of stars lost, possibly through tidal striping.

M80 is a luminous cluster, $M_V = -8.23$ (unless otherwise stated, cluster properties come from the online catalog of Harris 1996)), with a compact, dense core and moderately low metallicity, $[Fe/H] = -1.75$. Located on the sky at $(\ell = 352.67°, b = 19.46°)$, the cluster is currently 3.8 kpc from the center of the Galaxy. Recent ground-based CCD photometry of the cluster stars was presented by Brocato et al. (1998) and by Alcaino et al. (1998). Photometry using HST imaging was presented by Piotto et al. (2002).

Several properties of M80 make it an interesting candidate for study. Its concentration index of 1.95 is among the largest for a cluster that is not classified as having undergone core collapse. The central region hosts both one of the largest populations of blue stragglers ever detected (Ferraro et al. 1999) and a Nova (T Scorpii) that erupted in 1860 A.D. and was recently recovered by Shara & Drissen (1995). The proper motion of the cluster shows that it never gets farther from the center of the Galaxy than about 4 kpc and may pass very close to the Galactic center (Dinescu et al. 1999). As a consequence of this orbit, the predicted destruction rate (*i.e.*, the inverse of the time to complete the disruption of the cluster) is 0.5 per 10 Gyr and may be as high as 40 per 10 Gyr (Dinescu et al. 1999). Thus, M80 is a good candidate for a cluster that has lost a lot of mass due to tidal stripping.

This chapter is organized as follows. Section 2 describes the observations, Sec. 3 presents additional information necessary to derive the M/L, Sec. 4 describes the derivation of the M/L using Michie-King models, Sec. 5 discusses the results of fitting the data with the models, and Sec. 6 is a summary.

4.1 Data

4.1.1 Observations

M80 was observed in the Hα line on the nights of 1995 May 13-14 with the CFHT using the Rutgers Fabry-Perot interferometer with the Sub-arcsecond Imaging Spectrograph. A Loral3 CCD detector was placed at the focal plane and imaged a $3' \times 3'$ field of view. The

CCD was binned 2×2 during readout to obtain 1024×1024 pixels (0.173″ per pixel). Further details of this instrumental can be found in Gebhardt et al. (1997).

We took 15×15 minute exposures stepped by 0.33 Å (15 km/s) across the Hα absorption line. Hourly calibration exposures of Hα and Dα emission lines were taken to correct for temporal drifting of the wavelength zero point and optical axis center. Projector flats were obtained for every wavelength setting of the etalon. The images were reduced with IRAF in the standard fashion: overscan subtraction, bias subtraction and flat-fielding. The seeing varied from 0.8″ to 1.2″. Sky transparency variations occurred throughout the observation. We determined frame-to-frame normalizations by iteratively fitting the spectral line with a Voigt function to the 50 brightest stars in the field. The procedure quickly converged and corrections never exceeded 15%.

4.1.2 Photometry and membership

In Fabry-Perot imaging spectroscopy, a spectrum is reconstructed from individual photometric measurements at different wavelengths of the object of interest. We therefore have measured the brightness of as many stars as possible using DAOPHOT II (Stetson 1987). We used the following procedure to determine the PSF of each frame. We start with the 150 brightest stars and after an initial determination and subtraction of these stars and their neighbors, we inspect the residuals and remove from the lists stars that have pixels with large deviations from the mean (these bad pixels are the result of unsubstracted neighbors or cosmic rays and would contaminate the PSF estimate). The PSF is then recomputed with the cleaned list of bright stars. We experimented with a PSF that was a constant, linear or a quadratic function of the position coordinates x, y and determined that a constant PSF gave the best results for the field of view of interest.

In order to determine if our Fabry-Perot stars are members of M80 and if they are indeed single stars and not two or more unresolved stars, we ideally require photometry from HST in at least two different band passes to construct a color-magnitude diagram,

adequate exposure time for our targeted red giants (i.e. no saturated pixels), and a field of view that contains all of our stars. Unfortunately, there was no single data set that met these criteria and therefore we relied on three different ones: two sets of HST photometry to determine the neighbors of our stars (see §4.1.3), but they needed to be supplemented by ground-based photometry in cases where our stars were saturated in the HST images. These three datasets are described below.

Photometry of stars for M80 in the F555W and F439W filters were presented by Piotto et al. (2002) from HST/WFPC2 observations. We use their published positions and photometry publicly available through the VizieR database (Ochsenbein et al. 2000). These authors aimed at observing the upper parts of the CMD down to just below the main-sequence turnoff. This depth is ideal for us since our Fabry-Perot observations target the bright red giant stars. Unfortunately, we were only able to match 59% of our stars because of the peculiar WFPC2 field of view.

M80 was observed in 2006 February 2 with HST/ACS in filters F555W, F435W and F814W as part of proposal number 10573. We performed simultaneous photometry on the three filters to compensate for bad pixels and cosmic rays with DOLPHOT (Dolphin 2000) and were able to match the positions for the remaining 41% of our stars. Unfortunately, these observations are deeper than those taken with WFPC2 and virtually all the stars in our Fabry-Perot sample have saturated pixels. Nevertheless, DOLPHOT is able to estimate magnitudes and we feel encouraged by how well the upper parts of the CMD are defined (see Fig. 4.1), though with a noticeably large scatter. Since we are aiming at finding bright neighbors of our Fabry-Perot sample, precise photometry is not required since we experiment with three different thresholds (see Section 4.1.3). Therefore, we use this sample to determine neighbors but will determine more reliable magnitudes from a ground-based sample (described below) which has adequate depth. In the end, we rely on HST/ACS magnitudes to determine membership for only 7% of the total sample.

Ground-based multicolor CCD photometry (UBVI) from Las Campanas Observatory

(hereafter LCO) was presented by Alcaino et al. (1998). With a magnitude range of $11.5 < V < 21.5$, this data set is also appropriate to determine the photometry of our Fabry-Perot stars. However, this sample has comparable spatial resolution to ours and therefore can not be used to resolve possible bright neighbors of our stars. We only use this sample to determine the photometry of 33.3% of our stars to determine their membership.

The resulting color-magnitude diagram from the three different samples is presented in Figure 1. Here, stars in common between the three data sets were used to transform (linearly) the HST/ACS F435W and F555W magnitudes and the LCO B and V magnitudes to the instrumental WFPC2 magnitudes in filters F439W and F555W respectively. The FP stars are marked with green, blue or red solid dots when the photometry comes from matches with the WFPC2, LCO or ACS data sets, respectively. Black points are the photometry for all the stars in the HST/ACS and HST/WFPC2 data sets (note their different depths). Stars that lie on unusual places on the CMD have been regarded as non-members of the cluster and are marked with a cross. At least three of those stars had velocities inconsistent with the cluster mean and dispersion. Note that, although we are more tolerant with the ACS matched stars because of their more uncertain magnitudes, we have checked that their velocities are consistent with being members of the cluster. The depth of our Fabry-Perot sample is to about a magnitude of 17.7 in the F555W filter. Two stars in our sample remained unmatched to any of the three data sets either because they were outside of the field of view or because they were eliminated with standard quality checks (sharpness, ellipticity, χ^2). These stars were treated as if they were non-members of the cluster and have been removed from any subsequent analysis.

4.1.3 Neighbors

One big source of concern in ground-based observations of globular clusters is the severe crowding, especially in the inner parts. With insufficient spatial resolution, a star measured from the ground can potentially be two or more closely spaced stars of comparable

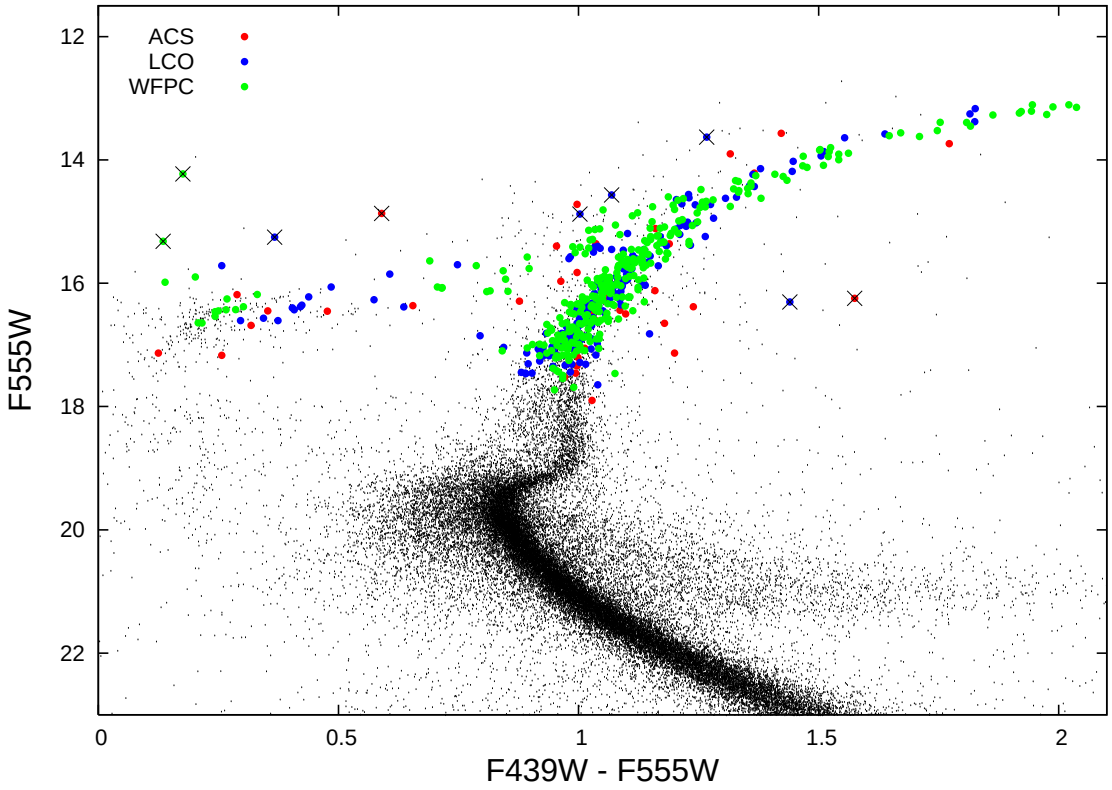

Figure 4.1 CMD of M80. Black dots are both the HST/ACS and HST/WFPC2 magnitudes (note their different depths). Solid points denote our Fabry-Perot stars when the positions were matched against the HST/ACS (red), HST/WFPC2 (green) and LCO (blue) data sets. Stars that we regard as non-members of M80 are marked with a cross.

brightness. The velocity measured for such blended stars would be some average velocity that would bias the velocity dispersion towards being smaller. Fortunately, we can directly evaluate the effects of crowding by matching the positions of the FP stars to those in the HST/WFPC and HST/ACS data sets as was described above.

With the FP stars identified in the list of HST stars, we can readily identify their neighbors. However, it is not obvious at what magnitude threshold a neighbor star should be considered part of the surrounding sky or an "intruding" bright neighbor. If unresolved faint neighbors surround our FP star, they are properly subtracted as sky by DAOPHOT. On the other hand, neighbors of comparable brightness to the star of interest within the DAOPHOT fitting radius can contaminate the measured velocity. Xie (2003) made tests in which velocities were fitted to two stars with different velocities and fluxes. They find

that the dispersion error introduced by the contamination is at the level of 10% to 20% when the flux ratios of the two stars is 0.1 to 0.3. Based on this result we experimented with three different criteria that define a close neighbor as a star within a radius of 0.8″ (the DAOPHOT fitting radius) whose magnitude is at least 1/3rd, 1/5th or 1/8th of the flux of the matched FP star of interest. We then eliminate FP stars that have neighbors according to the above rejection criteria and end up with three different lists of stars plus the original one. After deriving our results using all four lists we find that the rejection criteria of 1/3rd is enough to yield consistent results within the uncertainties except for the dispersion profile (see §4.1.5) in the inner regions where it is still biased to a lower dispersion as expected because of the contamination. Based on these results, we apply our most strict rejection criteria of 1/8th to the inner 25″ (about 3 core radii) and the 1/3rd criteria to the rest of the sample.

4.1.4 Velocities

We fit a Voigt function to the 15 flux observations[1] obtained with DAOPHOT for each star using least-square techniques. The Voigt function has five free parameters: continuum level, line strength, velocity, and the Lorentzian and Gaussian line widths. With a spectral coverage of 5 Å it was hard to fit for the Lorentzian width and we therefore experimented between fixing it to the instrumental Lorentzian width or zero. We adopted the later but the center of the line (velocity) is not affected by our choice. Monte Carlo simulations were constructed to estimate the uncertainty in the velocity measurements. We use the DAOPHOT 1σ uncertainty, assume that the flux errors are normally distributed and generate 5000 realizations of the spectrum for every star. We fit a profile to each spectrum and take the uncertainty to be the standard deviation of the distribution. Stars with uncertainties larger than 8 km s^{-1} (due to poor S/N) were removed from the sample to leave

[1]Strictly speaking we don't always have all 15 fluxes because sometimes a cosmic ray can destroy the photometry of a star at a particular wavelength, but there are still enough measurements to reconstruct the line profile.

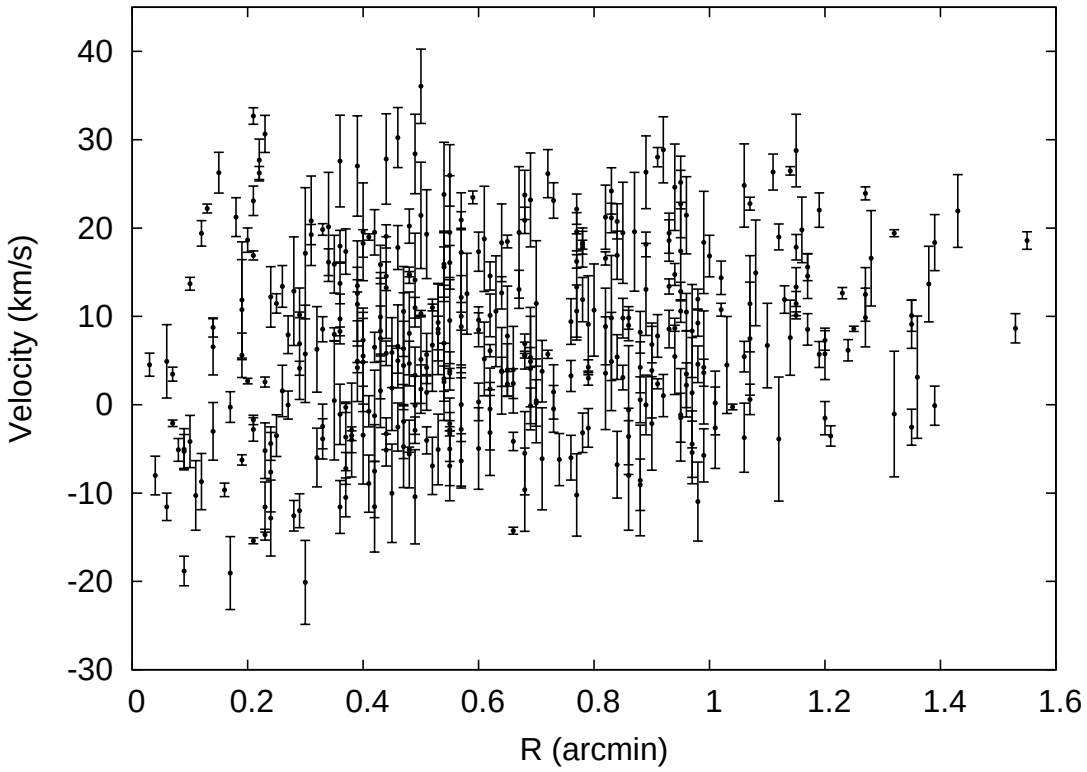

Figure 4.2 Velocity of 388 Fabry-Perot stars as a function of radius from the cluster center.

543, of which 532 are members of M80.

One final necessary cut in our list of stars before it can be used in a dynamical analysis is that due to the field of view of the FP spectrograph. FP frames are not strictly monochromatic since the central wavelength has a radial dependence: $\lambda(r) \propto 1/\sqrt{1+\frac{r^2}{F^2}}$ where r is the radius measured from the optical axis and F is the effective focal length of the FP camera lens. Thus, the spectral coverage of stars at large radii is blueshifted compared to stars near the center and so the velocities of stars are measurable over a wider range when they are more negative than the cluster mean than when they are more positive. To prevent the bias that this would introduce in the velocity dispersion, we have determined the radius out to which we can determine velocities to at least twice the dispersion on both sides of the cluster mean. This reduced the effective field of view to a radius of $1.55'$. Fig. 4.2 is the velocity as a function of radius from the cluster center for the remaining 388 stars. This is the final sample that will be used in the subsequent analysis and modeling.

Data for our sample are presented in Table 4.1. Column 1 is the star id number. Columns 2 and 3 are the offsets in arcminutes (X positive eastward, Y positive northward) from the adopted cluster center: $\alpha = 16^{\rm h}\,17^{\rm m}\,02\overset{\rm s}{.}48$, $\delta = -22^\circ\,58'\,33\overset{''}{.}8$ (J2000.0) from Shara & Drissen (1995). Column 4 is the velocity and its uncertainty. Columns 5 and 6 are the instrumental F555W magnitude and F439W-F555W color, respectively. The last column indicates from what dataset the photometry was derived followed by a note to indicate when: *, the star was flagged as a non-member of M80; r, the star was at a large radius and would bias the dispersion; 3, 5 or 8, the star has at least one neighbor with a flux of at least 1/3rd, 1/5th or 1/8th of its flux, respectively (see §4.1.3).

4.1.5 Velocity dispersion and rotation

We have estimated the velocity dispersion with a maximum likelihood technique (Pryor & Meylan 1993) that takes into account the contribution from measurement uncertainties. We find the mean velocity and dispersion for the entire sample of 388 stars to be 7.39 ± 0.54 km s^{-1} and 10.1 ± 0.4 km s^{-1} respectively. This is in very good agreement with previous studies, see Pryor & Meylan (1993) and Harris (1996).

Table 4.2 is a dispersion profile constructed for 10 radial bins, each one containing 39 stars (the last bin has 37 stars). Column 1 is the radial range for the bin and column 2 is the mean radius for the stars in that bin. Column 3 is the velocity dispersion and its uncertainty estimated with the maximum likelihood estimator. The velocity dispersion seems to be decreasing with radius as expected. The difference in the dispersion between the inner- and outer-most bins is about 2.6 times its uncertainty.

Globular clusters are nearly spherical systems (Frenk & Fall 1982; White & Shawl 1987) and should have a net rotation much smaller than the dispersion. The small observed ellipticities are believed to be driven by internal rotation rather than by tidal interaction with the galaxy (White & Shawl 1987). Detecting rotation is a challenging process that requires a large number of velocity measurements. To look for rotation, we divide the cluster

Table 4.1. Radial Velocity Data

Star	X (′)	Y (′)	Velocity km s^{-1}	V	B-V	Notes	Star	X (′)	Y (′)	Velocity km s^{-1}	V	B-V	Notes
1	0.77	0.17	3.01 ± 0.77	13.15	2.04	WFPC	2	0.39	0.28	-5.09 ± 0.29	13.11	1.95	WFPC
3	0.45	1.08	9.58 ± 0.35	13.26	1.98	WFPC,r	4	0.31	−1.21	8.59 ± 0.29	13.14	1.99	WFPC
5	1.15	0.06	10.11 ± 0.40	13.11	2.02	WFPC	7	0.20	0.01	2.68 ± 0.32	13.24	1.92	WFPC
8	0.54	−0.12	-2.14 ± 0.34	13.17	1.83	LCO,8	9	−0.42	−0.24	14.78 ± 0.30	13.25	1.82	LCO
10	0.16	−0.14	-15.40 ± 0.34	13.21	1.92	WFPC	11	0.43	−0.34	-3.24 ± 0.30	13.21	1.94	WFPC
12	−0.04	0.05	3.46 ± 0.79	13.27	1.86	WFPC	13	0.03	0.29	10.18 ± 0.32	13.38	1.82	LCO
15	0.19	−0.02	8.62 ± 0.42	13.39	1.75	WFPC,5	16	0.96	−0.39	-0.25 ± 0.32	13.39	1.81	WFPC
17	−0.07	−0.01	-2.10 ± 0.37	13.45	1.82	WFPC	18	0.09	−1.27	23.93 ± 0.75	13.53	1.75	WFPC
19	0.69	0.64	8.66 ± 0.34	13.61	1.65	WFPC	20	0.54	−1.20	19.42 ± 0.40	13.56	1.67	WFPC
21	−0.39	0.12	18.99 ± 0.36	13.58	1.64	LCO	22	−1.58	−0.59	1.90 ± 0.49	13.64	1.55	LCO,r
23	0.18	−0.64	-14.26 ± 0.41	13.62	1.71	WFPC	24	0.76	0.85	26.47 ± 0.48	13.87	1.52	WFPC
25	−0.34	0.59	5.67 ± 0.38	13.57	1.42	ACS,5	26	0.45	0.20	10.31 ± 0.36	13.80	1.53	WFPC
27	0.13	0.14	-5.16 ± 0.49	13.84	1.50	WFPC,3	28	−0.49	0.19	11.00 ± 0.39	13.87	1.51	LCO
29	−0.65	−0.97	-15.31 ± 0.55	13.63	1.27	LCO,*	30	0.71	−0.13	5.71 ± 0.46	13.83	1.50	WFPC
31	−0.03	−0.06	-1.45 ± 0.56	13.94	1.47	WFPC,8	33	−0.29	−0.86	2.37 ± 0.57	13.91	1.54	WFPC,8
34	0.69	−0.37	18.12 ± 0.51	13.89	1.56	WFPC	35	−0.21	−0.30	8.30 ± 0.51	13.94	1.51	LCO
36	−0.10	−0.08	22.21 ± 0.50	13.95	1.52	WFPC	37	0.14	−0.16	-1.72 ± 0.54	14.09	1.51	WFPC
38	−1.50	0.50	10.00 ± 1.02	14.14	1.38	LCO,r	39	−0.58	−0.97	16.34 ± 0.51	14.02	1.45	LCO,3
40	−1.08	0.59	12.63 ± 0.65	14.24	1.36	LCO,8	41	−0.13	0.19	-14.71 ± 0.61	13.74	1.77	ACS
42	−0.26	0.03	0.76 ± 0.55	14.26	1.37	WFPC,8	43	−0.16	−0.09	-6.25 ± 0.58	14.00	1.54	WFPC
44	−0.17	−0.35	-3.50 ± 0.55	13.90	1.32	ACS	45	−0.05	−0.02	-7.92 ± 0.84	14.34	1.33	WFPC,8
46	−0.07	−0.11	-0.31 ± 0.76	14.38	1.36	WFPC,3	47	0.01	0.21	16.90 ± 0.51	14.12	1.48	WFPC
48	0.46	−0.63	4.24 ± 0.85	14.10	1.47	WFPC	49	0.51	0.22	3.55 ± 0.56	14.27	1.43	WFPC
50	0.12	−0.26	10.83 ± 0.56	14.19	1.45	LCO	51	−0.12	−0.19	2.57 ± 0.56	14.23	1.41	WFPC
52	−0.22	−0.13	7.12 ± 0.59	14.21	1.37	ACS,3	53	0.36	−0.07	-0.29 ± 0.59	14.35	1.33	WFPC
54	0.04	0.03	6.47 ± 0.85	14.73	1.20	WFPC,3	55	0.13	0.37	4.20 ± 0.59	14.33	1.43	WFPC
56	−1.54	−0.13	18.59 ± 1.03	14.62	1.31	LCO	57	0.32	0.06	19.84 ± 0.65	14.47	1.32	WFPC
58	−0.82	0.38	28.03 ± 1.09	14.43	1.37	LCO	59	−0.89	−0.59	22.77 ± 0.73	14.42	1.36	LCO
60	0.02	0.10	13.70 ± 0.73	14.43	1.36	WFPC	61	−0.02	0.16	15.13 ± 0.81	14.60	1.19	WFPC,8
62	−0.00	−0.04	18.84 ± 1.00	15.19	1.21	WFPC,3	63	−1.26	0.10	6.67 ± 0.70	14.57	1.07	LCO,*
64	0.13	0.63	18.48 ± 0.73	14.48	1.25	WFPC	65	−0.03	−0.22	26.23 ± 0.74	14.46	1.35	WFPC
66	0.36	1.21	7.70 ± 1.02	14.65	1.21	WFPC,r	67	−0.04	−0.00	-6.47 ± 1.57	14.75	1.32	WFPC,5
68	0.13	0.13	1.92 ± 0.94	14.55	1.35	WFPC,3	69	−0.59	0.04	-8.91 ± 0.74	14.56	1.23	LCO,3
70	−0.24	0.40	12.68 ± 0.78	14.60	1.33	LCO,3	71	0.14	0.05	15.09 ± 0.83	14.69	1.26	WFPC,5
72	−0.68	0.45	16.56 ± 0.75	14.62	1.23	LCO,5	73	0.32	−0.50	23.48 ± 0.72	14.65	1.28	WFPC
74	0.10	−0.17	18.64 ± 1.37	14.53	1.33	WFPC	75	−0.21	−0.58	1.79 ± 0.75	14.50	1.33	WFPC
76	0.46	0.62	16.23 ± 0.76	14.76	1.26	WFPC	77	0.01	0.16	-9.64 ± 0.78	14.67	1.27	WFPC
78	0.01	0.01	-2.81 ± 1.29	15.09	1.18	WFPC,3	79	−0.05	−0.04	12.83 ± 1.77	15.30	1.02	WFPC,3
80	−0.06	−0.61	6.12 ± 0.70	14.62	1.38	WFPC	81	−0.32	−0.14	7.97 ± 0.75	14.72	1.27	LCO
82	−0.26	0.78	20.04 ± 0.70	14.64	1.20	LCO,3	83	0.21	0.33	13.46 ± 0.70	14.73	1.24	LCO
84	0.01	−0.29	4.13 ± 0.81	14.63	1.22	WFPC	85	0.18	−0.08	-5.47 ± 1.01	15.31	1.14	WFPC,3
86	0.02	−0.33	-1.07 ± 0.84	14.71	1.21	LCO,3	87	0.80	−0.64	10.76 ± 0.73	14.77	1.25	WFPC
88	−0.03	−0.02	10.45 ± 2.31	16.56	0.96	WFPC,3	89	−0.09	−0.02	-18.82 ± 1.73	14.86	1.25	WFPC
90	1.09	0.68	16.43 ± 2.52	15.06	1.08	WFPC,r	91	0.85	−0.38	13.39 ± 0.86	14.80	1.20	WFPC
92	−0.01	−0.25	11.47 ± 1.10	14.76	1.15	WFPC	93	0.26	0.51	20.91 ± 0.93	15.01	1.25	WFPC
94	0.29	−0.14	5.02 ± 2.18	15.40	0.95	ACS,3	95	0.03	−0.07	13.41 ± 1.29	14.99	1.21	WFPC,3
96	1.19	−0.93	0.69 ± 1.81	15.06	1.24	WFPC,r	98	0.02	−0.14	8.75 ± 1.09	14.81	1.05	WFPC
99	−0.12	0.04	3.12 ± 1.26	14.91	1.11	WFPC,8	100	−0.13	0.28	11.29 ± 0.90	14.95	1.28	LCO,3
101	0.03	0.02	4.53 ± 1.31	15.13	1.03	WFPC	102	0.04	0.05	-11.56 ± 1.54	15.00	1.15	WFPC
103	−0.38	0.73	11.09 ± 0.92	15.04	1.22	LCO,3	104	−0.91	0.28	12.81 ± 1.05	15.08	1.22	LCO
105	−0.41	0.24	14.66 ± 0.92	15.02	1.24	LCO,5	106	−0.30	0.62	5.36 ± 1.10	15.01	1.23	LCO
107	0.57	1.08	-1.09 ± 1.29	15.34	1.17	WFPC,r	108	−0.18	−0.11	32.68 ± 0.94	14.86	1.12	WFPC
110	−0.23	0.50	12.32 ± 0.90	15.06	1.21	LCO,3	111	−0.45	−0.49	-4.15 ± 1.04	15.03	1.21	LCO
112	1.23	−0.17	6.16 ± 1.22	15.21	1.09	WFPC	113	−1.45	0.29	-114.84 ± 1.26	14.88	1.00	LCO,*

Table 4.1 (cont'd)

Star	X (′)	Y (′)	Velocity km s^{-1}	V	B-V	Notes	Star	X (′)	Y (′)	Velocity km s^{-1}	V	B-V	Notes
114	0.48	0.10	10.98 ± 1.17	15.11	1.17	WFPC	115	0.43	−0.78	18.66 ± 1.64	14.23	0.18	WFPC,*
116	−0.05	−0.21	-2.79 ± 1.34	14.97	1.22	WFPC	117	−0.07	0.02	-5.11 ± 1.32	15.11	1.15	WFPC
119	−0.18	0.25	19.26 ± 1.15	15.24	1.26	LCO	120	0.03	0.68	6.90 ± 1.12	15.12	1.04	WFPC
121	−0.09	0.98	11.96 ± 1.12	15.13	1.20	WFPC	122	0.96	−0.67	15.58 ± 1.55	15.12	1.16	ACS,5
123	0.09	−0.23	12.16 ± 1.44	15.23	1.19	WFPC,8	124	−1.11	−0.44	7.28 ± 1.12	15.12	1.20	LCO
126	−1.20	−0.20	-3.53 ± 1.16	15.21	1.21	LCO	127	−0.02	0.06	24.69 ± 1.44	15.23	1.16	WFPC,8
128	0.07	−0.06	-7.81 ± 1.21	15.19	1.19	WFPC,5	129	−0.09	−0.10	6.87 ± 1.44	15.60	1.11	WFPC,3
130	0.53	−0.16	15.49 ± 1.07	15.24	1.17	LCO,3	131	−0.02	−0.04	-8.01 ± 2.21	15.41	0.99	WFPC
132	0.20	0.05	17.39 ± 1.24	15.24	1.15	WFPC,5	133	0.06	−0.10	3.88 ± 1.38	15.29	1.15	WFPC,8
134	−0.86	−0.36	14.75 ± 1.24	15.19	1.10	LCO	137	0.16	0.01	18.19 ± 1.26	15.71	1.08	WFPC,3
138	0.14	0.17	26.00 ± 1.24	15.34	1.14	WFPC,5	139	−1.53	0.07	8.66 ± 1.68	15.40	1.04	LCO
140	0.94	0.17	10.60 ± 1.29	15.41	1.00	WFPC	141	−0.91	0.71	11.45 ± 1.37	15.34	1.17	LCO
142	−0.12	0.16	-11.67 ± 1.93	15.45	1.11	WFPC,3	143	0.39	−0.11	4.24 ± 1.43	15.33	1.18	WFPC,3
144	−0.03	−0.28	-4.06 ± 1.40	15.90	1.08	WFPC,3	145	0.04	−0.16	-0.27 ± 1.73	15.51	0.99	WFPC
146	0.32	0.16	12.03 ± 1.24	15.61	1.18	WFPC,5	147	−0.02	0.01	8.77 ± 2.15	15.71	0.79	WFPC,3
148	0.05	0.28	-12.57 ± 1.78	15.34	1.18	WFPC	149	0.84	0.27	18.15 ± 1.37	15.43	1.02	WFPC
150	0.01	0.18	-12.50 ± 1.60	15.53	1.14	WFPC,8	151	1.37	0.37	-1.27 ± 2.61	15.58	1.08	WFPC,r
152	1.09	−0.29	18.99 ± 1.47	15.53	1.13	WFPC	153	−0.27	−0.27	25.36 ± 1.21	15.38	1.23	LCO,3
154	0.40	0.18	-5.13 ± 1.87	15.29	1.03	WFPC	155	−0.29	−0.25	-3.97 ± 1.45	15.39	1.18	LCO
156	0.27	0.00	-0.04 ± 1.57	15.46	1.12	WFPC	157	0.29	0.00	0.98 ± 1.54	15.48	1.17	WFPC,8
158	−0.09	−0.43	19.06 ± 1.33	15.32	1.23	WFPC	159	−0.70	−0.50	9.82 ± 1.29	15.36	1.19	ACS
160	−0.41	−0.17	5.83 ± 1.39	15.46	1.14	LCO	161	−1.14	0.14	17.83 ± 1.46	15.56	1.15	LCO,8
162	−0.98	−0.56	11.90 ± 1.60	15.42	1.03	LCO	163	0.28	−0.18	3.39 ± 1.30	15.45	1.14	WFPC,8
164	0.05	0.07	-5.29 ± 1.98	15.14	1.02	WFPC	165	−0.18	−0.62	2.34 ± 1.41	15.37	1.23	WFPC
166	−0.91	−0.33	11.18 ± 1.69	15.43	1.04	LCO,3	167	−1.15	−0.70	-23.99 ± 1.95	15.46	1.09	LCO,3
168	−0.68	−0.50	3.08 ± 1.41	15.36	1.04	ACS	169	−1.06	0.13	5.45 ± 1.72	15.49	1.03	LCO
170	−0.41	−0.11	12.97 ± 1.57	16.18	0.29	ACS,3	171	0.36	0.40	2.95 ± 1.42	15.52	1.01	WFPC
172	0.01	0.11	4.64 ± 2.03	16.00	1.06	WFPC,3	173	−0.11	0.10	3.37 ± 1.51	15.45	1.07	LCO,3
174	−0.09	−0.01	-1.34 ± 4.24	16.22	1.04	WFPC,3	175	0.49	0.06	-2.88 ± 1.49	15.70	1.10	WFPC,5
176	−0.12	−0.01	19.40 ± 1.47	15.22	1.17	WFPC	177	0.81	−0.85	8.53 ± 1.79	15.66	1.10	WFPC
178	0.14	0.15	11.00 ± 1.54	15.68	1.10	WFPC,3	179	−0.33	−0.01	17.83 ± 2.15	14.87	0.59	ACS,*
180	0.31	0.12	8.55 ± 1.46	15.60	1.12	LCO	181	0.30	0.22	2.68 ± 1.54	···	···	–,*
182	0.38	0.29	-5.58 ± 3.97	15.61	1.13	WFPC	183	0.09	−0.03	12.86 ± 2.07	15.89	1.11	WFPC,3
184	0.29	0.94	3.62 ± 1.54	15.63	1.11	WFPC	185	−0.65	0.49	12.83 ± 1.85	15.67	1.11	LCO,3
186	−0.43	−1.11	5.69 ± 1.48	15.57	0.98	LCO,5	187	0.15	0.76	18.35 ± 1.31	15.64	1.10	WFPC
188	0.18	1.14	13.33 ± 2.23	15.83	1.08	WFPC	189	0.46	−0.42	14.58 ± 1.58	15.52	1.19	WFPC
190	−0.31	−0.51	9.60 ± 1.48	15.53	1.14	LCO	191	−0.34	−0.60	20.87 ± 1.49	15.52	1.13	WFPC
192	0.87	−1.04	10.09 ± 1.81	15.75	1.11	WFPC	193	0.88	−0.44	9.24 ± 1.51	15.67	1.12	WFPC
194	0.07	−0.40	13.99 ± 1.59	15.75	1.13	WFPC,3	195	−0.10	0.32	16.14 ± 1.49	15.55	1.11	LCO
197	−0.32	0.33	18.06 ± 1.73	16.38	1.24	ACS,3	198	−0.13	−0.20	14.62 ± 1.62	16.25	1.58	ACS,*,3
199	0.22	−0.46	-4.04 ± 1.54	15.62	1.10	WFPC	200	0.05	−0.20	23.08 ± 1.66	15.39	1.16	WFPC
201	−0.42	0.05	6.50 ± 1.70	15.64	1.13	LCO,5	202	−0.04	−0.83	21.14 ± 1.68	15.51	1.18	WFPC
203	−0.62	−0.27	5.56 ± 1.52	15.66	1.14	LCO	204	0.04	0.44	14.55 ± 1.63	15.60	0.98	LCO
205	0.36	0.29	17.79 ± 2.55	15.88	1.12	WFPC	206	0.13	−0.20	-4.40 ± 1.90	15.58	0.89	WFPC
207	−0.17	−0.31	17.95 ± 1.83	15.83	1.00	ACS	208	0.41	0.22	4.98 ± 1.42	15.68	1.15	WFPC
209	−0.98	0.52	26.34 ± 2.04	15.85	1.10	LCO,8	210	0.25	−0.52	10.00 ± 1.60	15.63	1.09	WFPC
211	−0.07	−0.66	2.39 ± 1.69	15.63	1.13	WFPC	212	−0.09	0.04	-4.17 ± 3.04	15.72	1.08	WFPC
213	−1.01	0.61	22.03 ± 1.92	15.96	1.10	LCO	214	−0.65	1.00	9.02 ± 2.37	15.90	1.08	LCO,3
215	1.23	0.35	12.72 ± 2.95	15.95	1.02	WFPC,r	216	0.03	−0.09	-5.04 ± 2.33	15.53	1.09	WFPC
217	1.01	−0.13	14.37 ± 1.90	15.92	1.14	WFPC	218	−0.92	0.18	5.49 ± 1.73	15.77	1.11	LCO,3
219	−0.63	0.09	3.73 ± 1.67	15.77	1.09	LCO,8	220	−0.15	−0.17	-8.19 ± 2.39	15.70	0.75	LCO,3
221	0.23	−0.01	-11.58 ± 2.86	15.80	0.84	WFPC	222	−0.08	−0.39	18.26 ± 1.56	15.72	1.17	LCO
223	0.02	−0.02	6.50 ± 3.81	17.10	0.84	WFPC,3	224	0.33	−0.29	-3.28 ± 1.82	15.76	1.11	WFPC
225	0.45	−0.16	20.22 ± 1.95	15.76	1.11	WFPC	226	0.06	0.05	16.00 ± 2.52	15.75	1.08	WFPC,3

Table 4.1 (cont'd)

Star	X (′)	Y (′)	Velocity km s^{-1}	V	B-V	Notes	Star	X (′)	Y (′)	Velocity km s^{-1}	V	B-V	Notes
227	0.18	0.01	-15.71 ± 5.05	15.96	1.06	WFPC,5	228	−0.05	0.77	22.14 ± 1.75	15.93	1.04	WFPC
229	−0.86	0.64	0.60 ± 1.73	15.86	1.11	LCO	230	0.18	0.74	3.26 ± 1.78	15.91	1.05	WFPC
231	−0.05	−0.10	12.43 ± 2.21	16.01	1.06	WFPC,3	232	1.44	−0.18	6.58 ± 4.76	16.15	1.07	WFPC,r
234	−1.33	0.27	9.11 ± 2.80	16.08	1.06	LCO	235	0.13	−0.49	4.22 ± 1.85	15.73	1.10	WFPC
236	0.36	−1.15	-1.52 ± 1.88	15.68	1.13	WFPC	237	−0.86	0.02	8.97 ± 1.75	15.94	1.10	LCO
238	−1.25	−0.61	-0.11 ± 2.24	15.99	1.09	LCO	240	−0.06	−0.52	8.12 ± 1.89	15.71	1.14	WFPC
241	−0.10	−0.22	-2.79 ± 2.54	16.53	1.02	WFPC,3	242	−0.23	0.06	-3.75 ± 2.67	15.32	0.13	WFPC,*,8
243	0.27	−0.10	-11.99 ± 1.94	15.76	0.90	WFPC	244	0.01	0.03	7.86 ± 3.40	16.17	1.07	WFPC,8
245	0.23	0.90	8.57 ± 2.16	16.09	1.06	WFPC	246	0.75	0.94	11.03 ± 3.80	16.23	1.10	WFPC,r
247	0.66	1.05	12.37 ± 4.54	16.23	1.08	WFPC,r	248	0.51	0.07	1.38 ± 2.04	16.02	1.05	WFPC
249	−0.68	−0.91	-21.56 ± 3.58	16.30	1.44	LCO,*	250	−1.08	0.46	14.55 ± 2.56	16.13	1.07	LCO
251	0.86	0.51	16.83 ± 2.35	16.07	1.05	WFPC	252	0.44	0.51	13.06 ± 2.16	15.94	0.85	WFPC
253	0.85	−0.02	9.80 ± 2.24	16.04	1.09	WFPC	254	−0.54	0.64	20.76 ± 2.01	15.98	1.05	LCO
256	1.21	−0.63	8.30 ± 3.68	16.22	1.09	WFPC,r	257	−0.36	0.32	4.66 ± 2.55	15.95	1.09	LCO
258	−0.95	−0.24	4.58 ± 2.06	15.96	1.09	LCO	259	−1.11	0.87	15.76 ± 3.88	15.25	0.37	LCO,*,r
260	−0.13	−0.08	26.27 ± 2.35	15.90	1.06	WFPC	261	−0.60	0.22	12.66 ± 1.84	15.99	1.09	LCO
262	0.06	−0.04	0.94 ± 3.22	15.78	1.06	WFPC,3	263	−0.33	0.24	-0.74 ± 1.77	16.03	1.08	LCO
265	0.09	0.37	12.52 ± 2.37	16.22	1.05	ACS,3	266	0.11	0.04	21.36 ± 3.61	16.00	1.07	WFPC,3
267	0.60	0.07	8.48 ± 1.95	16.03	1.03	WFPC	269	−0.17	−0.36	8.21 ± 2.56	16.60	1.04	ACS,3
270	0.74	1.02	1.12 ± 4.59	16.37	1.10	WFPC,r	271	0.17	−0.24	9.15 ± 2.80	16.02	1.04	LCO
272	0.16	−0.33	-10.49 ± 2.26	16.05	1.06	WFPC	273	−0.14	0.26	24.95 ± 2.32	16.03	1.14	LCO,5
274	0.51	0.53	23.12 ± 2.05	16.16	1.05	WFPC	275	−0.73	0.27	-3.17 ± 2.24	16.03	1.07	LCO
276	0.65	−0.45	-2.63 ± 2.23	16.03	1.07	WFPC	277	−0.26	0.01	2.77 ± 3.30	16.36	1.04	WFPC,3
278	0.16	−0.36	7.30 ± 2.49	15.92	1.10	WFPC	279	−0.43	−0.27	5.67 ± 2.43	16.02	1.13	LCO
280	0.32	0.09	-3.86 ± 2.29	16.14	1.07	WFPC	281	0.27	−0.07	7.92 ± 2.19	16.00	1.08	WFPC
282	−0.78	−0.04	17.79 ± 2.28	16.04	1.09	LCO,8	283	0.01	−0.06	4.91 ± 4.40	15.64	0.69	WFPC
284	0.30	−0.14	-8.01 ± 1.13	14.72	1.00	ACS,3	285	−0.33	0.87	19.42 ± 2.29	16.05	1.07	LCO
286	0.12	−0.18	4.51 ± 1.99	16.00	1.06	WFPC,8	287	−0.24	−0.87	7.79 ± 2.46	15.95	1.13	WFPC
288	0.68	0.36	19.58 ± 2.16	16.21	1.03	WFPC	289	−0.43	−0.03	15.87 ± 2.19	16.02	1.08	LCO
290	0.45	0.31	16.09 ± 1.96	16.22	1.05	WFPC	291	−0.11	−0.30	-7.90 ± 3.07	16.44	1.09	ACS,3
292	0.14	0.95	2.21 ± 2.58	16.10	1.06	WFPC	293	0.49	0.35	17.32 ± 2.23	16.16	1.05	WFPC
295	−0.12	−0.09	-1.21 ± 2.40	16.06	1.03	WFPC,3	297	−0.13	−0.06	10.89 ± 2.85	16.13	1.06	WFPC,8
298	0.79	−0.39	8.21 ± 2.35	16.22	1.11	WFPC	299	0.15	−0.28	5.25 ± 2.28	15.98	1.06	WFPC,8
300	−0.46	−0.38	0.33 ± 2.13	16.06	1.09	LCO	301	0.23	0.11	-3.50 ± 2.38	16.09	1.07	WFPC
302	−0.29	0.77	24.20 ± 2.69	16.10	1.05	LCO	303	0.11	−0.13	21.23 ± 2.28	15.88	1.05	WFPC
304	−0.21	0.10	30.65 ± 2.14	15.96	1.04	WFPC	305	−0.20	0.94	10.49 ± 2.12	16.06	1.07	LCO
306	−0.17	−0.08	14.22 ± 3.26	16.09	1.06	WFPC,8	307	−0.12	−0.35	-7.21 ± 1.78	16.14	1.07	LCO
308	−0.21	−0.91	18.59 ± 2.43	16.05	1.06	WFPC	309	0.23	0.28	13.73 ± 2.35	16.13	0.85	WFPC
310	−0.30	−0.46	3.82 ± 2.19	16.29	0.88	ACS	311	−0.59	−0.48	-6.00 ± 2.54	16.13	1.09	LCO
313	0.72	0.63	25.16 ± 3.13	16.47	0.98	WFPC	314	−0.11	0.16	16.76 ± 4.02	16.04	1.05	WFPC,3
315	−1.30	−0.39	-2.54 ± 2.12	16.17	1.08	LCO	316	0.65	−0.24	-0.13 ± 2.01	16.25	1.07	LCO,5
317	0.19	0.12	27.70 ± 2.42	16.02	1.08	WFPC	318	0.97	−0.71	5.76 ± 2.93	16.36	1.01	LCO
319	−0.54	0.45	0.20 ± 2.66	16.16	1.03	LCO	320	0.71	0.16	-0.47 ± 2.73	16.12	0.82	WFPC
321	−0.46	0.51	23.75 ± 2.79	16.20	1.03	LCO	322	−0.36	0.05	17.34 ± 2.64	15.97	0.96	ACS
323	−1.24	−0.27	9.87 ± 3.44	16.37	1.04	LCO	324	−0.42	0.64	10.60 ± 2.99	16.27	1.09	LCO,8
325	0.24	0.22	-2.46 ± 2.55	16.23	1.10	WFPC	326	−0.93	−1.03	18.35 ± 3.30	16.33	1.03	LCO
327	−0.05	0.13	11.00 ± 3.84	16.34	1.00	WFPC,3	328	−0.42	−0.63	9.42 ± 2.66	16.11	1.12	WFPC
329	−0.02	−0.10	17.68 ± 3.47	16.46	1.04	WFPC,3	330	−0.06	0.25	13.39 ± 2.38	16.07	1.12	WFPC
331	0.27	0.14	-20.11 ± 5.18	16.14	0.81	WFPC	332	0.15	−0.11	5.60 ± 2.56	16.30	1.04	WFPC
333	0.99	0.09	-5.74 ± 3.10	16.33	1.06	WFPC	334	−0.19	0.02	9.44 ± 3.09	16.65	1.03	WFPC,3
335	0.77	−1.01	12.48 ± 3.11	16.36	1.04	WFPC	336	−0.38	−0.16	-8.93 ± 3.38	16.45	1.05	LCO
337	−0.36	1.11	19.80 ± 4.17	16.33	1.03	LCO	338	−0.12	−0.03	-8.70 ± 3.35	16.22	1.01	WFPC
339	−0.11	0.83	16.92 ± 2.81	16.29	1.01	WFPC	340	0.51	−0.67	5.40 ± 2.54	16.49	1.06	WFPC,5
341	0.08	−0.11	6.56 ± 3.39	16.12	1.16	ACS	342	0.35	−0.52	10.11 ± 2.47	16.26	1.02	WFPC

Table 4.1 (cont'd)

Star	X (′)	Y (′)	Velocity km s^{-1}	V	B-V	Notes	Star	X (′)	Y (′)	Velocity km s^{-1}	V	B-V	Notes
343	0.41	0.15	8.35 ± 2.85	16.24	1.04	WFPC	344	0.36	−0.01	-11.58 ± 3.03	16.45	1.11	WFPC
346	0.08	0.16	18.64 ± 5.15	16.65	0.22	WFPC,8	347	0.16	0.25	17.14 ± 7.80	16.06	0.71	WFPC
348	−0.05	0.46	-2.52 ± 2.72	16.35	1.09	LCO	349	−0.47	0.87	15.78 ± 3.35	15.85	0.61	LCO,3
350	−0.17	0.16	-5.20 ± 3.29	16.35	1.03	WFPC	351	0.26	0.25	-1.09 ± 3.52	16.58	1.03	WFPC
352	−0.87	−0.33	1.03 ± 2.44	16.38	1.04	LCO	353	0.49	−0.11	1.76 ± 2.79	16.33	1.00	WFPC
354	−0.27	−0.31	19.51 ± 2.59	16.43	1.04	LCO	356	−0.61	1.10	6.38 ± 3.61	16.58	1.00	LCO,r
357	−0.16	−0.01	4.53 ± 3.64	16.36	0.98	WFPC,3	358	−0.21	−1.04	-3.73 ± 3.94	16.36	1.07	WFPC
359	0.35	0.03	15.91 ± 3.33	16.39	1.03	WFPC	360	0.15	0.09	-19.06 ± 4.59	16.39	1.01	WFPC
361	0.42	0.58	26.16 ± 2.77	16.53	1.01	WFPC	362	1.08	0.59	3.12 ± 5.42	16.62	1.04	WFPC,r
363	−0.33	0.82	-0.02 ± 3.46	16.44	1.02	ACS	364	0.46	0.00	30.24 ± 3.48	16.42	1.02	LCO
365	0.13	0.03	-3.01 ± 3.45	16.34	0.98	WFPC	367	−0.47	0.14	-0.07 ± 3.41	16.41	1.00	LCO
370	0.49	0.28	-6.36 ± 3.11	16.48	0.98	WFPC	371	0.89	0.05	26.32 ± 4.26	16.07	0.72	WFPC
372	0.23	0.87	6.81 ± 2.10	16.50	0.99	WFPC	374	−0.28	0.40	3.33 ± 3.25	16.44	1.02	LCO
375	−0.14	−0.34	9.71 ± 2.91	16.55	1.03	LCO	376	−0.67	0.61	0.74 ± 5.28	15.72	0.26	LCO,3
378	−0.23	−0.08	4.29 ± 3.27	16.28	1.05	LCO,3	379	−0.08	−0.36	-3.66 ± 4.12	16.49	0.99	LCO
380	0.34	0.95	0.20 ± 3.63	16.51	1.02	WFPC	383	0.04	1.18	16.96 ± 5.74	16.75	1.00	LCO,r
385	−1.41	−0.24	21.94 ± 4.51	16.62	1.03	LCO	387	0.69	−0.68	-5.40 ± 3.66	16.45	1.04	WFPC
388	−0.65	−0.08	3.95 ± 3.03	16.49	1.06	LCO	389	−0.43	0.97	24.82 ± 5.33	16.68	1.00	LCO
391	0.01	0.09	10.94 ± 2.78	16.15	1.05	WFPC,8	393	−0.38	−0.36	-6.92 ± 3.32	16.65	1.18	ACS
394	−0.20	−0.20	8.62 ± 3.52	16.50	1.10	ACS,8	395	−0.23	−0.92	-1.47 ± 2.86	16.34	1.07	WFPC
397	−0.05	−0.23	-7.63 ± 5.12	16.43	1.03	WFPC	401	0.28	0.65	3.79 ± 3.50	16.66	1.00	WFPC
402	−0.30	0.10	-5.98 ± 3.42	16.58	1.02	LCO	403	−0.91	0.26	22.72 ± 3.87	16.68	1.00	LCO
404	0.16	−0.07	15.31 ± 4.21	16.64	0.98	WFPC,8	406	−0.25	0.85	4.24 ± 2.97	16.64	1.02	LCO
407	0.23	−0.05	12.21 ± 3.57	16.46	1.00	WFPC	408	0.17	0.14	8.04 ± 4.36	16.93	0.95	WFPC,3
409	0.93	−0.39	-2.61 ± 4.93	16.91	1.04	WFPC	410	−0.97	0.83	16.58 ± 7.52	16.06	0.48	LCO
411	0.04	0.26	15.40 ± 4.22	16.60	1.05	WFPC,8	412	−0.10	0.03	-4.11 ± 1.90	16.97	0.99	WFPC,3
413	0.68	0.53	-3.59 ± 3.41	16.76	1.00	WFPC	414	−0.45	1.04	7.59 ± 4.43	16.75	1.00	LCO
415	−0.23	−0.64	-9.62 ± 4.94	16.30	1.14	WFPC	418	−0.04	−0.14	24.06 ± 5.35	16.66	1.01	WFPC,3
419	−0.73	−0.11	1.45 ± 3.21	16.53	1.03	ACS	420	−0.19	−0.28	-5.09 ± 4.55	16.70	1.00	ACS,8
421	0.13	0.06	13.46 ± 1.63	16.08	0.71	WFPC,5	422	−0.65	1.07	14.49 ± 7.55	16.92	0.98	LCO,r
423	−0.73	−0.12	-6.21 ± 3.04	16.69	1.03	LCO	424	1.29	0.08	-7.97 ± 7.50	16.84	1.00	WFPC,r
426	−0.72	−0.38	21.23 ± 3.73	16.65	1.00	LCO	427	0.09	0.16	10.76 ± 6.71	16.38	1.03	WFPC
428	0.94	0.04	5.47 ± 4.56	16.78	0.98	WFPC	430	−0.36	−0.27	-10.02 ± 7.47	16.82	1.15	LCO
431	−0.02	−0.88	0.56 ± 2.74	16.64	1.01	WFPC	433	−0.25	0.29	4.93 ± 4.59	16.79	0.99	LCO
434	−0.82	−0.03	8.86 ± 4.54	16.64	1.02	LCO	435	−0.09	−0.06	-10.27 ± 4.24	16.28	1.05	WFPC
436	0.37	−0.76	-6.79 ± 3.94	16.57	1.06	WFPC	437	0.39	−0.49	-0.49 ± 4.84	16.62	1.02	WFPC
438	−0.20	0.28	0.47 ± 7.46	16.27	0.57	LCO	439	−0.97	−0.02	1.36 ± 6.44	16.38	0.64	LCO,8
441	−0.12	0.36	15.54 ± 3.48	17.17	0.26	ACS,3	442	0.24	−0.10	-10.22 ± 5.97	16.86	1.02	WFPC,5
443	0.04	−0.28	12.86 ± 6.90	15.90	0.20	WFPC	444	−1.35	0.31	13.66 ± 4.77	16.86	0.99	LCO
445	0.36	0.06	27.59 ± 5.66	17.08	1.01	WFPC	447	0.05	−0.26	1.56 ± 3.01	16.64	1.04	WFPC
448	0.19	0.15	-12.83 ± 4.70	16.98	0.97	WFPC	449	−0.36	−0.27	1.87 ± 5.62	17.04	0.84	LCO,5
450	−0.31	0.02	6.27 ± 5.02	16.47	1.03	ACS	452	−1.56	−0.43	5.91 ± 7.43	16.96	0.95	LCO,r
453	−0.43	0.82	28.86 ± 3.94	16.87	0.99	LCO	454	0.74	−0.84	-3.88 ± 7.71	16.78	0.98	WFPC
455	−0.50	0.22	15.91 ± 3.99	16.86	1.02	LCO	456	0.02	0.55	25.96 ± 3.50	16.71	0.97	LCO
457	−0.08	−0.22	0.94 ± 4.40	16.73	0.94	WFPC,5	458	−0.45	−0.41	5.18 ± 4.25	16.70	1.00	LCO
459	0.32	0.92	8.35 ± 5.76	16.99	1.00	WFPC	460	−0.88	0.39	3.48 ± 5.06	16.84	1.00	LCO
461	−0.54	0.03	-6.92 ± 4.26	16.90	1.03	LCO	462	−0.02	0.22	21.85 ± 5.19	16.87	1.00	WFPC,8
464	0.11	0.28	20.82 ± 5.22	16.71	0.98	WFPC	465	0.23	−0.46	19.31 ± 5.25	16.62	1.06	WFPC
466	0.25	−0.23	12.81 ± 3.71	16.83	0.97	WFPC,3	467	−0.14	−0.46	8.08 ± 4.99	16.71	0.99	WFPC
468	−0.76	0.17	11.90 ± 2.59	16.81	0.98	LCO	470	0.43	−0.19	4.44 ± 5.69	16.54	0.24	WFPC,5
471	0.23	0.43	28.39 ± 4.79	16.93	0.97	WFPC	472	−0.36	0.19	1.99 ± 4.05	17.46	0.99	ACS,3
473	0.29	−0.31	1.58 ± 4.44	16.66	0.97	WFPC	474	0.44	0.32	-2.83 ± 3.82	16.81	0.94	WFPC
476	0.40	0.41	12.57 ± 4.72	17.00	0.98	WFPC	477	−0.15	0.95	-4.46 ± 3.93	16.76	0.94	WFPC
478	−0.39	0.91	18.37 ± 6.43	17.03	0.95	LCO	479	0.13	−0.16	5.96 ± 3.33	17.55	0.97	WFPC,3
480	−0.27	0.28	11.38 ± 4.32	16.81	0.96	LCO	481	0.47	0.42	10.58 ± 6.61	16.83	1.00	WFPC

Table 4.1 (cont'd)

Star	X (′)	Y (′)	Velocity km s^{-1}	V	B-V	Notes	Star	X (′)	Y (′)	Velocity km s^{-1}	V	B-V	Notes
482	0.79	0.53	17.39 ± 5.91	17.07	0.98	WFPC	484	−0.23	0.27	17.88 ± 5.63	16.85	0.79	LCO,8
485	0.44	−0.31	15.58 ± 4.17	16.91	0.96	WFPC	486	−0.17	−0.95	21.45 ± 4.46	16.57	1.05	WFPC
487	0.66	−0.59	13.06 ± 5.46	16.83	1.04	WFPC	488	0.06	−0.50	5.13 ± 5.58	15.98	0.14	WFPC
489	0.14	0.55	3.75 ± 4.96	17.18	0.92	WFPC,3	490	−1.06	−0.27	6.70 ± 4.95	17.00	0.97	LCO
491	−0.66	−0.22	0.45 ± 5.07	16.91	1.01	LCO	492	−0.44	−0.36	14.22 ± 5.20	16.81	0.93	LCO,3
494	0.29	−0.37	-1.90 ± 4.36	16.84	0.96	WFPC,8	495	0.32	0.33	6.61 ± 5.03	16.88	1.01	WFPC
497	−0.54	0.18	-2.79 ± 6.78	16.22	0.44	LCO	499	0.66	0.58	-9.06 ± 3.21	16.96	0.99	WFPC
500	0.19	−0.35	5.51 ± 6.00	16.25	0.27	WFPC,5	501	0.25	−0.34	-7.52 ± 5.73	16.87	1.01	WFPC
505	0.52	0.64	3.57 ± 6.78	17.02	1.00	WFPC	511	0.06	0.09	-9.51 ± 3.99	16.31	0.97	WFPC,8
512	−0.58	0.21	18.77 ± 6.36	17.01	0.96	LCO	513	−0.74	0.64	-10.96 ± 4.71	16.95	1.00	LCO
514	0.38	−0.27	10.56 ± 5.31	16.58	1.08	WFPC	515	−0.45	−0.35	0.02 ± 4.49	17.10	0.95	LCO,5
516	0.35	0.45	8.84 ± 6.03	16.99	0.92	WFPC	517	0.22	−0.43	-10.42 ± 5.92	16.95	1.02	WFPC
519	−0.37	0.15	4.84 ± 6.18	16.36	0.65	ACS	523	0.49	0.13	21.43 ± 6.41	17.05	0.96	WFPC
524	0.32	0.54	-3.15 ± 5.05	16.99	0.90	WFPC	525	0.27	−0.39	-4.75 ± 4.79	16.90	1.04	WFPC,8
526	−0.13	−0.28	5.76 ± 6.48	16.98	1.04	LCO	528	0.34	0.60	4.89 ± 5.42	17.03	0.98	WFPC
529	0.45	−0.73	-0.60 ± 7.58	16.18	0.33	WFPC	530	−0.25	−0.46	9.31 ± 4.57	16.87	1.00	LCO
531	−0.33	0.30	27.81 ± 5.35	17.05	0.93	LCO,8	532	−0.41	0.37	19.51 ± 6.97	17.07	1.03	LCO
536	−0.99	−0.11	4.22 ± 7.22	17.10	0.99	LCO	538	0.37	0.41	9.53 ± 5.08	17.13	0.93	WFPC
540	−0.08	0.44	5.91 ± 4.10	17.07	0.99	LCO	541	−0.51	0.90	4.49 ± 5.83	17.14	0.95	LCO
542	−0.16	0.14	9.60 ± 6.68	17.73	0.95	WFPC,3	543	−1.32	0.09	-1.05 ± 7.59	17.19	0.96	LCO
551	−0.29	0.74	9.11 ± 5.81	16.43	0.41	LCO,8	553	0.07	0.64	18.33 ± 4.69	17.05	0.89	WFPC
555	−0.21	−0.23	-1.50 ± 5.94	17.14	0.12	ACS,3	556	0.22	0.57	-2.03 ± 6.35	17.21	0.95	WFPC,3
557	−0.33	0.16	18.84 ± 4.53	17.90	1.03	ACS,3	558	−0.34	0.22	19.58 ± 6.36	17.34	1.00	ACS,5
559	0.50	−0.46	-5.49 ± 5.04	17.17	0.99	WFPC	560	−1.12	−0.23	28.77 ± 4.62	17.26	0.92	LCO
563	0.58	−0.37	23.19 ± 5.67	17.06	1.04	WFPC	565	−0.39	0.09	-3.44 ± 6.27	17.20	1.00	ACS
566	1.02	0.34	14.93 ± 7.94	16.45	0.25	WFPC	567	−0.19	0.31	2.34 ± 5.73	17.11	0.92	LCO,8
568	−0.10	−0.31	-7.57 ± 6.71	17.13	1.20	ACS,3	571	−0.35	0.50	-4.96 ± 4.81	17.18	0.93	LCO,8
572	−0.32	−0.45	-5.02 ± 4.54	16.45	0.48	ACS	574	−0.19	0.33	-7.77 ± 6.42	17.29	1.00	LCO,8
576	0.10	0.82	4.89 ± 6.54	17.10	1.00	WFPC	577	−0.70	0.09	-6.12 ± 6.49	17.07	0.92	LCO
579	−0.39	0.41	17.23 ± 7.05	16.36	0.42	LCO,5	582	0.07	−0.43	-6.47 ± 4.04	17.20	0.96	WFPC,3
583	0.39	−0.21	13.26 ± 6.55	17.09	0.94	WFPC	586	0.02	−0.38	-2.86 ± 6.68	16.94	0.95	WFPC
589	0.36	0.10	21.00 ± 4.71	17.46	1.08	WFPC,8	591	−0.68	−1.18	3.12 ± 7.91	16.40	0.40	LCO
592	−0.56	0.31	3.84 ± 5.29	17.31	0.99	LCO	594	−0.22	−0.19	6.90 ± 7.15	16.93	0.99	ACS
597	0.38	−0.01	-5.94 ± 5.92	17.25	0.98	WFPC,8	599	0.42	0.07	-11.54 ± 5.82	16.64	0.21	WFPC,5
601	0.43	−0.05	9.93 ± 6.31	17.13	0.89	LCO,8	603	−0.08	0.52	8.57 ± 5.80	17.17	1.04	LCO
604	−0.78	−0.45	3.88 ± 6.09	17.18	0.94	LCO	605	−0.48	−0.71	-8.01 ± 6.74	17.08	0.98	WFPC
606	0.27	0.81	19.46 ± 6.17	16.43	0.27	WFPC	607	−0.67	−0.04	19.51 ± 7.80	17.16	0.93	LCO
608	0.13	0.46	6.34 ± 6.94	16.38	0.42	LCO,8	609	−0.14	−0.36	12.61 ± 6.62	16.61	0.30	LCO
611	0.44	0.01	14.80 ± 6.79	···	···	–,*	613	−0.95	0.48	11.43 ± 7.29	17.35	0.95	LCO
616	0.52	0.10	6.74 ± 6.04	16.46	0.24	WFPC	620	0.47	0.60	13.33 ± 6.87	16.75	1.02	WFPC
621	−0.38	0.57	4.08 ± 7.55	16.45	0.35	ACS	624	0.46	0.82	24.62 ± 5.78	17.38	0.95	WFPC
625	0.16	−0.79	10.71 ± 5.73	17.17	0.97	WFPC	626	1.06	0.15	7.48 ± 7.04	17.44	0.96	WFPC
627	−0.11	0.02	16.78 ± 4.46	16.67	0.93	WFPC,5	631	0.48	−0.22	-5.07 ± 4.47	17.17	0.98	WFPC,8
633	0.09	0.53	2.59 ± 4.88	17.31	1.02	LCO	635	−0.02	−0.39	27.03 ± 6.54	16.43	0.29	WFPC
637	−0.14	0.12	11.87 ± 7.28	17.00	0.93	WFPC	643	−0.33	0.27	-1.25 ± 5.66	17.44	0.98	LCO
647	−0.54	0.01	6.96 ± 7.59	16.61	0.37	LCO,8	650	0.41	−0.50	7.77 ± 6.48	17.18	0.95	WFPC
653	0.13	−0.87	-8.57 ± 6.58	17.09	1.01	WFPC	661	0.06	−0.54	23.79 ± 7.19	16.38	0.30	WFPC
665	−0.45	0.04	2.90 ± 7.50	16.57	0.34	LCO,3	667	−0.27	0.34	7.50 ± 7.64	16.68	0.32	ACS,5
669	−0.76	−0.47	-2.12 ± 5.91	17.31	0.89	LCO	675	0.38	−0.68	-10.22 ± 5.63	17.42	0.95	WFPC
687	−0.76	−0.56	-1.14 ± 6.26	17.33	0.97	LCO	693	−0.06	0.27	14.15 ± 7.97	17.52	0.97	ACS,8
699	−0.28	0.49	12.16 ± 7.71	17.46	0.90	LCO,8	701	−0.23	−0.25	20.13 ± 6.83	17.05	1.01	ACS
709	−0.56	0.61	9.82 ± 7.79	17.46	0.89	LCO	719	0.67	−0.55	19.58 ± 7.15	17.50	0.97	WFPC
725	−0.49	−0.10	36.05 ± 5.19	17.65	1.04	LCO	739	−0.61	0.34	11.47 ± 7.81	17.45	0.88	LCO,5
747	−0.32	0.37	14.11 ± 6.07	17.47	0.89	LCO	751	0.05	−0.18	14.53 ± 6.14	17.01	0.96	WFPC,5
761	0.59	−0.28	3.97 ± 5.56	17.69	0.99	WFPC,5							

in two halves with a line through the center whose angle is varied through 180° in steps of 1°. The average velocity is calculated on each side and the largest difference between them we find is 3.52 km/s at a position angle of 238° (measured from North through East). We also use the same maximum likelihood technique used to measure the dispersion but where the mean velocity at the position of star i is the sinusoidal function

$$V_i = \langle V \rangle + V_{rot} \sin(pa_i - pa_0). \tag{4.1}$$

Here V_i and pa_i are the velocity and position angle of each star, respectively, pa_0 is the position angle of the axis of rotation and we allow for V_{rot} to be either a constant or have the form for solid-body rotation, $V_{rot} = Cr$. The results for the constant V_{rot} case were $pa_0 = 246.1° \pm 17.1°$, $V_{rot} = 2.42 \pm 0.81$ km s^{-1}, $\langle V \rangle = 7.41 \pm 0.54$ km s^{-1} and a velocity dispersion of $\sigma = 9.97 \pm 0.46$ km s^{-1}and for the solid-body case we obtain $pa_0 = 256.1° \pm 18.1°$, $C = 3.59 \pm 1.18$ km s^{-1}arcmin^{-1}, $\langle V \rangle = 7.37 \pm 0.53$ km s^{-1} and $\sigma = 9.95 \pm 0.45$ km s^{-1}. Both cases are consistent with our previous estimate. Finally, we ran 1000 Monte Carlo simulations that replaced the measured velocities with normal random deviations with a constant mean to test the significance of the rotation. The rotation amplitude was larger than 2.08 km s^{-1} only 5% of the time. The probability of detecting a sinusoidal amplitude as large or larger than the observed value of 2.42 km/s was 0.02. Although M80 is not observed to have any axial flattening in the range r=16-49″ by White & Shawl (1987), their reported position angle for the major axis of $\theta_e = 161 \pm 4°$ is perpendicular to our axis of rotation as expected if rotation were the main driver of the flattening. Frenk & Fall (1982) find an ellipticity of 0.06, but do not report the position angle of the major axis.

4.2 Other necessary data

One first step in using the new kinematic information for M80 is to construct simple multimass King-Michie models. These require an IMF to derive the amount of mass in each

Table 4.2. Velocity dispersion radial profile

Range ($'$)	<R> ($'$)	σ km s^{-1}
Range ($'$)	<R> ($'$)	σ km s^{-1}
0.04–0.22	0.15	13.76 ± 1.60
0.23–0.36	0.29	12.10 ± 1.46
0.36–0.44	0.40	9.58 ± 1.23
0.44–0.51	0.48	9.99 ± 1.31
0.51–0.60	0.55	8.70 ± 1.14
0.60–0.70	0.65	8.24 ± 1.07
0.70–0.84	0.77	9.63 ± 1.18
0.84–0.95	0.90	9.46 ± 1.24
0.95–1.13	1.01	8.83 ± 1.15
1.13–1.55	1.26	8.64 ± 1.09

stellar class, a stellar mass-luminosity relation to convert the density models to light, and a surface-brightness profile to constrain them. Our procedure follows closely that of G&G but with significant updates to the IMF and mass-luminosity relations. We adopt a distance of 10.8 Kpc derived from the distance modulus of 15.85 reported by Recio-Blanco et al. (2005) from the fitting of theoretical horizontal branch models to the CMD of WFPC2/HST data. The adopted reddening is E(B-V) = 0.18 from Harris (1996) and the extinction is A_V = 0.583.

4.2.1 Surface-brightness profile

We adopt the profile derived from CCD surface photometry reported in the Trager et al. (1995) compilation. Their CRB1 profile was observed in the B band at the Cerro Tololo Inter-American Observatory (CTIO). We estimate sampling uncertainties based on the amount of light in each annulus using King's prescription (King 1966). In the outer regions of M80, we adopt data from photographic star counts from King et al. (1968), specifically

their Palomar Schmidt (PS) plate in the B band. The full surface brightness profile adopted in this work is presented in Fig. 4.3 together with our best fit model (see §4.4).

4.2.2 Mass function, luminosity function and mass classes

We approximate the continuous spectrum of stellar masses with 9 discrete mass bins (see Table 4.3). Each bin contains main-sequence stars, giants, stellar remnants, or a mixture of these types. The mixture and the total mass in each bin are determined by the IMF, though we also include a simple representation of the effects of the dynamical evolution of the cluster on the mass function. For $m \leqslant 0.9 M_{\odot}$ we adopt the lognormal IMF distribution derived by Paresce & De Marchi (2000) from the luminosity functions of a dozen globular clusters observed with HST. The high-mass end is more uncertain and thought to be a power law with an exponent close to the Salpeter value X = 1.3 ± 0.3 (see Chabrier 2003). The mass of main-sequence stars and giants in each bin is calculated with

$$M_i = \int_i m\xi(m)dm, \tag{4.2}$$

where the IMF ξ is

$$\xi(logm) \propto \begin{cases} \exp(-\frac{[\log m - \log(0.33\pm0.3)]^2}{2(0.34\pm0.04)^2}) & : m \leqslant 1.0 M_{\odot} \\ m^{-x} & : m > 1.0 M_{\odot} \end{cases} \tag{4.3}$$

Our four most massive mass bins require the addition of dark remnants. We calculate the amount of dark remants with an initial-final mass relationship for white dwarfs from Catalán et al. (2008) by extrapolating their observed progenitor mass from the range 1–6.5 $M_{\odot}$ to 0.8–8 $M_{\odot}$. This relationship – two different linear fits transitioning at 2.7 $M_{\odot}$ – gives the mass of the present-time remnant star (a white dwarf), m_f, as a function of the mass of the progenitor. The contribution of dark remnants is simply $M_i = \int_i m_f \xi(m)dm$ using the mass range of the progenitors that would end up in our mass bins. The above treatment of white dwarfs is uncertain and also doesn't take into account the modification of the cluster mass function by tidal stripping. Because of equipartition, low-mass stars are thought to

Table 4.3. Mass bins for multimass models.

Bin No.	Mass range (log m)	Mean mass ($M_\odot$)	L/M $L_{V\odot}/M_\odot$	Contents
1		1.2	0.0	wd
2	$-0.2, 0.0$	0.710	4.6	ms, giants, wd
3	$-0.4, -0.2$	0.501	0.129	ms, wd
4	$-0.6, -0.4$	0.316	0.045	ms, wd
5	$-0.8, -0.6$	0.200	0.025	ms
6	$-1.0, -0.8$	0.126	0.011	ms
7	$-1.2, -1.0$	0.079	0.0	ms
8	$-1.4, -1.2$	0.050	0.0	ms
9	$-1.6, -1.4$	0.032	0.0	ms

have been preferentially lost in the past, decreasing the present-time fraction of low-mass stars and increasing that of white dwarfs (Baumgardt & Makino 2003; Vesperini & Heggie 1997). We crudely model tidal stripping with a constant multiplicative factor (f_{wd}) of white dwarfs that, when larger than one, increases the mass fraction of the remnants of massive stars as expected because of tidal stripping.

Neutron stars are observed to be born with high velocities and therefore their retention numbers are very low. Neutron stars could be accounted for with $M_{ns} \propto 1.4 f_{ns} \int \xi(m) dm$ with the retention factor $f_{ns} \approx 0.05$ as suggested by Pfahl et al. (2002). We find that their effect on our conclusions is negligible and therefore they have been ignored.

The last ingredient that makes comparisons between models and data possible is the luminosity function. For consistency, we follow Paresce & De Marchi (2000) and adopt the model of Baraffe et al. (1997) for stars in main sequence mass bins. We note however that by far the most important luminosity is that of the red giants. We adopt the L/M derived from observed luminosity functions of M3, 47 Tuc and M92 by Pryor et al. (1991). The metallicity of M80 is comparable to that of M3 and M92. Table 4.3 presents our mass bins, with the mean mass per bin and its light-to-mass ratio L/M.

4.3 Models

Here we briefly summarize the construction of multimass anisotropic Michie-King models but the interested reader is referred to Gunn & Griffin (1979), Pryor et al. (1986) (see also Kent & Gunn (1982) for insightful discussions and compact relations for the single-mass case).

A model surface-brightness profile can be created by projecting each mass density profile for mass class i, $\rho_i(r)$, and converting from mass to light through a $(L/M)_i$. Model density profiles $\rho_i(r)$ are found by solving the Poisson equation $\nabla_r^2 W = \rho$ numerically for the potential W after adopting the Michie-King (Michie 1963; King 1965) distribution function:

$$f(E, J) \propto e^{-J^2/(2v_s r_a)^2} \times (e^{-A_i E} - 1), \tag{4.4}$$

which causes $\rho(W) = \int f(E, J) d^3v$ to be only a function of W. In Eq. 4.4, E and J are the energy and angular momentum and one assumes thermal equilibrium at the center (short relaxation times), which implies that A_i is proportional to the mean mass of mass class i. In Eq. 4.4, the anisotropy of the velocity dispersion tensor is controlled by the transition radius, r_a, beyond which stellar orbits become primarily radial. The Michie-King models do not include net rotation. This is an acceptable approximation because the dynamical significance of rotation is proportional to the square of the ratio of v_{rot} to σ which is much less than one for M80 (see section 4.1.5). Operationally, a dimensionless Poisson equation is integrated outwards from the center, where $\mathrm{d}W/\mathrm{dr} = 0$ and $W = W_0$, until the cluster edge (the tidal radius) is reached. Thus, W_0 is the parameter that controls the concentration $c \equiv \log(r_t/r_s)$ and which we vary to produce a grid of models. All multimass models have four free parameters. Two of them control the shape of the density profile: the concentration and the anisotropy radius. The remaining two parameters provide the physical scalings to the otherwise dimensionless models: the scale radius r_s and the scale velocity v_s. The total mass of the cluster is found with $M = (9/4\pi G) d r_s v_s^2 \mathcal{M}$, where $\mathcal{M}$ is

the dimensionless mass and d is the distance to the cluster.

4.3.1 Fitting the models

The procedure has been extensively described in Pryor et al. (1989). A grid of dimensionless models was constructed covering a range of concentrations from 1.0 to 3.0 in steps of 0.05. Models are fitted with least squares techniques to the surface brightness profiles. The best fit (lowest χ^2) yields the concentration parameter c, scale radius r_s, central surface brightness μ_{0V}, and total apparent magnitude V_t. The models are also fitted to the velocity data with the G&G maximum likelihood technique to obtain the scale velocity v_s. The above fitted parameters yield the dynamical, or "virial", M/L and central $(M/L)_0$. The expressions were given in Pryor et al. (1989) and we repeat them here for convenience. The central or core $(M/L)_0$ is given by the ratio of the central projected mass density to the central surface brightness:

$$\left(\frac{M}{L_V}\right)_0 = (0.715 M_\odot/L_{V\odot})\, 10^{0.4(\mu_{0V}-A_V-7.0)} \times \left(\frac{v_s}{10 \text{ km s}^{-1}}\right)^2 \left(\frac{0.5'}{r_s}\right) \left(\frac{10 \text{ kpc}}{d}\right) \Sigma_0, \tag{4.5}$$

where μ_{0V} the central surface brightness profile in V mag arcmin^{-2}, A_V the extinction, d the cluster distance and Σ_0 the dimensionless central projected density of the model. The central $(M/L)_0$ can be interpreted as the average M/L in the region where we have velocity information. Similarly, though more model dependent, the global M/L is given by

$$\left(\frac{M}{L_V}\right) = (2.13 M_\odot/L_{V\odot})\, 10^{0.4(V_t-A_V-6.0)} \times \left(\frac{v_s}{10 \text{ km s}^{-1}}\right)^2 \left(\frac{r_s}{0.5'}\right) \left(\frac{10 \text{ kpc}}{d}\right) \left(\frac{\mathcal{M}}{30}\right), \tag{4.6}$$

with $\mathcal{M}$ the dimensionless model mass and V_t the cluster's total V magnitude. The population global M/L and central $(M/L)_0$ are determined from the mass-luminosity relation and the mass function. In a self-consistent model, the population M/L and $(M/L)_0$ should be in reasonable agreement with their dynamical counterparts.

The uncertainties are estimated with Monte-Carlo simulations in which 1000 artificial

sets of surface brightness and velocity data are created. Each set is derived from the best-fit model by using the uncertainties for each surface-brightness/velocity point. The $1-\sigma$ deviations around the parameter's mean in the 1000 fits are taken to be the uncertainties in the parameters.

The three parameters that we allow ourselves to vary to learn about the dynamical state of the cluster are the power law index x in the mass function (Eq. 4.3), the dark remnant multiplicative factor f_{wd} described in section 4.2.2, and the anisotropy radius r_a.

4.4 Results

The results of our model fits are presented in Table 4.4 for different combinations of f_{wd}, x and r_a. Here the first column is the anisotropy radius in units of r_s, followed by the concentration and χ^2 per degree of freedom and the probability of seeing a χ^2 that large or larger. Column 5 is the scale radius followed by the fitted central V band surface brightness and the fitted total V magnitude. The scale velocity v_s is given in column 9. The next 4 columns are the population M/L and $(M/L)_0$ followed by their dynamical counterparts. The last column is an estimate of the agreement between dynamical and population M/L and is simply the fraction of Monte Carlo realizations in which the dynamical M/L was larger/smaller than the population M/L if the best-fit dynamical M/L is less/more than the population M/L.

We begin with the simplest model possible, the single-component model in which mass strictly follows light. The best-fit model is that in which $r_a = 10r_s$ and, in fact, in all our experiments better fits to the surface brightness profile were obtained when the anisotropy radius was $10r_s$. Next follow the multimass models with the expected amounts of dark remnants ($f_{wd} = 1.0$, $x = 1.3$). Multimass models have a larger dynamical total M/L than the single mass models since they include dark main-sequence low-mass stars which are more spatially extended than the light because of equipartition. In general, the dynamical total M/L is more sensitive than the central $(M/L)_0$ to parameters of the models that

control the shape of the surface brightness profile (concentration, anisotropy, mass fractions) since it depends on the total integrated dimensionless mass $\mathcal{M}$. Once again, the best model is that in which $r_a = 10r_s$ and with a somewhat better χ^2 than the single mass case. The population M/L and $(M/L)_0$ are unacceptably much lower than their dynamical counterparts.

To investigate this discrepancy, we start by testing our dynamical M/L. Although we have found and removed a few foreground stars based on their colors, M80 is at a low galactic latitude, $b = 19.46°$, towards the center of the galaxy, $\ell = 352.67°$ (Harris 1996) and we could have missed more non-member stars. For example, the Besancon population synthesis model of the Galaxy (Robin et al. 2003) predicts 22 foreground stars in the field of view of our Fabry-Perot observations. This contamination, if present, should affect more the outer parts of the radial dispersion profile. We therefore re-fitted the observations using only stars within half the radius ($0.75'$) of the original field of view and find differences in the dynamical M/L of at most 14% (which is within the uncertainty).

We now turn our attention to the more uncertain population M/L. The lower population M/L suggests a need for more dark stellar mass, i.e. dark remnants or low main-sequence stars. Experiments with power law IMF as low as x=0.67 below the turnoff mass to increase the amount of low-mass stars did not produce enough dark stars. We therefore experimented with the number of dark remnants through a multiplicative factor f_{wd}. This also has the effect of decreasing the relative fractions of main sequence low-mass stars and, thus, changes the shape of the density profiles. Table 4.4 shows that the fit to the surface-brightness profile improves as f_{wd} increases. The model with XR=1.3 with the best agreement between the population and dynamical M/L's has $f_{wd} = 4.5$ and is presented in Figs. 4.3 and 4.4.

Our measured M/L for M80 is best reproduced by a model with a large enhancement of the present-day number of white dwarfs compared to what is expected for the typical globular cluster initial mass function. The mass fraction in white dwarfs is expected to

Table 4.4 Fitted model parameters for single- and multi-mass models.

$\frac{r_a}{r_S}$	c	$\frac{\chi^2}{\text{dof}}$	P(χ^2)	$r_s(')$	μ_{oV} mag arcmin^{-2}	V_t	v_S	population $\frac{M}{L_V}$	population $\left(\frac{M}{L_V}\right)_0$	dynamical $\frac{M}{L_V}$	dynamical $\left(\frac{M}{L_V}\right)_0$	P(M/L)
					single mass							
I	1.70	2.6	0.000	0.16± 0.01	6.60± 0.09	7.51± 0.02	12.4± 0.5	—	—	2.6± 0.2	2.5± 0.2	0.000
10	2.00	1.4	0.083	0.17± 0.01	6.58± 0.07	7.43± 0.03	12.6± 0.5	—	—	2.5± 0.2	2.5± 0.2	0.000
06	2.20	1.8	0.006	0.20± 0.01	6.84± 0.07	7.41± 0.04	12.8± 0.5	—	—	2.5± 0.2	2.5± 0.2	0.000
03	2.65	3.6	0.000	0.27± 0.01	7.08± 0.06	7.41± 0.03	13.7± 0.6	—	—	2.7± 0.2	2.6± 0.2	0.000
					multimass, f_{wd}=1.0							
I	1.85	2.4	0.000	0.11± 0.01	6.53± 0.10	7.52± 0.02	9.8± 0.4	1.53	1.04	3.7± 0.3	2.4± 0.2	0.000
10	2.75	1.3	0.167	0.13± 0.01	6.62± 0.06	7.38± 0.03	10.3± 0.4	1.53	0.98	4.0± 0.3	2.5± 0.2	0.000
06	3.00	2.2	0.000	0.17± 0.01	6.85± 0.07	7.28± 0.07	10.9± 0.4	1.53	0.96	4.2± 0.4	2.5± 0.2	0.000
03	3.00	3.9	0.000	0.24± 0.01	7.08± 0.07	7.13± 0.14	12.3± 0.5	1.52	0.95	4.3± 0.4	2.6± 0.2	0.000
					multimass, f_{wd}=3.0							
I	1.90	3.3	0.000	0.08± 0.01	6.34± 0.12	7.56± 0.02	10.1± 0.4	2.40	2.47	3.0± 0.3	3.0± 0.3	0.006
10	2.40	1.0	0.458	0.11± 0.01	6.53± 0.07	7.43± 0.03	10.7± 0.4	2.40	2.20	3.3± 0.3	2.9± 0.2	0.000
06	2.95	1.9	0.004	0.15± 0.00	6.80± 0.06	7.36± 0.03	11.1± 0.5	2.40	2.04	3.4± 0.3	2.8± 0.2	0.000
03	3.00	2.8	0.000	0.16± 0.01	6.78± 0.06	5.77± 0.06	13.3± 0.6	2.40	2.67	3.0± 0.3	3.3± 0.3	0.006
					multimass, f_{wd}=4.5							
I	1.90	3.7	0.000	0.08± 0.01	6.42± 0.13	7.56± 0.02	10.2± 0.4	3.05	3.49	3.0± 0.3	3.3± 0.3	0.357
10	2.35	1.0	0.517	0.10± 0.01	6.50± 0.08	7.44± 0.04	10.8± 0.4	3.06	3.09	3.1± 0.3	3.0± 0.3	0.462
06	2.95	1.8	0.010	0.14± 0.01	6.78± 0.06	7.37± 0.04	11.3± 0.5	3.06	2.87	3.2± 0.3	2.9± 0.2	0.276
03	3.00	2.9	0.000	0.15± 0.00	6.74± 0.07	5.60± 0.02	13.5± 0.6	3.06	3.83	2.8± 0.2	3.5± 0.3	0.104
					multimass, f_{wd}=6.0							
I	1.80	4.0	0.000	0.10± 0.02	6.57± 0.13	7.57± 0.02	10.3± 0.4	3.71	4.15	2.9± 0.2	3.2± 0.3	0.002
10	2.35	0.9	0.548	0.10± 0.01	6.48± 0.08	7.44± 0.04	11.0± 0.5	3.71	3.99	3.0± 0.3	3.1± 0.3	0.004
06	2.95	1.7	0.015	0.14± 0.01	6.76± 0.07	7.36± 0.04	11.4± 0.5	3.71	3.69	3.1± 0.3	3.0± 0.3	0.018
03	3.00	2.9	0.000	0.15± 0.00	6.73± 0.07	5.54± 0.02	13.6± 0.6	3.71	4.93	2.7± 0.2	3.5± 0.3	0.000

increase if the mass loss driven by tidal forces is significant (Baumgardt & Makino 2003; Vesperini & Heggie 1997). M80 is on a Galactic orbit that keeps it in the inner regions of the Galaxy and, thus, is predicted to have experienced significant tidal mass loss (Dinescu et al. 1999). The only problem with claiming that our results confirm the theoretical predictions is that our increase in the white dwarf mass fraction, about 4.5×, is larger than the $< 2\times$ increase predicted by the mumerical models of cluster dynamical evolution (Vesperini & Heggie 1997). The models also predict the greatest increase shortly before the complete destruction of the cluster, when the system is predicted to have low luminosity and central concentration. The clusters that are observed to have present-day main-sequence mass functions that are strongly depleted in low mass stars, probably because of tidal stripping, all have low or intermediate concentrations and luminosities smaller than that of M80 (De Marchi et al. 2007). On the other hand, the dynamical models still include significant simplifications and have been run for only a modest set of initial conditions and Galactic orbits. Simulations for clusters resembling M80 would be interesting. It would also be useful to measure the mass function on the upper main sequence of M80 — this should be possible with the existing ACS imaging. Direct measurements of the number of white dwarfs in M80 might also be possible, though it would require much deeper imaging.

4.5 Summary

The primary purpose of this work was to report the observation of 543 radial velocities in the globular cluster M80 using Fabry-Perot spectrography. By matching our sample of stars with HST observations we were able to identify and remove blended stars and have therefore been able to estimate reliable velocities near the center. Our sample allowed us to estimate the expected declining dispersion profile and also the first detection of rotation in this cluster. M80 is rotating about an axis that is perpendicular to the major axis of the cluster-flattening, though the flattening itself is very close to zero.

We have taken a first step in using our new kinematic information by constraining

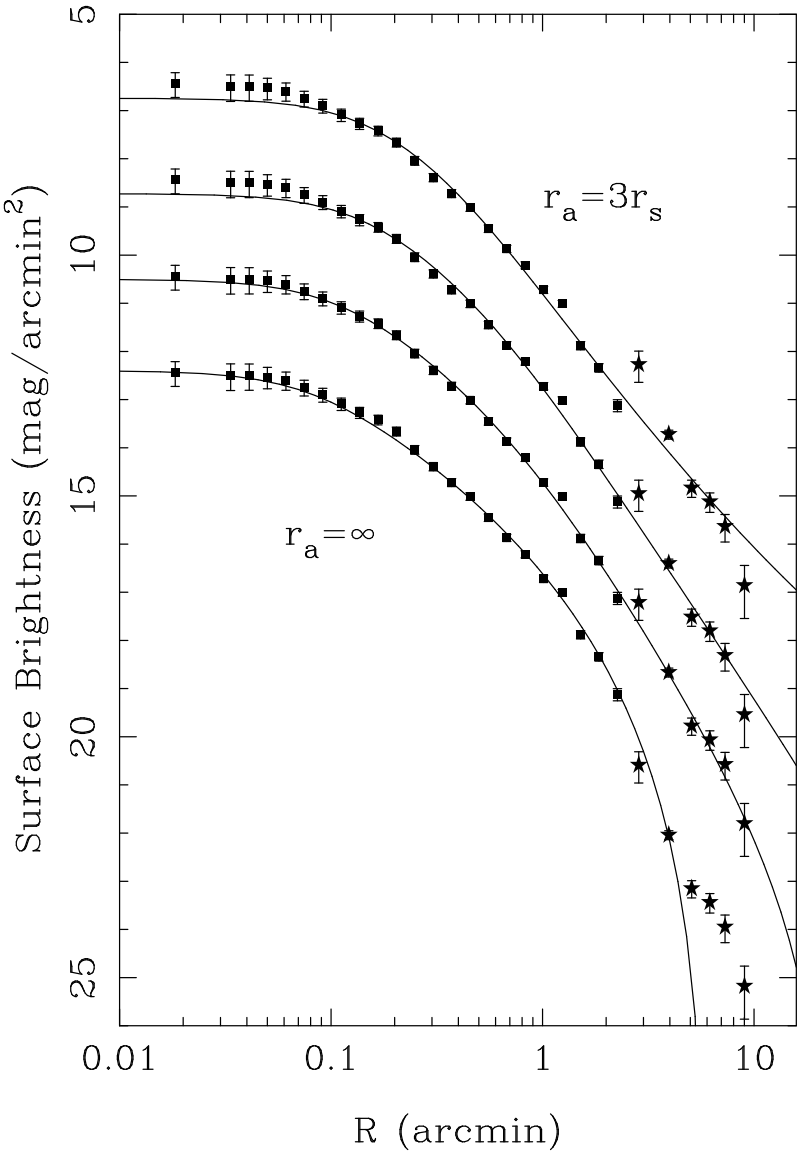

Figure 4.3 Surface brightness profile of M80 and the best-fitting multi-mass models for different values of the anisotropy r_a. The solid squares are the CCD surface brightness photometry from Trager et al. (1995) and the solid stars are the PS-7587 star counts of King et al. (1968). The uppermost line is the fitted model for $r_a = 3r_s$. The best-fit models for the $r_a = 6r_s, 10r_s,$ and ∞ (isothermal) cases are shown shifted by 2.0 mag for clarity.

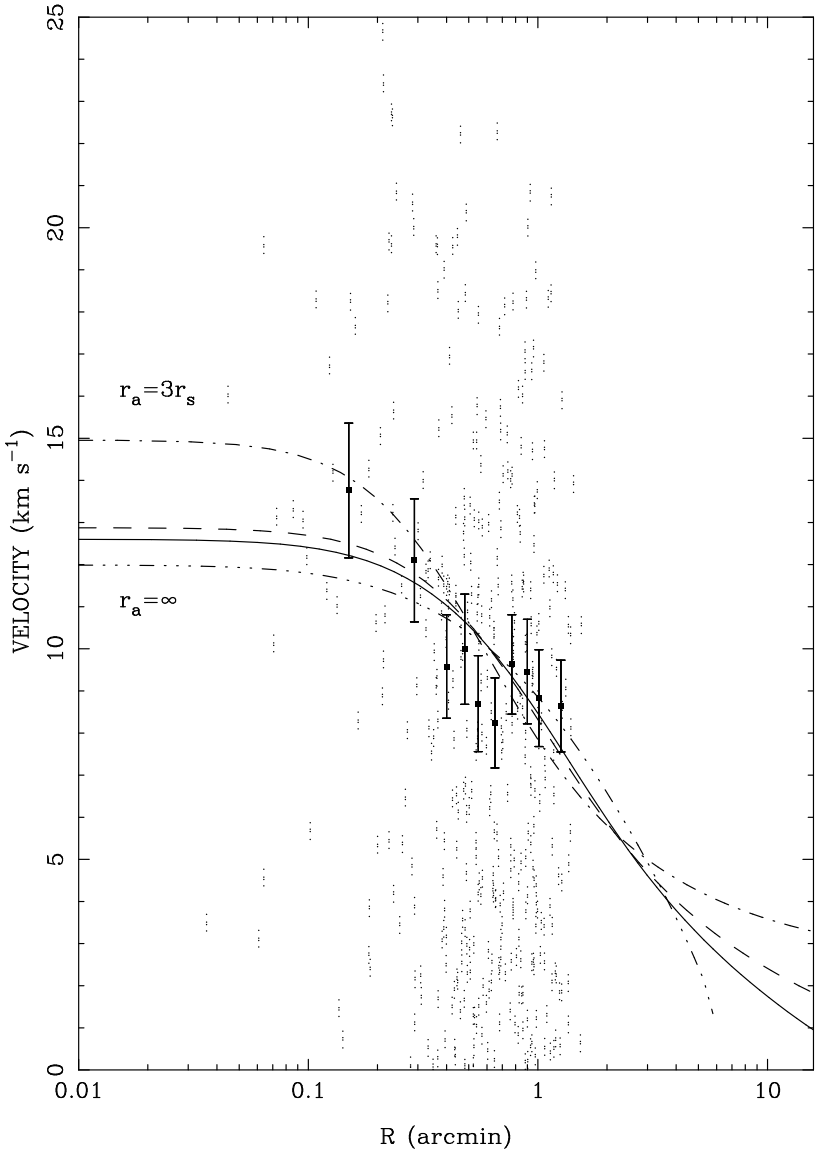

Figure 4.4 Velocity data and four fitted velocity-dispersion profiles. The curves are the best-fit velocity dispersion profiles for models with $f_{wd} = 4.5$ and different values of the anisotropy radius, r_a. The points are the absolute value of the difference between the stellar velocity and fitted mean cluster velocity for each model (closely spaced points are due to small differences in the fitted mean). Solid squares and error bars are the velocity dispersion profile in ten bins. Note that the models are fitted to all of the star velocities, not the binned data.

simple Michie-King multimass anisotropic models. Our models are based on the lognormal initial mass function expected in globular clusters (Paresce & De Marchi 2000). Only by increasing the amounts of white dwarfs beyond those prescribed by the IMF are we able to reconcile the dynamical and population estimates of the M/L. We tentatively interprete this as evidence of tidal stripping that has evaporated low main-sequence stars. This is consistent with M80's observed Galactic orbit that keeps it confined to the inner regions of the Galaxy and therefore is likely to have experienced significant tidal mass loss. It would be interesting to carry out simulations with M80's characteristics to further support this case.

Bibliography

Alcaino, G., Liller, W., Alvarado, F., Kravtsov, V., Ipatov, A., Samus, N., & Smirnov, O. 1998, AJ, 116, 2415

Baraffe, I., Chabrier, G., Allard, F., & Hauschildt, P. H. 1997, A&A, 327, 1054

Baumgardt, H., & Makino, J. 2003, MNRAS, 340, 227

Brocato, E., Castellani, V., Scotti, G. A., Saviane, I., Piotto, G., & Ferraro, F. R. 1998, A&A, 335, 929

Catalán, S., Isern, J., García-Berro, E., & Ribas, I. 2008, MNRAS, 387, 1693

Chabrier, G. 2003, PASP, 115, 763

De Marchi, G., Paresce, F., & Pulone, L. 2007, ApJ, 656, L65

Dinescu, D. I., Girard, T. M., & van Altena, W. F. 1999, AJ, 117, 1792

Dolphin, A. E. 2000, PASP, 112, 1383

Ferraro, F. R., Paltrinieri, B., Rood, R. T., & Dorman, B. 1999, ApJ, 522, 983

Frenk, C. S., & Fall, S. M. 1982, MNRAS, 199, 565

Gebhardt, K., Pryor, C., Williams, T. B., Hesser, J. E., & Stetson, P. B. 1997, AJ, 113, 1026

Gunn, J. E., & Griffin, R. F. 1979, AJ, 84, 752

Harris, W. E. 1996, AJ, 112, 1487

Kent, S. M., & Gunn, J. E. 1982, AJ, 87, 945

King, I. R. 1965, AJ, 70, 376

—. 1966, AJ, 71, 276

King, I. R., Hedemann, E. J., Hodge, S. M., & White, R. E. 1968, AJ, 73, 456

Michie, R. W. 1963, MNRAS, 125, 127

Ochsenbein, F., Bauer, P., & Marcout, J. 2000, A&AS, 143, 23

Paresce, F., & De Marchi, G. 2000, ApJ, 534, 870

Pfahl, E., Rappaport, S., & Podsiadlowski, P. 2002, ApJ, 573, 283

Piotto, G., King, I. R., Djorgovski, S. G., Sosin, C., Zoccali, M., Saviane, I., De Angeli, F., Riello, M., Recio-Blanco, A., Rich, R. M., Meylan, G., & Renzini, A. 2002, A&A, 391, 945

Pryor, C., Hartwick, F. D. A., McClure, R. D., Fletcher, J. M., & Kormendy, J. 1986, AJ, 91, 546

Pryor, C., McClure, R. D., Fletcher, J. M., & Hesser, J. E. 1989, AJ, 98, 596

—. 1991, AJ, 102, 1026

Pryor, C., & Meylan, G. 1993, in Astronomical Society of the Pacific Conference Series, Vol. 50, Structure and Dynamics of Globular Clusters, ed. S. G. Djorgovski & G. Meylan, 357–+

Recio-Blanco, A., Piotto, G., de Angeli, F., Cassisi, S., Riello, M., Salaris, M., Pietrinferni, A., Zoccali, M., & Aparicio, A. 2005, A&A, 432, 851

Robin, A. C., Reylé, C., Derrière, S., & Picaud, S. 2003, A&A, 409, 523

Shara, M. M., & Drissen, L. 1995, ApJ, 448, 203

Stetson, P. B. 1987, PASP, 99, 191

Trager, S. C., King, I. R., & Djorgovski, S. 1995, AJ, 109, 218

Vesperini, E., & Heggie, D. C. 1997, MNRAS, 289, 898

White, R. E., & Shawl, S. J. 1987, ApJ, 317, 246

Xie, B. 2003, PhD thesis, Rutgers The State University of New Jersey - New Brunswick

Chapter 5

Conclusions

This work was primarily concerned with characterizing and modeling non-circular motions of gas in spiral galaxies, and with the motion of stars in the globular cluster M80.

We applied the bisymmetric model proposed by Spekkens & Sellwood (2007) to characterize non-circular streaming motions of gas in both Hα and HI gas for disk galaxies in the THINGS (Walter et al. 2008) and BHαBar (Hernandez et al. 2005) samples. We find that this physically-motivated model, embodied in the software *velfit*, offers a number of advantages over harmonic analysis decomposition (Schoenmakers et al. 1997). For example, this approach is not limited to small distortions and therefore can be applied to model flows observed in bars, it analyzes all of the data at once and therefore should be more sensitive to global disturbances expected from triaxial dark matter halos, and its model parameters are easily related to the underlying gravitational potential.

We analyzed galaxies that were not obviously affected by spiral arm streaming motions in the THINGS sample and agree with the conclusion of Trachternach et al. (2008) that the dark matter halos of NGC 3198 and NGC 2403, as inferred from the HI velocity maps, are consistent with being round. More stringent constraints on the shape of dark matter halos would be possible with a model that could identify streaming motions despite the persistent warps present in most extended HI maps. It is also conceivable that warped disks themselves are manifestations of non-spherical halos (see Binney 1978). Clearly a lot more needs to be done to resolve these issues.

The expected lack of HI in galactic bars prevented us from finding clear bisymmetric signatures in two out of three barred galaxies in the THINGS sample. Nevertheless for

NGC 2903, despite the low spatial resolution of HI, we identify a bisymmetric disturbance that is aligned with the optical bar. We have confirmed this result in a higher-resolution Hα map that shows distinctly, that this galaxy does have a pronounced non-axisymmetric flow in the bar region. The higher spatial resolution of Hα allowed us to estimate large bisymmetric amplitudes and therefore should be the preferred tracer for bar studies.

Our analysis allowed us to find mild bisymmetric distortions in NGC 7793 and NGC 2976. The latter had been extensively studied by Simon et al. (2003) and Spekkens & Sellwood (2007) and the position angle and radial extent of the distortion is suggestively aligned with an elongation of the galaxy reported by Menéndez-Delmestre et al. (2007). It would be interesting to model the non-circular flows of this dark-matter-dominated galaxy (suggested by its gently rising rotating curve) with hydrodynamical simulations to constrain a bar model or even a possible triaxial halo.

Although characterizing non-circular flows proved to be a useful exercise, we also embarked on the much more ambitious task of modeling the gas flow in the barred galaxy NGC 1365. The gravitational potential of the model was based on new observations that included V- and I-band photometry, Fabry-Perot spectroscopy and a re-analysis of archival VLA HI observations. The distortions imprinted by the bar on a 2-dimensional velocity map offered a unique opportunity to break the disk-halo degeneracy. By varying the strength of the disk mass and the bar pattern speed in hydrodynamical simulations we found that the disk of NGC 1365 is massive, though not maximal, and that its bar is rotating fast. This method continues to find massive disks and fast bars and therefore poses a challenge to the ΛCDM paradigm that demands dark-matter-dominated galaxies. A welcome validation of the Weiner et al. (2001) method would come from modeling bars in low-surface-brightness galaxies where most of the mass is believed to be in the dark matter halo and, thus, should have a bar with a low M/L that has been slowed down by dynamical friction (Debattista & Sellwood 2000). However, the 2-dimensional kinematic maps required to constrain such models are clearly difficult, though not impossible, to observe (see, for example, the barred

galaxy F563-V2 in Kuzio de Naray et al. 2009).

In Chapter 4, we presented a first survey of radial velocities in the galactic globular cluster M80. Our sample allowed us to determine the expected declining velocity dispersion profile and also to make the first detection of rotation in this cluster, which is consistent with the mild observed flattening. We use simple Michie-King dynamical models to constrain the M/L of M80 and find that our model needs more dark remnants than those expected from the adopted initial mass function. We tentatively interpret this as evidence of tidal stripping that, because of mass segregation, has preferentially depleted the low mass stars. This is consistent with the observed space velocity of M80 (Dinescu et al. 1999), which shows that the cluster is confined to an orbit close to the galactic bulge and has therefore crossed the disk several times. It would be desirable to further support our findings with a measurement of M80's mass function on the upper main sequence and with proper motion studies, both of which should be possible with existing HST data. The now defunct Rutgers Fabry-Perot imaging spectrograph left as a last breath more raw data similar to that analyzed in Chapter 4 for a few more globular clusters. Who knows what other surprises lie in those observations? Only time will tell.

Bibliography

Binney, J. 1978, MNRAS, 183, 779

Debattista, V. P., & Sellwood, J. A. 2000, ApJ, 543, 704

Dinescu, D. I., van Altena, W. F., Girard, T. M., & López, C. E. 1999, AJ, 117, 277

Hernandez, O., Carignan, C., Amram, P., Chemin, L., & Daigle, O. 2005, MNRAS, 360, 1201

Kuzio de Naray, R., McGaugh, S. S., & Mihos, J. C. 2009, ApJ, 692, 1321

Menéndez-Delmestre, K., Sheth, K., Schinnerer, E., Jarrett, T. H., & Scoville, N. Z. 2007, ApJ, 657, 790

Schoenmakers, R. H. M., Franx, M., & de Zeeuw, P. T. 1997, MNRAS, 292, 349

Simon, J. D., Bolatto, A. D., Leroy, A., & Blitz, L. 2003, ApJ, 596, 957

Spekkens, K., & Sellwood, J. A. 2007, ApJ, 664, 204

Trachternach, C., de Blok, W. J. G., Walter, F., Brinks, E., & Kennicutt, R. C. 2008, AJ, 136, 2720

Walter, F., Brinks, E., de Blok, W. J. G., Bigiel, F., Kennicutt, R. C., Thornley, M. D., & Leroy, A. 2008, AJ, 136, 2563

Weiner, B. J., Sellwood, J. A., & Williams, T. B. 2001, ApJ, 546, 931

Appendix A

Applying a Smoothing Penalty

Spekkens & Sellwood (2007) fit a model by minimization of the usual function

$$\chi^2 = \sum_{n=1}^{N} \left(\frac{V_{\rm obs}(x,y) - \sum_{k=1}^{K} w_{k,n} V_k}{\sigma_n} \right)^2 . \tag{A.1}$$

Here $V_{\rm obs}(x,y)$ and σ_n are respectively the value of the observed velocity and its uncertainty for the n-th pixel at projected position (x,y), V_k is a coefficient of the fitted velocity around the k-th ellipse defined by the current guesses of ellipticity, ϵ, and position angle, ϕ. The index k ranges over K, which is the total all three sets of velocities that define the model velocity (eq. 2.4). The weights $w_{k,n}$, which include the trigonometric factors, also define the interpolation scheme that yields a model prediction at the point (x,y).

We can minimize a new function if we wish

$$X^2 = \chi^2 + \lambda \sum_{k=2}^{K-1} \mathcal{A} \left[V_{k-1} - 2V_k + V_{k+1} \right]^2 , \tag{A.2}$$

which adds a penalty for large second differences between the tabulated values V_k, which are assumed to be equally spaced, and the constant $\mathcal{A}$ is required to ensure that λ is dimensionless. The value of λ, which can be set independently for the axisymmetric and non-axisymmetric terms, can be adjusted as desired; small values have slight effect, while large values make the profile very smooth. Over-smoothing not only increases the value of χ^2, but may reduce the inner slope and smooth other real features in the rotation curve.

Since the magnitude of the second velocity difference (in square brackets) varies as the inverse square of the ring spacing, $\Delta R = R_{\rm max}/N_R$, we choose $\mathcal{A} = N_R^4/V_{\rm est}^2$, which ensures that the smoothing constraint is unaffected when the ring spacing is changed. Here, $V_{\rm est}$ is a constant that is a rough estimate of a typical orbital speed in the disc.

The smoothness constraint is applied only in the matrix that is solved to find the optimal values for V_k (see SS07), and adds extra terms as follows:

$$\frac{\partial X^2}{\partial V_j} = \frac{\partial \chi^2}{\partial V_j} + 2\lambda \mathcal{A} \left(V_{j-2} - 4V_{j-1} + 6V_j - 4V_{j+1} + V_{j+2} \right). \tag{A.3}$$

Appendix B

Bootstrap Estimation of Errors

A standard bootstrap technique is to estimate uncertainties in the parameters of the model from the spread of results in repeated fits to pseudo-data. To construct one realization of pseudo-data, we add to the predicted velocity from the best-fit model at every pixel a residual velocity from some other pixel chosen at random from residuals between the best fit model and the real data. Random interchange of residuals assumes that the residuals are uncorrelated, whereas inspection of our residual images generally reveals coherent patterns of residual velocities due to features, such as other forms of non-axisymmetric streaming and large-scale turbulence that are not included in our fitted model. Pseudo-data constructed by random interchange eliminates correlations between the residuals and generally leads to unrealistically small uncertainties. Thus we require a scheme that will reproduce appropriately correlated errors at random at each iteration of the bootstrap.

Spekkens & Sellwood (2007) adopted constant residuals over small patches of the image, which worked well for the small galaxy NGC 2976 where most of the correlations appeared to arise from turbulence. But that scheme cannot capture the patterns of residuals that arise from spirals and other non-axisymmetric distortions that are clear features in the residuals for larger galaxies. We therefore adopt a different approach here.

Since the dominant residual correlations appear over azimuthally extended regions in the disc plane, we manipulate the actual residual pattern as follows: we deproject it to face on and then, at every iteration, we rotate the residuals through a random angle. We also shift the residual pattern outwards by adding a constant to the radius of every pixel and subtract the maximum radius from those pixels that are shifted outside the map so that

they fill the hole created in the centre by the outward shift. The constant used to shift in radius is a randomly-chosen fraction of the radius of the map. We then reproject the new residual pattern, and assign a residual velocity at each pixel in the pseudo-data from that of the nearest pixel in the scrambled image. When we fit for an axisymmetric model in part of the galaxy and include a non-axisymmetric perturbation over a limited radial region, we scramble the residuals within each of these parts separately, and do not interchange residuals between the separate regions, since the appearance of residual patterns in the two regions can differ quite markedly.

Curriculum Vitae

Ricardo Zánmar Sánchez

Education

2001 – 2009	Ph.D., Physics, Rutgers University, New Brunswick, NJ
1996 – 2001	B.Sc., Technological Institute of Monterrey (ITESM), Monterrey, México

Publications

- "Modeling the Gas Flow in the Bar of NGC 1365", **Zánmar Sánchez, R.**, Sellwood, J. A., Weiner, B. J., Williams, T. B., 2008, *The Astrophysical Journal*, 674, 797
- "First Observations with the Southern African Large Telescope (SALT)", Romero-Colmenero, E., Buckley, D., Kniazev, A., Vaisanen, P., Loaring, N., Still, M., Hashimoto, Y., Potter, S., O'Donoghue, D., Nordsieck, K., Burgh, E., Williams, T., **Zánmar Sánchez, R.**, Rangwala, N., 2007, in "The Central Engine of Active Galactic Nuclei", *ASP Conference Series*, Vol. 373, 717
- "Commissioning of the Southern African Large Telescopes (SALT) first-generation instruments", Buckley, D. A. H., Barnes, S. I., Burgh, E. B., Crawford, S., Cottrell, P. L., Kniazev, A., Nordsieck, K. H., O'Donoghue, D., Rangwala, N., **Zánmar Sánchez, R.**, Sharples, R. M., Sheinis, A. I., Väisänen, P., Williams, T. B., 2008, *Proceedings of the SPIE*, Vol. 7014, 701407-701407-15